INVESTIGATION OF SELF-INDUCED THERMAL EFFECTS OF CO2 LASER RADIATION PROPAGATING IN ABSORBING GASES

David C. Smith, et al

United Aircraft Research Laboratories
East Hartford, Connecticut

1972

L921004-8

INVESTIGATION OF SELF-INDUCED THERMAL EFFECTS OF CO_2 LASER RADIATION PROPAGATING IN ABSORBING GASES

F. G. GEBHARDT

D. C. SMITH

ANNUAL REPORT

PERIOD COVERED: APRIL 30, 1971 TO APRIL 29, 1972

PREPARED UNDER CONTRACT DAAB07-70-C-0204

SPONSORED BY U.S. ARMY ELECTRONICS COMMAND

United Aircraft Research Laboratories

U
A

EAST HARTFORD, CONNECTICUT 06108

L921004-8

INVESTIGATION OF SELF-INDUCED THERMAL EFFECTS OF CO_2 LASER RADIATION PROPAGATING IN ABSORBING GASES

F. G. GEBHARDT

D. C. SMITH

ANNUAL REPORT
PERIOD COVERED: APRIL 30, 1971 TO APRIL 29, 1972

PREPARED UNDER CONTRACT DAAB07-70-C-0204

SPONSORED BY U.S. ARMY ELECTRONICS COMMAND

United Aircraft Research Laboratories

UNITED AIRCRAFT CORPORATION

EAST HARTFORD CONNECTICUT 06108

L921004-8

Investigation of Self-Induced Thermal Effects of CO_2 Laser Radiation Propagating in Absorbing Gases

Annual Report for the Period
30 April 1971 through 29 April 1972

Contractor: United Aircraft Research Laboratories

Effective Date of Contract: 30 April 1970

Contract Expiration Date: 29 April 1973

Contract Number: DAAB07-70-C-0204

Principal Investigator: David C. Smith (203) 565-5281

Project Scientist: Frederick G. Gebhardt (203) 565-7006

Contracting Agency: U. S. Army Electronics Command
Fort Monmouth, New Jersey

Contracting Officer: Rudolph G. Buser

Short Title: Thermal Distortion

Amount of Contract: $189,148

ABSTRACT

This report summarizes the work performed during the second year of an experimental and theoretical research program concerning the self-induced thermal distortion effects on cw CO_2 laser radiation propagating in absorbing media. The research program is directed toward improving the understanding of the possible limitations imposed by the atmosphere on the propagation of high power laser radiation. The work presented is concerned with essentially the following three different areas: (1) wind simulation experiments using a high pressure gas cell; (2) studies of the kinetic cooling of a gas by absorbing of CO_2 laser radiation; and (3) studies of turbulence effects on the self-induced thermal distortion of laser beams.

TABLE OF CONTENTS

SECTION I

INTRODUCTION

The United Aircraft Research Laboratories have been conducting an experimental and theoretical research investigation of the self-induced thermal distortion effects on cw CO_2 laser radiation propagating in absorbing media. For the past two years this research has been under the joint sponsorship of the U.S. Army Electronics Command and a parallel Corporate sponsored program. The research is directed toward improving the understanding of the possible limitations associated with the propagation of high power CO_2 laser radiation in the atmosphere. During the first year of this program considerable progress was made in obtaining an understanding of the self-induced thermal distortion effects on laser beam propagation in an absorbing medium in the presence of a uniform transverse wind.(Ref. 1) Experimental and theoretical results were obtained showing the thermal distortion to be determined by the nondimensional distortion parameter N and the Fresnel number, which are defined in terms of the pathlength, the source wavelength and beam size, and the properties of the propagation medium. Using liquid CS_2 as the absorbing medium experiments simulating a wide range of atmospheric conditions with wind were carried out for values of the distortion parameter N up to ~ 100, which represents the strong nonlinear interaction regime where extremely severe thermal distortion and intensity reduction effects occur. These results clearly show the seriousness of the convective thermal lens effects and through the use of the parameter N the results also provide a means for obtaining quantitative estimates for the atmospheric limitations that may be encountered in a variety of high power cw laser applications.

This report describes the work carried out during the second year of the program, which covers the period from 30 April 1971 through 29 April 1972. During this period the studies of thermally self-induced propagation phenomena have progressed in essentially the three different areas of (1) high pressure gas cell wind simulation experiments; (2) experimental and theoretical studies of the kinetic cooling of a gas by absorption of CO_2 laser radiation; and (3) experimental and theoretical studies of the effects of turbulence on the self-induced thermal distortion of laser radiation. Section II describes the high pressure gas cell experiments in which results obtained for the thermal lens effects of wind under large N conditions are examined as functions of the focal range and the total path attenuation. In addition to providing data for estimating the atmospheric limitations on high power propagation for a wide range of thermal distortion conditions, the experimental results in this section are also important for providing a means of checking the existing nonlinear propagation codes (Ref. 2-6), in the large distortion regime where errors and instabilities are likely to become important. The results of the focusing studies indicate that the optimum transmitter focus can be modified by the thermal distortion; and, in particular, it is found that it is possible for a higher target intensity to be achieved with a collimated beam than with a focused beam because of the thermal lens effects. This suggests the technique of varying

the transmitter focal range as a simple first step toward minimizing the thermal distortion effects. In Appendix C a related experiment is described in which the effects of astigmatism on the source beam phase distribution are examined as a possible means for reducing the thermal distortion by a wind.

The first experimental observation of the kinetic cooling of a gas has been achieved under the present contract using an electrically pulsed atmospheric pressure CO_2 laser. The details of this work have been published and are included here in Appendix D. In Section III a brief theoretical treatment of the kinetic cooling effect is given for both the cases of pulsed and cw laser radiation. From these considerations, expressions are derived for the magnitude and duration of the transient density variations. Expressions are also derived for the steady-state cooling effect that can arise with a cw beam in a transverse wind; and, results obtained using them in the nonlinear propagation code are included.

Section IV describes the theoretical and experimental efforts to determine the importance of atmospheric turbulence effects for the propagation of high power cw CO_2 laser radiation. A theoretical model is described in which the effects of velocity or mechanical turbulence are assumed to be dominant (in comparison with temperature turbulence) and are characterized by an eddy-diffusion coefficient. Laboratory experiments with artifically generated velocity turbulence in a 2 m long cell are also described. The results, which were obtained for the conditions of strong turbulent diffusion in comparison with the mean flow velocity, are in qualitative agreement with the theoretical model. The velocity turbulence provides a symmetric mode of heat transfer which tends to reduce the thermal distortion effects and replace the asymmetric bending and spreading by the mean wind velocity with a symmetric blooming. The importance of the turbulence effects, however, is proportional to the gustiness, i.e., the ratio of the rms-to-the mean wind velocity, which in the atmosphere is typically 10-30% or less. Thus, mechanical turbulence effects are expected to represent at most only a small perturbation on the thermal distortion of laser beams in the atmosphere.

Experimental results showing a comparison of the distortion with beam translation with that obtained in flowing gas in the 50 cm wind tunnel are included in Appendix A. These results indicate that the poor agreement with theory of some of the previous wind tunnel data (e.g., see Ref. 1, Fig. 27) may be due to the thick boundary layers associated with the low wind velocities rather than the effects of conduction or gas heating cited earlier. Thus, because of the possible interference of boundary layer and turbulence effects it is clear that beam translation experiments are preferred over the use of small wind tunnels for simulating atmospheric propagation in a laminar wind.

In Appendix B the correction factors to account for focused beam propagation and beam slewing in the thermal distortion parameter N are derived. The previously derived correction factor for the focused beam N(see Ref. 1, Eq. (17)), has been found to be accurate only in the limit of small amounts of focusing. In the limit of very large amounts of focusing (i.e., when the ratio of the initial beam size to the undistorted beam size at the target is large) the correct value of N is increased by approximately a factor of two from the value obtained using only the initial-to-target beam size ratio (Ref. 1, Eq. (17)) to account for the focusing.

SECTION II

Large N Wind Simulation Experiments

2.1 Introduction

In this section, experiments using a high pressure gas cell are described. Results are obtained for the thermal lens effects of a laminar wind under conditions where the distortion parameter N becomes large. In these experiments the thermal distortion is examined as a function of the focal range of the source and the total path attenuation. The advantage of using a high pressure gas for obtaining a large distortion effect with a wind has been discussed previously (Ref. 1); and, is based on the reduction of effects due to thermal conduction that can irterferewith the experiments at the low wind velocities which are used. In addition, difficulties with previous gas experiments using recirculating wind tunnels have recently been shown to be caused by the boundary layer effects as is discussed in Appendix A. The main objectives of the large N thermal distortion experiments with the high pressure gas cell were to examine the influence of varying αt and also to study more carefully the effects of focusing. Although large N thermal distortion results have been obtained using liquid CS_2 , it has not been possible to obtain results for values of αt less than ~ 2 due to the large attenuation of CS_2 at 10.6 μ.

2.2 High Pressure Gas Cell Thermal Distortion Experiments

The experimental arrangement used to carry out the thermal distortion experiments is shown in Fig. 1. The experiments consisted essentially of propagating a CO_2 laser beam through a moving cell of gas oriented vertically (to minimize natural convection effects) which simulates the effects of a transverse wind, and then monitoring the resulting thermally distorted intensity patterns as a function of the laser beam power. The laser used in the experiments produced approximately 20 watts in the TEM_{oo} mode amd was stabilized to reduce amplitude fluctuation in the output power. In the first series of experiments to be described, the distortion effects obtained with collimated and focused beams are compared. For the focused beam case, a curved mirror (M_1) of radius 2.15 m was used. The collimated beam was obtained with a mirror curvature for (M_1) of 6.78 m radius. The high-pressure gas cell consisted of a 5 cm diameter by 103 cm long tube with 5mm thick AR coated Ge windows at both ends. For all the experiments, except those examing the αt dependence in Section 2.4, pure CO_2 at a pressure of 150 psig was used in the cell. The CO_2 absorption coefficient was found to increase from $\sim 1.8 \times 10^{-3} cm^{-1}$ at 1 atm pressure to $\sim 4.10 \times 10^{-3} cm^{-1}$ at 150 psig or $\sim$ 11 atm pressure. The increase in the absorption coefficient is due to the effect of rotational line overlap (Ref.7) and the measured increase by a factor of ~ 2.3 for 11 atm is in reasonable agreement with the value of 2.6 that has been reported by Christiansen,et.al., (Ref. 7). The transmission of the cell windows was measured to be $\sim$ 84 percent with N_2 at ~5 psig in the cell. The absorption coefficient of the CO_2 was observed to increase

somewhat with the laser beam power due to its temperature dependence and the influence of gas heating. For example, with the cell stationary the CO_2 transmission was reduced by ~ 7 percent with a laser beam power of 15 W. With the amount of cell motion involved in all of the experiments and for the power levels used, however, the variation of the CO_2 transmission with power could not be observed within the accuracy of the power measurements and thus, is considered to be negligible.

The types of data obtained in the experiments include photographs of the distorted laser beam patterns obtained using Kalvar film and intensity profiles measured by moving a detector equipped with a 35 micron diameter pin-hole across the beam along with the moving gas cell. The pertinent parameters for the various experiments including the undistorted laser beam radii at the cell input and output planes together with the cell velocity, absorption coefficient, path length, etc., are shown in Table I with the experiments identified by the appropriate dates and focusing conditions.

In Figs. 2, 3, and 4 are shown the data obtained with the collimated beam. Fig. 2 contains the undistorted intensity patterns and profiles along the wind direction, i.e., the direction of cell motion. This data is shown to indicate the deviation from the ideal symmetric gaussian beam shape which is assumed in the theory. The distorted intensity patterns for the collimated beam are shown in Fig. 3 for various values of the distortion parameter N, where

$$N = \left[\frac{(-dn/dT)\ 2\ P\ z}{\pi\ n\ \rho\ c_p v\ a_i^3}\right]\left\{1 - \frac{(1-e^{-\alpha z})}{\alpha z}\right\}\left(\frac{a_i}{a_o}\right) q \qquad (1)$$

Here, n, dn/dT, ρ, c_p, v and α are, respectively, the refractive index, index change with respect to temperature, density, specific heat at constant pressure, velocity and absorption coefficient of the medium; z is the absorbing path length, a_i and a_o are, respectively, the undistorted laser beam radii at the input (source) and output (target) planes, and P is the power. The distortion parameter N is used as measure for the strength of the thermal lens effects with wind and was derived originally for a collimated gaussian beam. As shown in Appendix B the effect of focusing is accounted for in N by the ratio a_i/a_o and the numerical correction factor q (see Fig. B-1), which varies from 1 to 2 as a_i/a_o varies from 1 (collimated beam case) to ∞. Although this form of the focusing correction to N applies strictly only for $\alpha z << 1$, it is also used for finite αz in Eq. (1) in the interests of keeping the expression as simple as possible. The values for the distortion parameter N in the present experiments are calculated using the measured quantities P, a_i, a_o, v, αt, and z indicated in Table I. together with the known properties of CO_2 which for convenience are tabulated in Table II. Here t is the cell length and to account for the small air path (for which $\alpha \sim 0$) between the end of the cell and the detector plane we distinguish between the total path z and t and use αt instead of αz in the term inside the curly brackets in Eq.(1). The collimated beam crescent patterns for N=1.35, 2.7 and 5.4 in Fig. 3 compare favorably with computer results obtained by Wallace (see Ref. 5, Fig. 4) for the cases $z = z_o$, $1.5\ z_o$ and $2\ z_o$, which correspond to N ~ 1, 2.25 and 4, since $N \sim (z/z_o)^2$ (Ref. 1, p. 6).

Quantitative data is obtained for the thermal distortion in terms of the magnitude and deflection of the peak intensity as found from the measured intensity profiles shown in Fig. 4. The intensity profiles in Fig. 4 are grouped together for the two different velocities of v = 1 and 0.5 cm/s to show that the inverse velocity dependence of N in Eq. (1) correctly accounts for the observed thermal distortion.

In Figs. 5-8, data obtained for the focused beam case are shown. The undistorted beam patterns and profiles given in Fig. 5 indicate that the beam deviates somewhat from an ideal gaussian. Comparison of the distorted intensity patterns shown in Fig. 6 for the focused beam with the collimated beam data in Fig. 3 shows a distinct difference in the nature of the distortion resulting from the convective thermal lens effect. In particular, the small islands which form in the distorted patterns for the focused beam at the larger values of N are absent in the distorted collimated beam patterns which retain their crescent shape and do not exhibit the tendency to break up. This aspect of the distortion has also been found in numerical calculations of focused beam propagation as is shown in Appendix E. In Figs. 7 and 8, the proper scaling of the thermal distortion for the two different velocities of v = 1 and 0.5 cm/s is again clearly shown by the measured intensity profiles.

In Fig. 9 a series of distorted patterns and intensity profiles are shown which indicate progressively the influence of natural convection effects as the laser beam power increases from P = 7.2 W to 14.4 W for the wind velocity of 0.5 cm/s. The effects of natural convection are indicated by the filling in of the crescent pattern. An estimate of the natural convection velocity for a stationary cell oriented vertically can be obtained from the expression (Ref. 8)

$$v_{nc} \sim \left[\frac{g \alpha t P}{24\pi c_p \mu T_o}\right]^{\frac{1}{2}} , \qquad (2)$$

where g is the acceleration of gravity, t is the cell length, μ is the viscosity coefficient and T_o is the ambient temperature. For the conditions appropraite to Fig. 9, we obtain $v_{nc} \sim 1.2 \times 10 P^{\frac{1}{2}}$, where P is in watts. Defining the characteristic natural convection time $\tau_{nc}=t/v_{nc}$ and the time $\tau_w = 2 a_i/v$ associated with the cell volocity simulating a transverse wind, one expects the ratio τ_{nc}/τ_w to be near unity when natural convection effects are important. Indeed, for the power levels of ~7 - 14 W in Fig. 9, v = 0.5 cm/s and a_i = 0.25 cm, the ratio τ_{nc}/τ_w varies from ~3 to 2. Evidently, the onset of natural convection is associated with a critical value for τ_{nc}/τ_w of about 2.5 since natural convection effects appear to be unimportant in the P = 7.2 W case while they become dominant for P = 14.4 W in Fig. 9.

In Figs. 10 and 11, respectively, the normalized peak intensity and beam deflection dependence on N are shown for both the focused and collimated beam

cases. The normalized peak intensity I_{REL} is the ratio of the distorted peak intensity to that intensity which would be obtained in the absence of thermal distortion. The data shown in Fig. 10 for the focused beam differ considerably from that for the collimated beam for the values of N larger than three. For the focused beam, I_{REL} decreases with N at a rate which is greater than 1/N, for values of N greater than $N \sim 3$. The rapid decrease of I_{REL} with N does not occur for the collimated beam until N becomes greater than 10. The difference between the collimated and focused beam deflection dependence on N is less pronounced as shown in Fig. 11. However, similar to the normalized peak intensity, the beam deflection for a collimated beam does not increase as rapidly with N as it does in the focused beam case.

A different way of presenting data for the effect of the thermal distortion on the laser beam intensity is shown in Fig. 12. Here, the dependence of the peak intensity on the laser beam power is given. At very small power levels, the peak intensity increases nearly linearly with power as expected for propagation in a linear medium. However, since the nonlinear thermal lens strength measured in terms of N also increases with power, a maximum in peak intensity is eventually reached. Any further increase in the laser beam power tends to reduce the peak intensity because of the severe spreading effects produced by the convective thermal lens. It is interesting to note from Fig. 12 that the maximum target intensity is achieved with the collimated beam rather than the focused beam, but at a considerably higher value of laser beam power. Also, it should be noted that doubling the velocity from 0.5 to 1 cm/s simply doubles the power level at which the maximum peak intensity occurs. This is reasonable since the maximum of the peak intensity versus power curve should always occur at the same value of $N = N_p$ for a given laser beam.

2.3 Liquid CS_2 Cell Thermal Distortion Experiment

For convenience in comparing the high-pressure gas experiments with the liquid CS_2 experiments and also because the latter data (Ref. 1) has been replotted to properly account for the effects of focusing in N as shown in Appendix B, the CS_2 data for the peak intensity and beam deflection dependence on N and the peak intensity versus power are shown in Figs. 13, 14, and 15, respectively. Comparison of these results with Figs. 10 - 12 shows that the thermal distortion results follow essentially the same trends in both the liquid and high-pressure gas cases. It is also found from Fig. 15 that a higher peak intensity can be achieved at a target with a collimated beam than for a focused beam as in the high-pressure gas experiments. As in Fig. 12, the label N_p indicates the value of N for which the peak target intensity reaches a maximum with increasing power. Later, it will be shown that N_p corresponds to the points on the I_{REL} curves in Figs. 10 and 13 where the slope equals minus one.

2.4 Dependence of Thermal Distortion on αt

With the high-pressure gas cell, it is possible to vary the total attenuation or, equivalently αt, by varying the concentration of the absorbing gas in the cell. To examine the dependence of the thermal distortion on αt a series of focused beam experiments with three different absorbing conditions were performed. The focused beam was obtained using the Ge lens telescope as shown in Fig. 1. The objective in these experiments was to determine if an additional dependence on αt existed beyond that implicit in the expression for the distortion parameter N given in Eq. (1). The results of the experiments are shown in Figs. 16-18. The different amounts of total cell attenuation were obtained by using a mixture of CO_2 and nitrogen to give $\alpha t = 0.13$; pure CO_2 for which $\alpha t = 0.44$; and a mixture of nitrogen plus a small amount of propylene (C_3H_6) was used to provide $\alpha t = 2.3$. In all cases, the total pressure in the cell was 150 psig. From Figs. 17 and 18 showing the dependence of the normalized peak intensity and beam deflection on N, it is clear that there is a dependence on αt which becomes more pronounced with increasing values of N. Generally speaking, for the smallest value of αt, the thermal distortion effects are more pronounced than for the larger value of αt at the same value of N. This is borne-out in Fig. 16 where the distorted intensity profiles for comparable values of N can be compared for the three values of αt. Here it is seen that for $\alpha t = 0.13$ the thermal distortion is more severe than it is for $\alpha t = 0.44$ and 2.3 at the same value of N. It is interesting to note the axial peaks in the intensity profiles for N = 12 and 16 with $\alpha t = 0.13$, which are larger than the peaks associated with the deflected portion of the beam. Although there appears to be a tendency for axial peaks to be formed in the intensity profiles for the larger values of αt they are not as well developed. A possible explanation for the αt dependence evident in Figs. 16-18 is that the values of N given by Eq. (1) do not properly account for the effects of focusing when αz is large (see Appendix B). This makes sense physically since it is clear that focusing will have little effect on the thermal distortion in the limit of large αz because the intensity is reduced by attenuation at the focal range where one expects the focusing to have the greatest effect on the distortion.

2.5 Focusing Effects on Thermal Distortion

To examine the effects of focusing on the thermal distortion by a wind the Ge lens telescope was adjusted to focus the beam at approximately 0.75 z, z, 1.25 z and at some range between 1.25 z and ∞, the latter being the collimated beam case, where z is the range to the target, or detector plane. The differences between the thermal distortion obtained with these focusing conditions are shown qualitatively in Fig. 19. The intensity profiles measured as a function of laser beam power for the various focusing conditions are shown in Figs. 20 and 21. Values of N were not computed for the focusing experiments since the concept of N is of questionable value for beams which do not follow the usual collimated or focused behavior. For this case, a much better comparison is obtained in terms of the peak intensity dependence on the laser beam power shown in Fig. 22. Based on the data shown in Fig. 22, the maximum target intensity is achieved with

the beam focused at the target or when F/z = 1. With the beam focused in front of the detector (F/z = 0.74) or with the beam focused beyond the detector (F/z = 1.26) the maximum intensities are less than for the focused case. If the beam is defocused even further, i.e., F/z > 1.26, the maximum peak intensity appears to be slightly higher; and presumably for the collimated beam case, the maximum peak intensity will be greater than for the focused beam case as found earlier in Figs. 12 and 15. From Fig. 22, it is clear that the thermal distortion by a wind changes the optimum focal range for the laser transmitter. For example, under conditions in Fig. 22 where the laser beam power is 4 watts, a greater target intensity can be achieved by focusing 25% beyond the target than by focusing at the target range. This suggests that a variable transmitter focus can be used as a simple means of reducing the thermal distortion effects since under extremely large distortion conditions (i.e., large power levels) Fig. 22 indicates an improvement in target intensity can be achieved by defocusing the beam. This concept is related to experiments discussed in Appendix C, in which the effects of astigmatism are examined as a possible means for reducing the thermal distortion effects of wind.

2.6 Summary of Wind Simulation Experiments

The simulation of the thermal distortion effects of a laminar wind with the liquid CS_2 and high pressure gas cell experiments provides results which can be used to check nonlinear propagation codes and to develope models for predicting the limitations imposed by thermal blooming on various high power applications. The key to the use of the laboratory simulation results lies in the use of the dimensionless parameters N, $k a_i^2 /z$ and αz, which refer, respectively, to the thermal distortion (i.e., the strength of the nonlinear interaction); the Fresnel number based on the range z and the source beam radius a_i, and wave number $k = 2\pi/\lambda$ where λ is the wavelength; and the fractional attenuation factor αz. By evaluating these parameters for the situation of interest one can then refer to the normalized peak intensity and beam deflection results in Figs. 10,11,13,14 or 17,18 depending on which are most appropriate in terms of the degree of focusing and the total path attenuation.

The situation can best be summarized as follows. The distortion parameter N must be evaluated using Eq. (1) with the appropriate values for the properties of the medium and the beam radius a_i of the source, which, strictly speaking, is assumed to be gaussian, and the beam radius a_o at the target range z. The degree of focusing is, of course, given by a_i/a_o which for a diffraction limited beam focused at the range z is given to good approximation by the Fresnel number $k a_i^2 /z$. The experimental results for focused beams indicate that I_{REL}, which is the peak intensity normalized by the undistorted value at the range z, drops off

to 0.5 for values of N in the range of 3 to 6 and to 0.1 for N in the range of 9 to 18, depending on the magnitude of αz. I_{REL} decreases more rapidly with N when $\alpha z \ll 1$ than when $\alpha z \gtrsim 1$ as shown in Fig. 17. When $I_{REL} \lesssim 0.1$, the thermally self-induced spreading, bending and distortion effects are probably too severe to be tolerated for most applications and thus N should probably be less than $\sim 10 - 20$ for cases of practical interest. It is perhaps worthwhile mentioning that although the degree of focusing has been limited in the experiments to only a relatively small range the results may still provide a reasonable estimate for more strongly focused beams in view of the uncertainties associated with the effects due to turbulence and deviations in the source beam profile from the ideal symmetric gaussian.

For the case of a collimated or diverging beam the size of the Fresnel number is important since it determines if diffraction effects are strong enough to offset the self-focusing tendency of the convective thermal lens in the plane parallel with the wind. For most situations of practical interest the Fresnel number is expected to be $\lesssim 10$, however, and thus the self-induced intensification effect will not be important (Ref. 9). The experimental results do indicate, however, that I_{REL} decreases much less rapidly with N for a collimated beam than for a focused beam, which, no doubt, is related to the greater spreading and the formation of the central lobe in the distortion of the focused beam. It is important to note (see Figs. 12, 15 and 22) that for conditions where N is sufficiently large, it is possible for the target intensity to be greater with the beam collimated (or perhaps only defocused to a somewhat greater range) than when it is focused at the target. This can occur since not only is the collimated beam N smaller by the factor $a_o/q\, a_i$ than the value for the focused beam but also I_{REL} decreases less rapidly with N for the collimated beam as pointed out above.

The plots of I_{REL} versus N (see Figs. 10, 13 and 17) have an interesting and useful interpretation if one considers the situation where only the laser power is variable and the range, wind velocity, absorption coefficient and source beam size and focus remains fixed. In this case, the ordinate on the I_{REL} versus N plots may be associated with the power since N is proportional to the laser power and the remaining conditions are assumed constant. The peak intensity at the target range z is given by $I_p(z) = I_u(z)\, I_{REL}(N)$ where $I_u(z)$ is the undistorted peak intensity which is also proportional to the laser power. Clearly, the target peak intensity I_p will increase with power so long as I_{REL} does not decrease with N (or, equivalently P) as 1/N or faster. From the I_{REL} versus N data shown in

Figs. 10, 13 and 17 one can then see that I_p increases with the laser beam power until the slope of the curve equals -1, or equivalently, $I_{REL} \propto 1/P$. Beyond this point where I_{REL} decreases more rapidly than $1/N$ the value of I_p actually decreases with increasing power because of the influence of the nonlinear thermal distortion effects. Thus, the value of N for which the log I_{REL} versus log N plot has a slope of -1 corresponds to the point where the peak target intensity reaches a maximum with power and is labeled N_p in Figs. 12 and 15. The value of N_p can be used to determine the maximum power that can be used effectively for a given source beam configuration and set of propagation conditions. This power and the associated value of I_{REL} then determine the maximum peak target intensity obtainable under these conditions.

In Appendix E numerical results obtained by Bradley and Herrmann (Ref. 2) for the thermal distortion of a focused beam are compared with a distorted laser beam pattern measured in a liquid CS_2 experiment. The distortion parameter N is used to make the comparison between the simulation experiment and the computer calculation which is for high power propagation conditions in the atmosphere. The good agreement of the results establishes the validity of the laboratory simulation experiments and also provides evidence for the usefulness of N for scaling the thermal lens effects of wind to account for a wide range of conditions.

SECTION III

KINETIC COOLING

3.1 Introduction

The kinetic cooling of air by the absorption of CO_2 laser radiation was first discussed by Gerry (Ref. 10) and has since been studied by Glass (Ref. 10) and Wood, Camac and Gerry (Ref. 11). The cooling effect, which is transient in nature, causes an increase in the gas density that tends to focus the laser beam and thus the effect is generally regarded as being beneficial to high power propagation. The kinetic cooling effect can be important for both pulsed and cw propagation. In the cw case, however, a transverse wind or beam motion is required for the kinetic cooling to produce a steady-state focusing effect. The first experimental evidence for the kinetic cooling effect (Ref. 12) was obtained under the present Army Contract and the details of the work are presented in Appendix D. The kineti cooling effects were observed on a transient basis in mixtures of CO_2 and N_2 using an electrically pulsed atmospheric pressure CO_2 laser. Due to the effects of saturation and the limited sensitivity of the interferometer the cooling effects could only be observed with CO_2 concentrations greater than 5 percent. As a result, the characteristic cooling times observed were limited to several hundred microseconds as compared with times on the order of 2-50 milliseconds predicted for normal air with approximately 0.03 percent CO_2 (Ref. 11). Future experiments are planned to observe the kinetic cooling effect in normal atmospheric air using either a higher energy pulsed or a high power cw CO_2 laser.

In this section the theory for the kinetic cooling effect in air is briefly summarized and expressions for the transient gas temperature changes resulting from the cooling are derived for the cases of a short pulse and a cw CO_2 laser source in stationary air. These expressions are needed to determine the optical effects and the requirements for laboratory experiments investigating the kinetic cooling process. The steady-state temperature expression for the cooling effect with a cw beam in a wind or with beam motion is also derived and the result is used to modify the nonlinear propagation code to account for kinetic cooling. Numerical results illustrating the kinetic cooling effect with wind are shown in Section 3. .

3.2 Summary of Theory

The kinetic cooling effect is a result of the vibrational energy exchange processes that are involved in the absorption of 10.6 μ wavelength radiation by the CO_2 in air. A detailed theoretical treatment of the absorption process has led to a simple approximate model for the kinetic cooling in air (Ref. 11). According to this model, the laser beam energy absorbed by CO_2 is stored in the combined vibrational levels CO_2 (001) and N_2 (v=1), for which the effective collisional relaxation time is τ. The relaxation time for the lower level (CO_2 (100)) of the

absorbing transition is essentially instantaneous in comparison with τ.* Thus, equilibrium of the CO_2 (100) level, which is depleted by absorption, is rapidly restored by collisional energy transfer from translation. In this way, the gas is cooled until the stored vibrational energy heats the gas after the effective relaxation time τ.

An expression for the gas temperature at constant pressure is found from the equation for energy conservation neglecting heat conduction (Ref. 13)

$$\rho\left(\frac{\partial h}{\partial t} + \vec{v} \cdot \nabla h\right) = \alpha_t \; I(t) \quad , \tag{3}$$

where the enthalpy $h = c_p T + E_v$, I is the laser beam intensity and ρ, c_p , T, α_t and v are respectively, the density, specific heat at constant pressure, temperature, total absorption coefficient and velocity of the gas. E_v is the change in the vibrational energy of the combined CO_2 (001) and N_2 (v=1) levels which results from the absorption of 10.6 μ radiation by the CO_2 , and is governed by the equation

$$\rho\left(\frac{\partial E_v}{\partial t} + \vec{v} \cdot \nabla E_v\right) = 2.44 \; \alpha_c \; I(t) - \rho \frac{E_v}{\tau} \quad , \tag{4}$$

where α_c is the CO_2 contribution to the total absorption coefficient $\alpha_t = \alpha_c + \alpha_h$, and α_h accounts for the absorption due to water vapor. The energy absorbed by water vapor does not appear in Eq. (4), since it is rapidly transferred to translation and thus leads only to gas heating (Ref. 11). The factor 2.44 in Eq. (4) is the ratio of the vibrational energy of the CO_2 (001) level to the 10.6 μ photon energy $h\nu$, which accounts for the fact that each absorbed 10.6 μ photon with energy $E_{001} - E_{100}$ results in a vibrational quantum of energy E_{001} that is stored in the N_2 . Using the definition for h and Eq. (4) in Eq. (3) gives

$$\frac{\partial T}{\partial t} + \vec{v} \cdot \nabla T = \frac{\alpha_t \; I(t)}{\rho \; c_p} \left(1 - 2.44 \frac{\alpha_c}{\alpha_t}\right) + \frac{1}{c_p} \frac{E_v}{\tau} \quad , \tag{5}$$

which must be solved together with

$$\frac{\partial E_v}{\partial t} + \vec{v} \cdot \nabla E_v = \frac{2.44 \; \alpha_c}{\rho} \; I(t) - \frac{E_v}{\tau} \tag{6}$$

---

* Although this is true in air where the CO_2 concentration is typically ~0.033 percent the effect of the lower level relaxation time cannot be neglected when the CO_2 concentration is $\gtrsim$ 10 percent as in the experiments in Appendix D.

to obtain the temperature.

The transient temperature changes for pulsed and cw laser radiation are now considered with the gas stationary (i.e., $\vec{v} = 0$ in Eqs. (5) and (6)). For the pulsed case the pulse width τ_p is assumed to be much shorter than the relaxation time τ. Thus, for $I(t) = I_o \tau_p \delta(t)$, where $\delta(t)$ is the unit impulse function and $I_o \tau_p$ is the energy density of the pulse, the change in gas temperature following the laser pulse is given by

$$\Delta T\ (t) = \frac{\alpha_t I_o \tau_p}{\rho\ c_p} \left[1 - 2.44 \frac{\alpha_c}{\alpha_t}\ e^{-t/\tau} \right]. \tag{7}$$

If $\alpha_c/\alpha_t > 0.41$ transient cooling of the gas will occur. The cooling effect is greatest, of course, if $\alpha_t = \alpha_c$ (i.e., $\alpha_h = 0$) in which case the maximum temperature decrease, which occurs at $t = 0$, is

$$\left|\Delta T_m\right| = 1.44\ \frac{\alpha_c I_o \tau_p}{\rho\ c_p}\ . \quad \text{(Pulsed)} \tag{8}$$

The time interval for which the gas is cooled is $0.89\ \tau$ or less depending on whether α_h/α_c is equal to or greater than zero. It should be pointed out that the presence of water vapor (i.e., $\alpha_h \neq 0$) will not only reduce the magnitude of the cooling effect but also decrease the relaxation time τ.

For the case of a cw laser beam, we assume for the intensity $I(t) = I_o\ u(t)$, where $u(t)$ is the unit step function, and from Eqs. (5) and (6) the temperature change is

$$\Delta T(t) = \frac{\alpha_t I_o}{\rho\ c_p} \left[t - 2.44\ \frac{\alpha_c}{\alpha_t}\ \tau\ \left(1 - e^{-t/\tau} \right) \right]\ . \tag{9}$$

Assuming $\alpha_t = \alpha_c$, the maximum temperature decrease occurs at $t = 0.89\ \tau$, and its magnitude is given by

$$\left| \Delta T_m \right| = 0.55\ \frac{\alpha_c I_o \tau}{\rho\ c_p}\ . \quad \text{(cw)} \tag{10}$$

Equations (8) and (10) can be used to determine the requirements for experimentally observing the kinetic cooling effect in dry air. In normal atmospheric air the relaxation time τ is reduced by the presence of O_2 and H_2O (Ref. 11) and this together with the absorption due to the water vapor will decrease the magnitude of the cooling effect as indicated by Eqs. (7) and (9).

For the case of a cw beam with the uniform wind velocity v in the x-direction a steady-state solution for the gas temperature can be found from Eqs. (5) and (6). Taking the Laplace transform of Eq. (6) and using the boundary condition $E_v(\vec{r}\,;t = 0) = 0$ leads to the result

$$E_v(\vec{r};t) = \frac{2.44\,\alpha_c}{v\rho}\int_{x-vt}^{x} I(x',y,z)\; e^{-(x-x')/v\tau}\, dx' \quad . \quad (11)$$

Substituting this expression into Eq. (5) and setting $\partial T/\partial t = 0$ while letting $t \to \infty$ gives the equation to be solved for the steady-state temperature

$$\frac{\partial T}{\partial x} = \frac{\alpha_t I}{\rho\, c_p v}\left(1 - 2.44\,\frac{\alpha_c}{\alpha_t}\right) + \frac{2.44\,\alpha_c}{\rho\, c_p v^2 \tau}\int_{-\infty}^{x} I(x',y,z)\; e^{-(x-x')/v\tau}\, dx' \quad . \quad (12)$$

Integration of Eq. (12) from $-\infty$ to x gives for the steady-state temperature

$$T(x) - T(-\infty) = \frac{\alpha_t}{\rho c_p v}\int_{-\infty}^{x} I(x;y,z)\left(1 - \delta\, e^{-(x-x')/v\tau}\right) dx' \,, \quad (13)$$

where

$$\delta = 2.44\,\frac{\alpha_c}{\alpha_t} \quad . \quad (14)$$

In the following section this expression is used to modify the nonlinear propagation code to account for the kinetic cooling effect for a cw beam in a wind.

3.3 Numerical Results

The computer code used to describe the nonlinear propagation effects for a cw beam in a transverse wind is described in Ref. 1, Section 3.6. To account for kinetic cooling in the numerical procedure the appropriate changes must be made in the expressions for $\vec{\theta}_{n\ell}(z)$ and $\Psi(z)$ which appear in Eqs. (36) and (39), respectively, of Ref. 1. Since in general

$$\vec{\theta}_{n\ell}(z) = z \frac{\nabla_t n}{n_o} = \frac{z}{n_o} \frac{dn}{dT} \nabla_t T \quad , \tag{15}$$

where ∇_t is the transverse gradient operator, the effects of kinetic cooling can be included by using the steady-state temperature expression in Eq. (13) to evaluate Eq. (15) with the result

$$\vec{\theta}_{n\ell}(z) = \epsilon z \left\{ \hat{x} \left[(1-\delta) I + \frac{\delta}{v_T} \int_{-\infty}^{x} I e^{-(x-x')/v_T} dx' \right] + \hat{y} \int_{-\infty}^{x} \frac{\partial I}{\partial y} (1-\delta e^{-(x-x')/v_T}) dx' \right\} \quad , \tag{16}$$

where

$$\epsilon = \frac{(dn/dT)\,\alpha_t}{n_o \rho\, c_p v} \tag{17}$$

Here, ϵ is the same as in Ref. 1, except that $\alpha_t = \alpha_c + \alpha_h$ has replaced α. Also, if δ is set equal to zero, or equivalently $\alpha_c = 0$ and no cooling can occur, Eq. (16) reduces to same expression as in Ref. 1, Eq. (36), as required.

The expression for $\Psi(z)$ from Ref. 1, Eq. (39) is

$$\Psi(z) = -z \left(\nabla_t + \frac{\nabla_t I}{I}\right) \cdot \vec{\theta}_{n\ell}(z/2) \quad , \tag{18}$$

which after substitution of Eq. (16) and performing the indicated operations becomes

$$\Psi(z) = -\frac{\epsilon z^2}{2}\left\{ 2(1-\delta)\frac{\partial I}{\partial x} + \frac{\delta}{v_T} I \right.$$

$$-\frac{\delta}{(v_T)^2}\left(1-\frac{v_T}{I}\frac{\partial I}{\partial x}\right)\int_{-\infty}^{x} I\, e^{-(x-x')/v_T}\, dx'$$

$$+\int_{-\infty}^{x}\frac{\partial^2 I}{\partial y^2}\left(1-\delta\, e^{-(x-x')/v_T}\right) dx' \qquad (19)$$

$$\left.+\frac{1}{I}\frac{\partial I}{\partial y}\int_{-\infty}^{x}\frac{\partial I}{\partial y}\left(1-\delta\, e^{-(x-x')/v_T}\right) dx'\right\}$$

Again, if δ is set equal to zero in Eq. (19) the expression reduces to the proper result for pure beam heating. Equations (16) and (19) have been used in the numerical procedure to examine the convective thermal distortion associated with kinetic cooling.

The two parameters $\delta = 2.44\,\alpha_c/\alpha_t$ and $\beta = v_T/a_o$ are used in connection with the kinetic cooling to characterize the nonlinear propagation effects in conjunction with the distortion parameter N and Fresnel number $F = ka_o^2/z$. The parameter δ, which can vary from zero (pure heating) to 2.44 indicates the relative importance of the transient cooling by the CO_2 absorption as compared with the gas heating due to the absorption by water vapor. The parameter β is the ratio of the relaxation time τ to the gas transit time a_o/v, where a_o is the 1/e intensity radius of the gaussian beam source. The cooling effect will be most important when τ is comparable to or greater than a_o/v (i.e., for $\beta \gtrsim 1$), which means that the vibrational energy due to CO_2 absorption that is stored in N_2 is removed from the vicinity of the beam before heating the gas after the relaxation time τ. The distortion parameter N is evaluated in the same way when kinetic cooling is included as for the case of pure heating, with the total absorption coefficient used in each case. With kinetic cooling the parameters δ and β must be specified in addition to the parameters N and F which indicate, respectively, the strength of the nonlinear interaction and the importance of diffraction effects.

An example of the thermal lens effect of kinetic cooling with a wind is shown in Fig. 23 for a collimated gaussian beam with $\delta = 2.44$ (i.e., for $\alpha_h = 0$) and $\beta = 2.0$. The constant intensity contours representing 40 percent of the peak are shown for N = 0.52 and F = 6.67 for both the cooling and pure heating (i.e., $\delta = 0$) cases. Comparison with the 40 percent contour for the undistorted beam (i.e., for N = 0) shows that a strong self-focusing effect is associated with the cooling. For this case the peak intensity is increased to approximately three times the undistorted peak intensity and the beam dimension is decreased roughly by a factor of two. It should also be noted that the distorted peak intensity shifts in the wind direction under the influence of cooling rather than into the wind, as is the case when beam heating occurs.

In Fig. 24, the relative peak intensities, I_{REL}, are plotted as functions of N for both the cooling and heating cases.* The self-focusing due to the kinetic cooling, which for the case plotted is for the conditions $\delta = 2.44$ and $\beta = 2$, leads to a more rapid change in the distorted peak intensity with N than in the heating case, where both focusing and blooming effects are involved. The dashed curves in Fig. 24 show the dependence on N of the normalized average intensity

$$I_{AVE} = \frac{2\pi a^2}{A_{eff}} = 2\pi a^2 \frac{\int I^2 \, dA}{\left(\int I \, dA\right)^2} \quad , \tag{20}$$

where A_{eff} is the effective beam area and $\int I \, dA$ is the total power. It is interesting to note that although I_{AVE} follows I_{REL} fairly closely for the pure heating case, there is a greater discrepancy between the two with kinetic cooling. The reason for this can be traced to the beam distortion associated with cooling which causes the central portion of the beam to contract more than the outer portions. For example, with the N = 0.52 case in Fig. 23, the diameter of the 10 percent contour (not shown) is reduced by less than a factor of 1.5 as compared with the factor of two decrease in the diameter of the 40 percent contour.

The normalized beam deflections are plotted versus N in Fig. 25 for both the cooling and heating cases. For small values of N, the deflection with cooling is $\sim 3N/2$, which is equal in magnitude to the heating case but in the opposite direction. As N becomes larger, the deflection with cooling increases less rapidly than for the pure heating case.

The data in Figs 24 and 25 represent essentially the extremes in the behavior of the magnitude and position of the distorted peak intensity with pure heating and strong cooling conditions. For smaller values of δ and β the deflection and I_{REL} curves will lie somewhere between the two extremes. In particular, for the case $\delta = 1.0$, where the absorption due to CO_2 is ~ 41 percent of the total, and with $\beta = 2.0$, the kinetic cooling effectively balances the heating and there is essentially no change in peak intensity or deflection as the parameter N increases.

---

* The quantities F_o and z_o shown in Figs. 24 and 25 refer, respectively, to the Fresnel number and range for which N = 1.

SECTION IV

TURBULENCE EFFECTS ON THERMAL BLOOMING

4.1 Introduction

Previous studies of the self-induced thermal distortion of high power cw CO_2 laser beams have ignored the possible influence of atmospheric turbulence. To establish a realistic model for assessing nonlinear propagation effects in the atmosphere it is necessary to be able to estimate how and to what extent the turbulence will modify the thermal lens effects from those predicted on the basis of a laminar wind. The temperature fluctuations associated with atmospheric turbulence are responsible for producing the so-called linear scattering effects which can influence both low and high power propagation. The turbulent velocity fluctuations, on the other hand, have no direct effect on low power propagation but they may be important at high power levels because of their interaction with the beam heating and self-distortion effects due to the absorption by CO_2 and water vapor. The temperature turbulence effects on propagation have been studied extensively and are reasonably well understood. Thus, since we are mainly interested in the effect of the turbulence on the thermal lens, we assume as a first approximation that temperature turbulence effects on the thermal distortion may be accounted for by an appropriate spreading angle for the mean intensity profile. The effects of the velocity fluctuations or mechanical turbulence on the thermal distortion thus remain and are the main subject of concern in this section.

The principal results of this section are a theoretical model accounting for mechanical turbulence effects and laboratory experiments with artifically generated velocity turbulence. The experimental results are in qualitative agreement with the theory and show that velocity turbulence tends to reduce the thermal distortion effects and replace the asymmetric bending and spreading by the mean wind velocity with a symmetric blooming. The magnitude of the velocity turbulence effects depends, however, on the ratio of the rms fluctuation-to-the mean velocity, i.e., the gustiness. Since in the atmosphere the gustiness is typically $\leq$ 10-30%, it appears that mechanical turbulence effects will represent at most only a small perturbation on the thermal distortion by the mean wind velocity in the atmosphere.

In Section 4.2, the theoretical model is described together with an approximate solution for the mean intensity profile which is used to show how the turbulence modifies the thermal self-distortion effects from those based on a laminar wind. The laboratory experiments using velocity turbulence generated in a 2 ' long cell are described in Section 4.3. The results presented include detailed contour measurements of the distorted CO_2 beam patterns obtained

in cooperative experiments with the contract monitor. The characteristics of atmospheric turbulence and its expected importance for high power propagation in the atmosphere are discussed in relation to the laboratory experiments in Section 4.4.

4.2 Theoretical Model

A theoretical model to account for the influence of velocity turbulence on the thermal self-distortion of a laser beam by a wind in the atmosphere is developed in this section. Since our interest is mainly in the effect of the turbulence on the thermal lens, several simplifying assumptions are made. First, the usual linear scattering effects on the laser beam intensity which result from temperature turbulence are assumed to be negligible in the absence of absorption or beam heating. This is a reasonable assumption for 10.6μ wavelength propagation since these effects tend to be small for paths less than several km. Moreover, under strong scattering conditions due to normal atmospheric turbulence the effects as far as the beam heating is concerned can be approximately accounted for by assuming an appropriate spreading angle for the mean intensity profile. The second assumption is that the absorption induced beam heating is sufficiently small that it has a negligible effect on the structure or characteristics associated with the normal mechanical turbulence in the atmosphere. Thus, we are considering only the weak interaction limit, which is reasonable for many cases of interest. For example, with a 100 kW CO_2 beam 1 M in diameter propagating through the atmosphere at sea level with a 1 mi/h wind the absorption due to CO_2 and H_2O produces a temperature rise across the beam of order $\Delta T \sim 0.02\ ^\circ C$, which is smaller than the temperature fluctuations (typically $\sim 1\ ^\circ C$) normally present in the atmosphere. The third assumption is that the turbulence is homogeneous and isotropic and can be characterized by a scalar eddy-diffusion coefficient K_h. With these assumptions for the theoretical model we are, in effect, saying that any turbulence effects on the thermal blooming are predominatly due to the influence of velocity fluctuations, i.e., mechanical turbulence, on the heat transfer process. The problem thus reduces to finding the mean temperature profile $\bar{T}$ for a given turbulence structure superimposed on a mean wind velocity transverse to the laser beam axis. The mean temperature T can, in principal, then be used to calculate a distorted intensity profile using the same techniques as with a laminar wind. It should be pointed out, however, that the intensity profile obtained in this way is only a first approximation to the mean intensity which, in general, will also depend on the higher order statistics of the random temperature fluctuations. In the present model scattering effects which can arise from the temperature fluctuations due to the interaction of the turbulence with the beam heating are also ignored.

The equation for the mean temperature T can be found from the expression for conservation of entropy in an incompressible fluid by the usual linearization procedure. Including the absorption heat source term $\alpha\bar{I}$ (where $\bar{I}$ is the mean intensity), we can write (Ref. 15)

$$\frac{\partial \bar{T}}{\partial t} + \bar{U}\frac{\partial \bar{T}}{\partial x} + \overline{\vec{u}\cdot\nabla\theta} = \chi \nabla^2 \bar{T} + \frac{\alpha \bar{I}}{\rho_o c_p} , \tag{21}$$

where $T = \bar{T} + \theta$ is the temperature* and $\vec{v} = \bar{U}\hat{x} + \vec{u}$ is the wind velocity. The overbar indicates an average and θ and $\vec{u}$ are the random, zero-mean temperature and velocity fluctuations, respectively. ($\chi = K/\rho_o c_p$ is the thermal diffusivity of the gas). Equation 21 differs from the nonturbulent heat equation only by the presence of the term $\overline{\vec{u}\cdot\nabla\theta}$. The usual procedure at this point is to make use of the fact that $\nabla\cdot\vec{u} = 0$ to write $\overline{\vec{u}\cdot\nabla\theta} = \nabla\cdot\overline{\vec{u}\theta}$, and to assume that

$$\overline{u_i\theta} = -(K_h)_{ij}\frac{\partial \bar{T}}{\partial x_j} , \tag{22}$$

where $(K_h)_{ij}$ is a second rank tensor in general. The coefficient $(K_h)_{ij}$ has the same dimensions as the thermal diffusivity χ and is known as the turbulence-or eddy-transport coefficient. For homogeneous and isotropic turbulence the eddy-transport coefficient becomes a scalar constant K_h, and for the steady-state case Eq. (21) now becomes

$$\bar{U}\frac{\partial \bar{T}}{\partial x} - (K_h + \chi)\nabla^2\bar{T} = \frac{\alpha \bar{I}}{\rho_o c_p} . \tag{23}$$

The effect of turbulence on the mean temperature profile is thus accounted for simply by a diffusion-like heat transfer term.

An order of magnitude estimate of the condition necessary for the turbulent diffusion to be important in the formation of the thermal lens can be found by comparing the heat transfer rates $1/\tau_d$ and $1/\tau_c$, associated, respectively, with the diffusion and convection terms in Eq. (23). Thus, from Eq. (23) we obtain for diffusion $1/\tau_d \sim 2(K_h + \chi)/a^2$ and for the convection due to the mean wind velocity $1/\tau_c \sim \bar{U}/2a$, where a is the laser beam radius. Since for air the thermal diffusivity $\chi \approx 0.2$ cm^2/sec, which can usually be neglected in comparison with the eddy diffusivity K_h, the importance of the turbulent diffusion in relation to the mean flow is proportional to the ratio $\tau_c/\tau_d \approx 4K_h/\bar{U}a$. The eddy diffusion coefficient K_h is of the order $u'\ell_c$, (Ref. 16) where u' is the rms velocity fluctuation and ℓ_c is a characteristic scale length for the turbulence.

* Note that T represents the deviation from the neutral vertical temperature profile which decreases with altitude by the adiabatic lapse rate of 10^{-2} °C/m.

If the diffusion concept is to be applied to the heat transfer from the laser beam of radius a by the velocity turbulence, the eddy diffusivity K_h can only represent turbulent scale sizes $\ell \lesssim a$. Another way of saying it is that the diffusion process is a valid description over the dimension of interest only if there is an interaction between a large number of eddies ocurring over this dimension. The ratio of the turbulent diffusion heat transfer to that by the mean flow velocity is then on the order of

$$\frac{\tau_c}{\tau_d} = \frac{4K_h}{\bar{U}a} \lesssim 4\frac{u'}{\bar{U}} , \tag{24}$$

which must be $\lesssim 1$ for the turbulence to be important. Since in the atmosphere under typical conditions $u'/\bar{U} \lesssim 0.1 - 0.3$, we do not expect the turbulence to have a dominant effect over the thermal distortion associated with the mean wind velocity.

According to Eq. (23), the problem of determining the mean temperature profile for the laser beam in an absorbing turbulent flow is effectively that of combined convection and conduction heat transfer. Aleshkevich and Sukhorukov (Ref. 17) have considered this problem and obtained the solution for a gaussiam beam in the form of an expansion in x and y near the beam axis. Taking the wind to be in the x-direction and dropping the axial heat diffusion term $\partial^2\bar{T}/\partial z^2$, their solution for Eq. (23) can be written

$$\bar{T}(x,y) - \bar{T}(0,0) = \frac{\alpha P_o}{4\pi K'} \left\{ 2T_x\left(\frac{x}{a}\right) - T_{xx}\left(\frac{x}{a}\right)^2 - T_{yy}\left(\frac{y}{a}\right)^2 + \cdots \right\} , \tag{25}$$

where $K' = K_h \rho_o c_p + K$, K is the thermal conductivity, a is the 1/e intensity radius of the gaussian laser beam and*

$$T_x = \gamma e^{2\gamma^2} \left[K_o(2\gamma^2) - K_1(2\gamma^2) \right] + \tfrac{1}{2}\gamma^{-1} , \tag{26}$$

$$T_{xx} = \left[(4\gamma^2 - 1) K_1(2\gamma^2) - 4\gamma^2 K_o(2\gamma^2) \right] e^{2\gamma^2} + \frac{1}{2\gamma^2} , \tag{27}$$

$$T_{yy} = e^{2\gamma^2} K_1(2\gamma^2) - \frac{1}{2\gamma^2} . \tag{28}$$

* There is apparently an error in Ref. 17, regarding the signs of T_{xx} and T_{yy}. For Eqs. (4) and (5) (in the same reference) to be consistent with Eq. (2) the minus signs in Eq. (2) should be changed to plus signs. It should also be noted that the wind is taken to be in the y-direction in Ref. 17.

Here, the parameter $\gamma = \bar{U}a/4(K_h + \chi)$ is the ratio of the convection-to-eddy diffusion heat transfer terms in Eq. (23), which is simply the reciprocal of the ratio τ_c/τ_d defined above. The quantities T_x, T_{xx} and T_{yy}, which depend only on γ, are given in Eqs. (26) - (28) in terms of the modified Bessel functions K_n^* (Ref. 18) and are shown in Fig. 26 for $0 \leq \gamma \leq 6$. When $\gamma \to 0$, diffusion heat transfer, which here we assume to be due to the turbulence, becomes dominant in comparison with convection. As γ becomes larger than one the convective heat transfer associated with the mean wind velocity becomes dominant.

It should be pointed out that the expression for the mean temperature in Eq. (25) is only accurate for $|x/a|, |y/a| \ll 1$; and, in addition, Eq. (25) is not suitable for use in the iterative computer code for calculating thermal distortion effects since it only applies for a gaussian beam while the computer procedure requires a general solution for arbitrary intensity profiles. Equation 25 can be used, however, to derive a perturbation type of expression and define a scaling parameter to account for turbulence effects on the thermal distortion.

Assuming a collimated gaussian beam consistent with the mean temperature profile in Eq. (25), a perturbation expression for the thermally distorted mean intensity can be written as (assuming $\alpha z \ll 1$) (Ref. 19)

$$\bar{I}(x,y,z) = I_u(x,y,z)\, e^{-\alpha z}\, e^{\psi} , \tag{29}$$

where I_u is the undistorted gaussian intensity and

$$\psi = - \frac{(dn/dT)\, z^2}{2\, n_o} \left\{ \nabla_\perp^2 \bar{T} - 2 \frac{x}{a^2} \frac{\partial \bar{T}}{\partial x} - 2 \frac{y}{a^2} \frac{\partial \bar{T}}{\partial y} \right\} . \tag{30}$$

which accounts for the thermal lens effects.

Making use of Eq. (25) in Eq. (30) the expression for the thermal distortion exponent ψ is

$$\psi = - N_Y \left\{ 2\, T_x(\gamma) \left(\frac{x}{a}\right) + T_{xx}(\gamma) \left(1 - 2\frac{x^2}{a^2}\right) + T_{yy}(\gamma) \left(1 - 2\frac{y^2}{a^2}\right) \right\} , \tag{31}$$

* In Ref. 17, the K_n are referred to as Macdonald functions.

where

$$N = \frac{(-dn/dT)\,\alpha\, P_o z^2}{\pi\, n_o \rho_o c_p \bar{U} a^3} \quad , \tag{32}$$

which is the familiar distortion parameter defined for the nonturbulent convective thermal lens associated with the mean velocity $\bar{U}$.

It can be seen qualitatively from Eq. (31) that for fixed values of N and mean wind velocity $\bar{U}$ the effect of increasing the level of turbulence as measured by K_h will lead to an increase in on-axis intensity since $\gamma \sim 1/K_h$.

Intensity profiles through beam center along the wind direction have been calculated using Eq. (29) and results are shown in Fig. 27 for the case N = 1. The parameter $\gamma^{-1} = 4K_h/\bar{U}a \sim 4u'/\bar{U}$ provides a measure of the relative importance of turbulent heat diffusion and since in Fig. 27 N is constant, if we consider the laser beam parameters and mean wind $\bar{U}$ to be fixed, the changes in γ^{-1} may be regarded as changes in K_h or u'. For values of $\gamma^{-1} \lesssim 1$ there is little effect on the intensity profiles which are decreased and shifted into the wind characteristic of the wind or convection dominated thermal lens. As the value of γ^{-1} (or equivalently K_h or u') increases, the turbulent diffusion heat transfer reduces the temperature gradients and tends to restore the intensity profile to the undistorted condition (N = 0) as shown in Fig.(27).*

In Fig. 28, the dependence of I_R, which is the on-axis mean intensity normalized by the attenuated undistorted value, on the parameter $\gamma^{-1} \sim 4u'/\bar{U}$ is shown for the values of N = 0.5 and 1. As the turbulent diffusivity K_h (or equivalently the rms velocity u') increases, so that γ^{-1} increases from ~ 1 to 10, the on-axis intensity is approximately doubled for the case N = 1 and for the caxe N = 0.5 there is an increase by a factor of ~ 1.4. The increase in on-axis intensity by the turbulent diffusion is due mainly to the reduction in beam bending which can be seen in Fig. 27. If the turbulent diffusion parameter γ^{-1} can continue to be increased beyond 10 the thermal lens effects can eventually be eliminated as shown in Fig. 28.

---

* It should be pointed out that since the temperature expresssion (Eq. 25) neglects terms higher than second order in x and y, the intensity profiles in Fig. 27 are only accurate for $|x/a| \ll 1$; and, as N and γ increase the curves become increasingly inaccurate at the off-axis points. This is why the profiles do not converge for $\gamma^{-1} \ll 1$ to the perturbation results shown in Ref. 19, Fig. 2, as they should. The results in Fig. 27 are correct near the beam axis, however, and are also useful for showing qualitatively the effects of turbulence on the thermal distortion.

4.3 Turbulence Cell Experiments

The approach used in the experimental program is to examine the thermal self-distortion of a laser beam in a laboratory simulation using artificially generated velocity turbulence. One of the considerations involved in finding a suitable method for generating the turbulence is the requirement of a small mean flow velocity to enable strong thermal lens effects to be obtained with the small ($\sim$ 30 W) laser power available. Another constraint is that the structure of the turbulence should include a range of scale sizes from much smaller to on the order of or larger than the laser beam diameter to provide a significant interaction between the beam and the turbulence. Although the use of grids was considered initially this approach was not pursued since it appeared doubtful that fully developed, homogeneous turbulence would be obtained at the required low flow velocities and, hence, small Reynolds numbers. After investigating several types of nozzle arrays the necessary requirements appeared to be met in a turbulence cell consisting of a series of opposing jets enclosed in a box with perforated walls on either side as shown by the sketch in Fig. 29. After initial tests with a 3 in. long model this arrangement was extended to a 2 m long cell for providing a region of nearly homogeneous and isotropic turbulence with essentially zero mean velocity. The effect of a mean wind velocity is obtained by moving the laser beam across the stationary turbulence cell as indicated in Fig. 29. Self-induced thermal distortion experiments are conducted using pure CO_2 in the turbulence cell with the turbulence level being monitored by measuring the gas pressure at one of the plenum chambers feeding the tubes with a water manometer. The turbulence cell initially was not enclosed. However, it was found necessary to enclose it within a box with an open port at the top to prevent the stratification and mixing of CO_2 with air which produced undesirable refraction or bending effects at the lower turbulence levels.

In Fig. 30 results for the turbulence effects on a stationary beam are shown with images of the CO_2 beam pattern recorded using Kalvar film. With no turbulence in the cell, which was oriented horizontally, a vertical natural convection velocity is established that leads to the downward deflection and characteristic kidney or crescent shape seen in Fig. 30. With turbulence in the cell and the same amount of absorption and laser power, the beam patterns become symmetrical and decrease in area as the pressures indicating the turbulence levels increase from 1.5 to 16 cm of H_2O. This agrees qualitatively with what is predicted by the theoretical model in Sec. 4.2.

Figure 31 shows photographs of the patterns near the exit window of the turbulence cell of a HeNe beam that is superimposed on the CO_2 beam. The HeNe beam was well collimated and about the same diameter as the CO_2 beam at the exit window of the turbulence cell. The HeNe beam patterns in Fig. 31 show that the turbulence effects on the stationary CO_2 beam lead to the symmetric spreading effects that are associated with conduction or diffusion dominated thermal blooming. The nearly symmetrical patterns which represent $\sim$ 5 sec exposures indicate that the turbulence

structure is stationary and nearly homogeneous and isotropic across the beam. The pronounced ring structure in the HeNe beam patterns for the strong thermal blooming case with 27 W in the CO_2 beam are believed to be due to interference effects that are enhanced since the CO_2 beam is about one-half the size of the collimated HeNe beam at the entrance window of the turbulence cell. Thus, the central rays of the HeNe beam that are spread by blooming eventually intercept and interfere with the outer rays that are unaffected by the CO_2 beam induced thermal lens.

Figure 32 shows intensity profiles of a stationary CO_2 beam with the same (6 cm H_2O) turbulence level for different laser beam powers. A 35 μ pinhole was used with the detector which was scanned slowly (typically 1 - 3 minutes in duration) across the beam to provide an estimate of the mean intensity profile with the turbulence. With no mean wind velocity or beam motion the thermal lens effects with turbulence should be the same as the pure conduction blooming case but with the thermal diffusivity of the gas, $\chi = K/\rho_o c_p$ replaced by the turbulent diffusion coefficient, K_h. For this case the intensity expression, Eq. (29), becomes (Ref. 20)

$$\bar{I}(r) = I_u(r)e^{-\alpha z} \exp\{-N_c[2e^{-r^2} - 1]\} \quad , \tag{33}$$

where $r = (x^2 + y^2)^{\frac{1}{2}}/a$,

$$I_u(r) = \frac{P}{\pi a^2} e^{-r^2} \quad , \tag{34}$$

and

$$N_c = \frac{(-dn/dT)\, P z}{\pi n_o \rho_o c_p K_h a^2} \left[1 - \frac{(1 - e^{-\alpha z})}{\alpha z}\right] \quad . \tag{35}$$

According to Eq. (33), the mean intensity profile with a stationary beam in turbulence (or, also in the case where thermal conduction is dominant) is reduced near the axis for $r < (\ell n 2)^{\frac{1}{2}} \sim 0.835$; and, for $r > 0.835$ the intensity is increased, which, as the thermal blooming becomes stronger, tends to change the gaussian profile to a donut shape. The changes in the distorted intensity profiles with increasing power (which for fixed turbulence intensity increases N_c) are seen in Fig. 32 to be in qualitative agreement with this predicted behavior.

The mean on-axis intensity normalized by the attenuated undistorted value, $I_R(0)$, is found from Eq. (33) for the stationary beam in turbulence to be given by

$$I_R(0) = \frac{\bar{I}(0)}{I_u e^{-\alpha z}} = e^{-N_c} \quad . \tag{36}$$

Although Eq. (33) is a perturbation expression, the result for the mean on-axis intensity in Eq. (36) agrees with the exact analytic expression $\bar{I}_R(0) = \text{sech}^2 N_c^{\frac{1}{2}}$ (Ref. 21) within $\sim 12\%$ for $N \leq 1$. In Fig. 33 measured values are shown for the mean on-axis intensity as a function of power at the turbulence level associated with the pressure of 1.5 cm of H_2O. The results are seen to follow an exponential decrease as predicted on the basis of Eqs. (35) and (36). This provides a convenient optical method for determining the eddy-diffusion coefficient of the turbulence since everything in the expression for N_c in Eq. (35) is known except K_h. For the data shown in Fig. 33 with a "turbulence level" of 1.5 cm of H_2O the value $K_h \sim 3.5$ cm^2/sec is obtained. This value can be compared with the estimate of $K_h \sim 1.2$ cm^2/sec for the 10 cm H_2O turbulence level which is based on data obtained with a single 3/8 in. long hot wire probe. The rms velocity fluctuation measured for this case was $u' \sim 2$ cm/sec and a crude estimate for the outer scale length of the turbulence, $\ell_t \sim 0.6$ cm was obtained from the hot wire anemometer signal with the probe mechanically scanned at 25 cm/sec through the turbulence. Additional studies comparing values of K_h obtained optically with hot wire anemometer measurements are in progress to check the theoretical model and establish the nature of the turbulence structure as a function of the different pressure settings given in cm of H_2O. The pertinent experimental parameters for the stationary beam turbulence results of Figs. 32 and 33 are given in Table III.

The results for turbulence effects on the thermal distortion with beam motion or, equivalently, wind are shown in Figs. 34 and 35. The intensity profiles were measured through beam center along the direction of beam motion which in this case was in the downward direction (see Fig. 29). Several traces were obtained for each case and the results indicate both the repeatability of the experiments and the low level of intensity fluctuations produced by the turbulence. For the no turbulence cases in the lower left-hand corners of Figs. 34 and 35, the peak intensity is shown to be reduced to ~ 36 percent of the undistorted value and shifted into the wind $\sim 1.65\ a_o$. For the same laser power and beam motion conditions but with velocity turbulence, the measured intensity profiles on the right-hand side of Figs. 34 and 35 show the distortion and beam deflection being reduced with the on-axis intensity increased as the pressure setting for the turbulence increases from 1.5 to 20 cm of H_2O. The only important difference between the data in Figs. 34 and 35 is in the "wind" or beam motion velocities, which are 2 and 1 cm/sec, respectively.

Since the power level used in Fig. 34 is twice that in Fig. 35, the same value of $N \sim 11$ is obtained for each case, however, as is also indicated by comparing the laminar wind (i.e., beam motion only) cases in each figure. For the maximum turbulence level of 20 cm H_2O with $\bar{U} = 2$ cm/sec (Fig. 34) the peak intensity is increased to ~ 60 percent of the undistorted value. With $\bar{U} = 1$ cm/sec (Fig. 35) and the maximum turbulence level of 16 cm H_2O the peak intensity is increased to ~ 75 percent of the undistorted value. The greater increase in the peak intensities observed at all turbulence levels with $\bar{U} = 1$ cm/sec in Fig. 35 as compared with $\bar{U} = 2$ cm/sec is consistent with the theoretical results of Figs. 27 and 28 since $\gamma^{-1} = 4 K_h/\bar{U}a \sim 4 u'/U$ for Fig 35 is twice that for Fig. 34 at the same turbulence level. Based on the optically determined value of $K_h \sim 3.5$ cm^2/sec from Fig. 33 for the 1.5 cm H_2O turbulence level and using the average beam radius, $a \sim 0.26$ cm one obtains for the parameter $\gamma^{-1} = 4 K_h/Ua$ the values of 27 and 54, respectively, for the 1.5 cm H_2O case in Figs. 34 and 35. If we assume that $K \sim u'a$, the rms velocity associated with the 1.5 cm of H_2O turbulence level is ~ 13.5 cm/sec, which is much greater than the 1 or 2 cm/sec beam motion or "wind" velocities used in Figs. 34 and 35.

It should be pointed out for consideration in future experiments that natural convection effects may be a problem under experimental conditions similar to those in Figs. 34 and 35 without turbulence. This is suggested by the relatively small beam deflection observed for the laminar wind case which for this value of $N(\sim 11)$ should be about $3a_o$ - $4a_o$ instead of $\sim 1.65a_o$. Indeed, if the natural convection velocity is estimated (assuming the beam to be stationary) using the expression (Ref. 20)

$$v_{nc} \sim \left(\frac{\alpha g P}{\rho_o c_p T}\right)^{1/3} \tag{37}$$

with the conditions: $\alpha = 2 \times 10^{-3}$ cm^{-1}, $g = 9.8 \times 10^2$ cm sec^{-2}, $\rho = 1.73 \times 10^{-3}$ g cm^{-3}, $c_p = 0.86$ J g^{-1} °K^{-1}, $T = 290$°K, we obtain $v_{nc} \sim 1.66\ P^{1/3}$ cm/sec, with P given in watts. Thus, for P = 8.8 W (Fig. 35) $v_{nc} \sim 3.4$ cm/sec which, since the beam motion is downward and at a velocity of only 1 cm/sec, may account for the smaller beam deflection because N is effectively reduced by the influence of v_{nc}. The natural convection effects may be reduced by orienting the cell vertically or possibly by making the beam motion in the horizontal plane.

More detailed results for the thermal distortion effects with velocity turbulence have been obtained in cooperative experiments with the contract monitor. A high speed ($\sim$ 8000 rpm) rotating mirror scanner was used in conjunction with a liquid nitrogen cooled Hg Cd Te detector equipped with a 0.0039 in. diam. aperture to obtain time resolved (~ 100 μsec scan duration) intensity profiles across the beam. The beam motion across the scanner was provided by the same mirror

used to simulate a mean wind velocity (see Fig. 29). The intensity profiles were displayed on a 545 B Tektronix oscilloscope with a 1A7A differential preamplifier and were recorded on 35 MM movie film at 3600 in/min. Detailed constant intensity contours were obtained from the measured intensity profiles approximately 39 cm beyond the exit window of the 2 m turbulence cell and are shown in Figs. 36-46.

The undistorted beam contours were obtained with air in the cell (i.e., no absorption) and are shown in Fig. 36. The input and output 1/e beam radii measured from individual scans through beam center, perpendicular to the direction of beam motion, (the beam motion is from right-to-left in Figs. 36-46) are a_i = 0.21 cm at the cell input and a_o = 0.38 cm in the output or detector plane. The contours shown in Figs. 37-46 were obtained with pure CO_2 in the cell and based on a transmission measurement with P ~ 2 W and a low turbulence level (~ 6 cm H_2O) the value αt = 0.37 is obtained for the cell absorption coefficient-length product. The laser beam power entering the turbulence cell in Figs. 37-40 is P = 21 W and the beam translation velocity is v = 2 cm/sec, which gives the value N = 11 for the convection dominated distortion parameter (Eq.(1)). The distorted contours are shown in Fig. 37 with the CO_2 stationary in the cell (i.e., the laminar wind case), and with low (6 cm H_2O), medium (10 cm H_2O) and high (16 cm H_2O) turbulence in the cell in Figs. 38, 39, and 40, respectively. In Fig. 37, with no turbulence the familiar crescent shaped distortion is evident with the peak intensity (denoted by the x) shifted ~ 2.6 a_o in the direction of beam motion. The convective thermal distortion spreads the beam as can be seen by comparison with the dashed 1/e contour obtained with air in the cell, and the resulting reduction in intensity can be expressed as

$$I_{EFF} = \frac{\text{AREA 1/e CONTOUR-AIR}}{\text{AREA 1/e CONTOUR}} \quad . \qquad (38)$$

For the no-turbulence case in Fig. 37 I_{EFF} = 0.24. With velocity turbulence superimposed on the same 2 cm/sec beam motion the distorted beam patterns become more symmetrical with the peak intensity shifting back to the undistorted beam axis with increasing turbulence in Figs. 38-40. Also, in Fig. 40, with high turbulence I_{EFF} = 0.375, which represents approximately a 55% increase as a result of the reduction in thermal blooming by the turbulent diffusion.

In Figs. 41 and 42, the cases of stationary CO_2 and medium turbulence are compared for the conditions, P = 21 W and the beam translation velocity of v = 15 cm/sec. For these conditions N = 4.3, and for the no-turbulence case (Fig. 41) the peak intensity is shifted ~ $2a_o$ and I_{EFF} = 0.33. With medium turbulence (Fig. 42) the beam deflection is reduced and the crescent shape is no longer evident. However, no increase in I_{EFF} is obtained with the turbulence.

In Figs. 43-46, the cases of stationary CO_2 and low, medium and high turbulence are compared for the conditions of P = 11W and a beam translation velocity of 5 cm/sec. For this case N = 2.26 and with no turbulence (Fig. 43) the peak

intensity is shifted $\sim 1.75\ a_o$ and the effective intensity is $I_{EFF} = 0.54$. With low, medium or high turbulence the beam deflection is reduced as expected and the thermal distortion tends to become somewhat more symmetrical. It is interesting to note, however, that for the low turbulence case (Fig. 44) I_{EFF} is reduced $\sim 24\%$ below the stationary CO_2 case. Although I_{EFF} increases to about the same value as in the nonturbulent case with medium turbulence there is no further increase in I_{EFF} at the high turbulence level (Fig. 46). The relative ineffectiveness of the turbulence in increasing I_{EFF} for this case as compared with the 2 cm/sec contours in Figs. 37-40 can be attributed to the higher beam translation velocity of 5 cm/sec, which for the same turbulence conditions (i.e., the same value of K_h) reduces the parameter $\gamma^{-1} = 4\ K_h\ /\bar{U}a$ by a factor of 2.5.

The results obtained for the convective thermal distortion in the presence of velocity turbulence show that the effect of the turbulence is to change the asymmetric wind type distortion, which is a combination of focussing and defocusing distortion. The experimental results also indicate, in qualitative agreement with the theory in Section 4-2, that for a given turbulence level its influence on the thermal distortion is inversely proportional to the mean velocity; and, that the rms velocity u' must be much larger than the mean $\bar{U}$ for any appreciable reduction in the thermal blooming to result from the turbulence diffusion.

4.4 Discussion

The experimental results shown in Sec. 4.3 are in qualitative agreement with the theoretical model developed in Sec. 4.2 in which an eddy diffusion coefficient K_h is used to account for the effects of mechanical turbulence on thermal blooming. Based on these results, it is found that velocity turbulence in the presence of a mean wind across the laser beam has the tendency to destroy the combined focusing and defocusing of the pure convective thermal lens and replace it with a symmetric two dimensional blooming or spreading. Also, according to the theoretical model, the velocity turbulence can reduce the thermal distortion and spreading effects if conditions are such that the parameter $\gamma^{-1} = 4K_h/\bar{U}a$ is much larger than one. In the laboratory turbulence experiments relatively large effects on the thermal distortion were observed which is in agreement with the preliminary estimates for values of $\gamma^{-1} >> 1$ that are based on the value of K_h determined optically for one of the turbulence levels. Measurements of K_h for all the different levels of cell turbulence used in the experiments are in progress which will be used in the quantitative evaluation of the thermal distortion results in terms of the parameter γ^{-1}.

Although the cell turbulence structure clearly does not accurately simulate that found in the atmosphere the laboratory experiments together with the eddy diffusion model can provide a qualitative estimate of the relative importance and effect of velocity turbulence on atmospheric propagation. By using typical values for K_h in the atmosphere the parameter γ^{-1} can be used to relate the experimental results to atmospheric propagation conditions. The eddy diffusion coefficient $K_h \sim u'\ell$, as indicated in Sec. 4.2, where u' is referred to as the

mixing velocity and ℓ is the mixing length. Using this definition for K_h, the parameter $\gamma^{-1} \approx 4(u'/\bar{U})\ (\ell/a)$. Since the length ℓ can be $\gtrsim 10^3$cm corresponding to the largest eddy sizes of the order of the outer scale length L_o, and $4(u'/\bar{U})$ is typically of order unity, it would appear that γ^{-1} can indeed be $\gg 1$ for the typical beam radius $a \sim 10$ cm. Thus, on this basis, our original predictions (Ref. 14) were that velocity turbulence in the atmosphere could be expected to be an important factor in reducing thermal blooming effects. It has been pointed out by Bradley and Hermann (Ref. 22), however, that the effects of eddy sizes ℓ greater than the beam radius a cannot be represented by an eddy diffusion coefficient since the diffusion model implies the interaction of many eddies over the dimension of interest. The effect of the larger eddy sizes $\ell > a$ must be viewed simply as a slow variation in the wind velocity vector that can be accounted for approximately by summing the squares of the long wavelength components with the square of the mean velocity. Thus, if we assume that turbulent eddy sizes ℓ exist that range from much smaller to much larger than the beam radius a, which is typical for atmospheric propagation, the maximum ℓ producing a diffusion effect on the laser beam is of order a, the beam radius. The parameter γ^{-1} is thus simply of the order $4\ (u'/\bar{U})$, which, if the dependence of u' on ℓ is ignored and u' is taken to be the rms velocity, gives $\gamma^{-1} \lesssim 1$ for typical conditions in the atmosphere.

A somewhat more precise estimate of γ^{-1} for typical atmospheric propagation conditions may perhaps be obtained by examining published data for K_h. Lettau (Ref. 23), for example, indicates that up to 1 km altitude K_h can range from 1 to 10^5 cm^2/sec depending on the mixing length ℓ, as shown in Fig. 47. Also shown in Fig. 47 is the molecular diffusivity $\chi \sim 0.2$ cm^2/sec for air, which is clearly unimportant in comparison with turbulent diffusion. If we assume for the laser beam radius a = 10 cm, and take for the mixing length ℓ = a, the corresponding mixing velocity u' varies from ~ 1 to 10 cm/sec as shown by the width of the shaded region in Fig. 47. Since the velocity fluctuations are known to be proportional to the mean velocity $\bar{U}$, the range in mean velocity associated with this variation in u' is given approximately by the mixing velocities of the largest eddy sizes which, from Fig. 47, vary from ~ 10 to 200 cm/sec. Using these extreme values for $\bar{U}$ and taking $K_h = 10$ to 10^2 cm^2/sec for $\ell = 10$ cm in Fig. 47, we find that $\gamma^{-1} \lesssim 0.4 - 0.2$ for a 10 cm radius beam. The less than or equal condition accounts for the fact that the mean velocity must either be larger than or at least as great as the largest scale length velocity fluctuations.

If, as an alternate approach, we consider the Kolmogorov similarity theory of turbulence (Ref. 24) we find that except for the smallest eddy sizes of order ℓ_o, the inner scale of turbulence, the velocity fluctuations $u'(\ell)$ associated with the eddy size ℓ are proportional to $\ell^{1/3}$. Taking the mean velocity $\bar{U}$ as an upper limit for the velocity fluctuations of the largest eddy sizes L_o, we then

have that $u' \sim \bar{U}\ (\ell/L_o)^{1/3}$. Since ℓ must be $\lesssim$ a for the eddy diffusion model to be valid for the laser beam of radius a, the diffusion coefficient is then $K_h = u'(\ell)\ \ell \lesssim u'(a)\ a$, and thus $\gamma^{-1} \lesssim 4\ u'(a)/\ \bar{U} \sim 4\ (a/L_o)^{1/3}$, which for the values a = 10 cm and $L_o = 10^3$ cm gives $\gamma^{-1} \lesssim 4\ (10)^{-2/3} \sim 0.86$. Although this gives an estimate of γ^{-1} somewhat larger than the data shown in Fig. 47, the difference is not significant since according to Figs. 27 and 28 the turbulence effects on the thermal distortion are negligible for $\gamma^{-1} \lesssim 1$.

From these considerations it appears then that velocity turbulence effects on thermal blooming in the atmosphere will usually be insignificant. This conclusion is, of course, in agreement with the intuitive feeling that the velocity fluctuations, which are usually smaller than the mean, cannot be as effective in removing heat from the beam as the mean flow and, hence, have proportionately less effect on the thermal lens. Possible exceptions when velocity turbulence may become important are when the mean velocity $\bar{U}$ of the air relative to the beam approaches zero with finite turbulent velocity fluctuations remaining. Although it is doubtful if such conditions can occur with a stationary beam in the atmosphere except, possibly, under strong free convection mixing conditions near the ground, they can occur with beam translation or slewing when the beam or points along the beam move with the mean flow velocity. In this case, the turbulent diffusion may reduce the thermal blooming and distortion effects from those predicted solely on the basis of natural convection and thermal conduction in the regions of low or zero relative velocity.

REFERENCES

1. F. G. Gebhardt and D. C. Smith, Annual Report on Army Contract DAAB07-70-C-0204 with U. S. Army Electronics Command for period 30 April 1970 to 29 April 1971; United Aircraft Research Laboratories Report UAR-K921004-4, July 1971.

2. L. C. Bradley and J. Herrmann, "Numerical Calculation of Light Propagation in a Nonlinear Medium," J. Opt. Soc. Am., 61, p. 668, May 1971.

3. J. N. Hayes, P. B. Ulrich and A. H. Aitken, "Effects of the Atmosphere on the Propagation of 10.6 Micron Laser Beams," Appl. Opt., 11, p. 257, February 1972.

4. F. G. Gebhardt and D. C. Smith, "Effects of Diffraction on the Self-Induced Thermal Distortion of a Laser Beam in a Crosswind," Appl. Opt., 11, p. 244, February 1972.

5. J. Wallace, "Effects of Nonlinear Refraction at 10.6 μm on the Far-Field Irradiance Distribution," J. Opt. Soc. Am., 62, p. 373, March 1972.

6. Others who have developed computer codes for investigating nonlinear propagation effects with a wind include: P. M. Livingston and H. Breaux, at Ballistic Research Laboratories, Aberdeen, Md.,; C. B. Hogge, J. Kenemuth, R. Butts and W. Trebilcock, AFWL, Kirtland AFB, Albuquerque, N.M.; and A. J. Glass, Dept. of Electrical Engineering, Wayne State University, Detroit, Michigan.

7. W. H. Christiansen, G. J. Mullaney and A. Hertzberg, "Absorption in CO_2 at 10.6 μ with Retational Line Overlap," Appl. Phys. Letters, 18, p. 385, 1 May 1971.

8. R. A. Chodzko and S. C. Lin, "Transition from Laminar to Turbulent Flow in a Laser-Induced Convection Column," Appl. Phys. Letters, 16, p. 434, 1 June 1970.

9. F. G. Gebhardt and D. C. Smith, "Effects of Diffraction on the Self-Induced Thermal Distortion of a Laser Beam in a Crosswind," Appl. Opt., Vol. 11, pp. 244-248, February 1972.

10. A. J. Glass, "Thermal Blooming in Gases," Opto-Electronics, Vol. 1, pp. 174-178, 1969.

11. A. D. Wood, M. Camac and E. T. Gerry, "Effects of 10.6 μ Laser Induced Air Chemistry on the Atmospheric Refractive Index," Appl. Opt., Vol. 10, pp. 1877-1884, August 1971.

12. F. G. Gebhardt and D. C. Smith, "Kinetic Cooling of a Gas by Absorption of CO_2 Laser Radiation," Appl. Phys. Letters, Vol. 20, p. 129-132, February 1972.

13. J. Wallace and M. Camac, "Effects of Absorption at 10.6-μ on Laser Beam Transmission," J. Opt. Soc. Am., Vol. 60, pp. 1587-1594, December 1970.

14. F. G. Gebhardt, D. C. Smith, R. G. Buser, and R. S. Rohde, "Experimental Studies of the Effects of Turbulence on Thermal Blooming," Opt. Soc. of America, Spring 1972 Meeting, New York, 12 April 1972.

15. See, e.g., J. L. Lumley and H. A. Panofsky, The Structure of Atmospheric Turbulence, John Wiley & Sons, New York (1964), p. 63, Eq. (2.18).

16. J. O. Hinze, Turbulence, McGraw-Hill, New York (1959), Sec. 1-9, p. 42.

17. V. A. Aleskhevich and A. P. Sukhorukov, "Deflection of Powerful Light Beams Under the Influence of Wind in Absorbing Media," JETP Letters, Vol. 12, pp. 77-79, (20 July 1970).

18. M. Abramowitz, and I. A. Stegum, Handbook of Mathematical Functions, U.S. Government Printing Office, Washington, D. C. 1964, p. 374. (Dover Publications, Inc., New York, 1965).

19. F. G. Gebhardt and D. C. Smith, "Self-Induced Thermal Distortion in the Near Field for a Laser Beam in a Moving Medium," IEEE J. of Quantum Electronics, Vol. QE-7, pp. 63-73, February 1971.

20. D. C. Smith, "Thermal Defocusing of CO_2 Laser Radiation in Gases," IEEE Journal of Quantum Electronics, Vol. QE-5, pp. 600-607, December 1969.

21. D. C. Smith, "An Analytical Solution of the Self-Induced Thermal Distortion of Laser Radiation in an Absorbing Medium," United Aircraft Research Laboratories Report UAR-H289, November 1969.

22. L. C. Bradley and J. Herrmann, private communication, May 1972.

23. H. Lettau, "Compendium of Meteorology," T. F. Malone, ed., pp. 320-333, American Meteorological Society, Boston, 1951; American Institute of Physics Handbook, Second Edition, D. E. Gray, ed., pp. 2-143, 144, McGraw-Hill, New York 1963.

24. V. I. Tatarski, Wave Propagation in a Turbulent Medium, (McGraw-Hill, New York, 1961), Ch. 2.

TABLE I

EXPERIMENTAL PARAMETERS
HIGH PRESSURE GAS CELL

$\lambda = 10.6\ \mu$
$z = 114$ cm (Total Pathlength)
$t = 103$ cm (Cell Length)
F = Focal Range

Date		F/z	a_i/a_o	a_i mm	v cm/s	αt
6/23	Focused	1	2.6	3.1	0.5, 1	0.415
7/6	Collimated	∞	0.9	2.4	0.5, 1	0.415
8/8	Focused	1	7.4	3.4	1	0.415
8/8	Collimated	∞	0.97	3.4	1	0.415
8/9	Focused	0.74	2.4	3.6	1	0.415
8/9	Focused	1	7.5	3.6	1	0.415
8/17	Focused	0.74	2.12	3.4	1	0.415
8/17	Focused	1	7.1	3.4	1	0.415
8/17	Focused	1.26	4.47	3.4	1	0.415
8/17	Focused	>1.26	2.83	3.4	1	0.415
8/26	Focused	1	7.1	3.4	1	0.13, 0.44, 2.3

TABLE II

MATERIAL PROPERTIES

	CS_2 (293°K)	Air (1 atm) (300°K)	CO_2 (1 atm) (300°K)
n	1.6319 (D)	1.000263	1.00417
$-dn/dT$, $^oK^{-1}$	0.72×10^{-3}	0.875×10^{-6}	1.39×10^{-6}
ρ, g cm^{-3}	1.26	1.175×10^{-3}	1.79×10^{-3}
c_p, J/g°C	0.95	1.006	0.86
K, W/cm°C	1.61×10^{-3}	2.6×10^{-4}	1.66×10^{-4}
χ, cm^2/sec	1.35×10^{-3}	2.2×10^{-1}	1.08×10^{-1}
μ, μ poise	3.66×10^3	1.82×10^2	1.46×10^2

TABLE III

EXPERIMENTAL CONDITIONS FOR FIGURES 32 & 33

STATIONARY BEAM IN TURBULENCE

Cell Length t = 2 m
Total Path z = 2.08 m
αt = 0.371 (100% CO_2)
T = 290°K

	Turbulence Level-CM H_2O	a_i, mm	a_o, mm
Fig. 32	6	1.23	2.42
Fig. 33	1.5	1.2	1.9

LIST OF FIGURES

LIST OF FIGURES (CONT)

LIST OF FIGURES (CONT)

FIG. 1

ARRANGEMENT FOR HIGH PRESSURE GAS CELL EXPERIMENTS

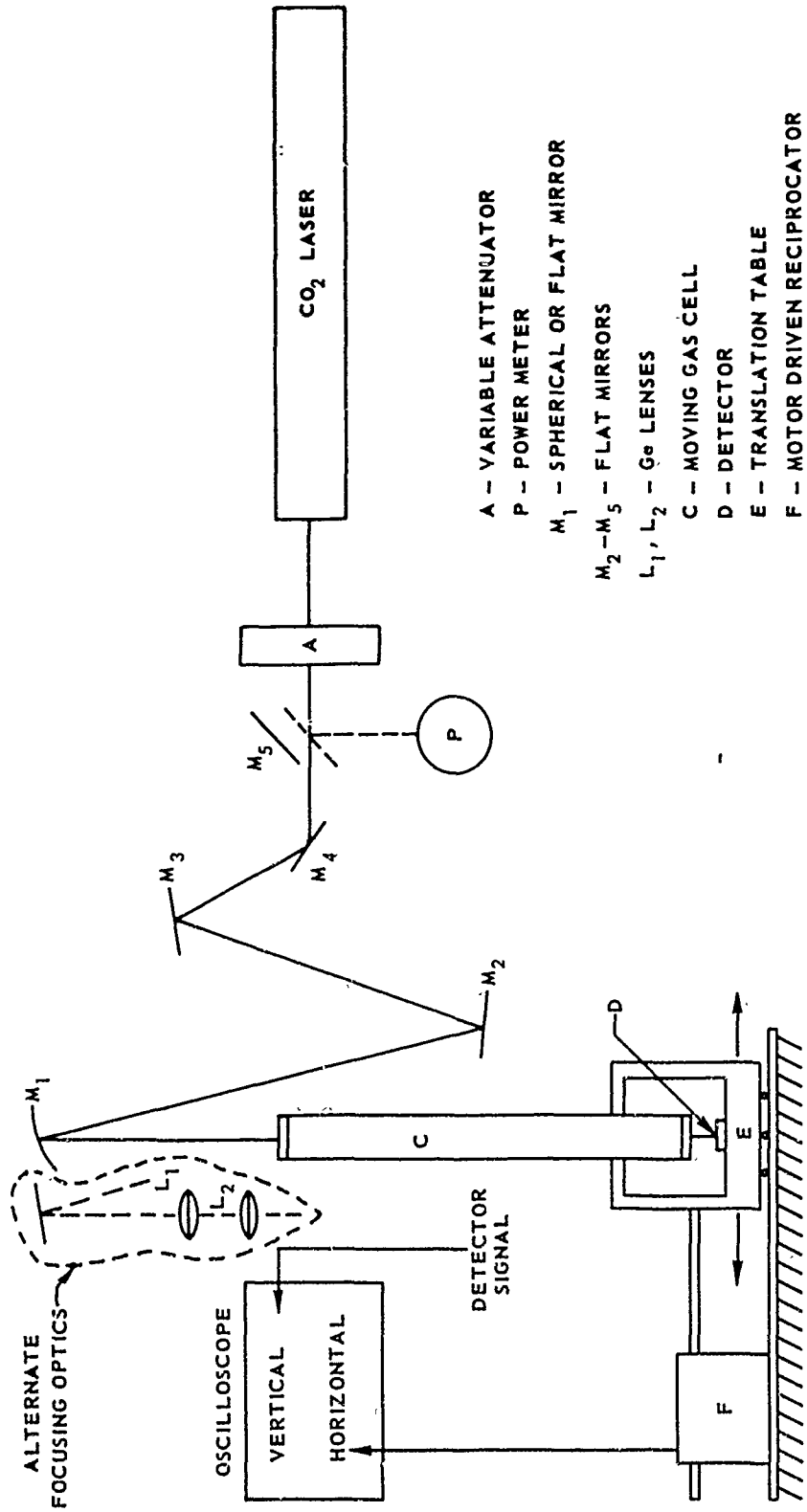

UNDISTORTED COLLIMATED BEAM DATA

7/6/71

INPUT BEAM
P = 1.95W

y = 0
PROFILES

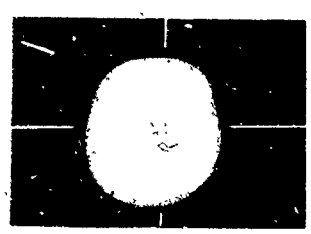

OUTPUT BEAM
P = 1.95W

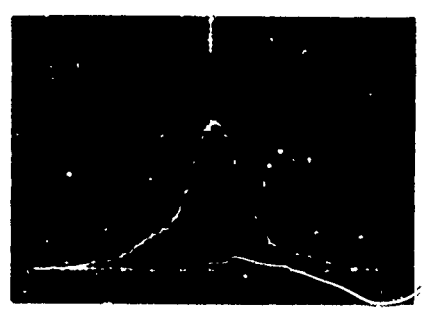

4/2

FIG. 2

FIG. 3

THERMALLY DISTORTED INTENSITY PATTERNS

COLLIMATED BEAM
7/6/71
WIND

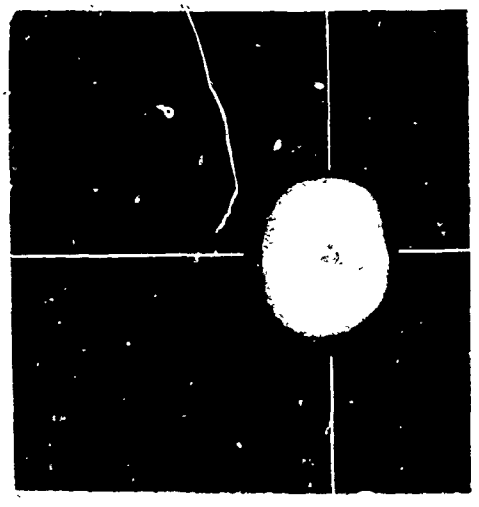

N = 0
P = 1.93W

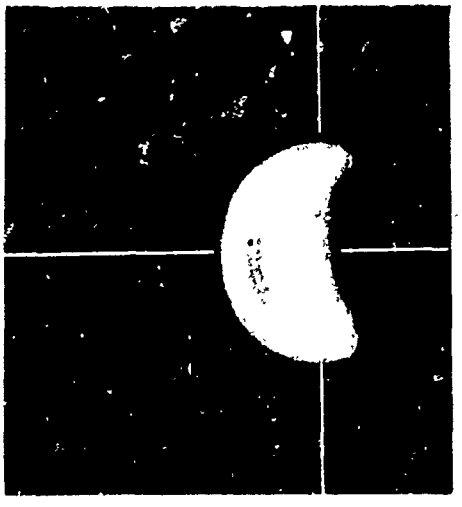

N = 5.4
P = 3.6W
v = 0.5 cm/sec

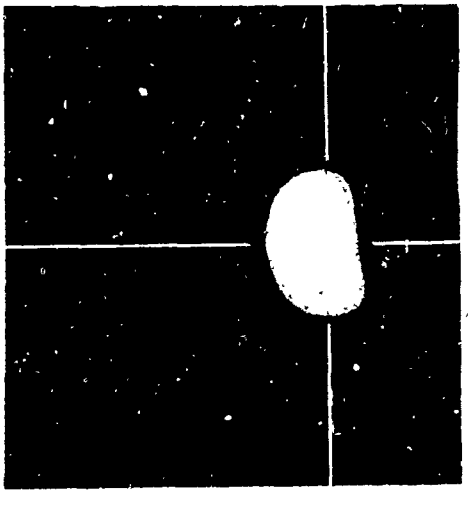

N = 1.35
P = 1.8W
v = 1 cm/sec

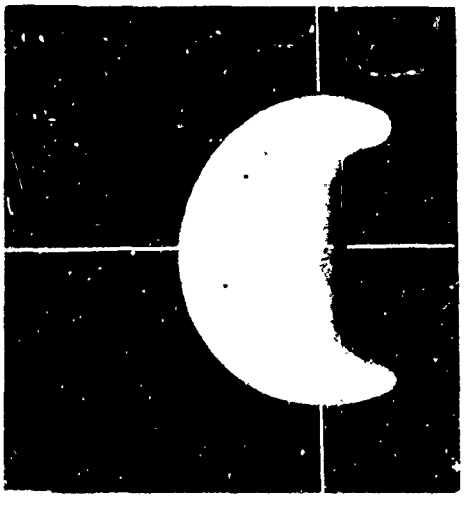

N = 10.8
P = 7.2W
v = 0.5 cm/sec

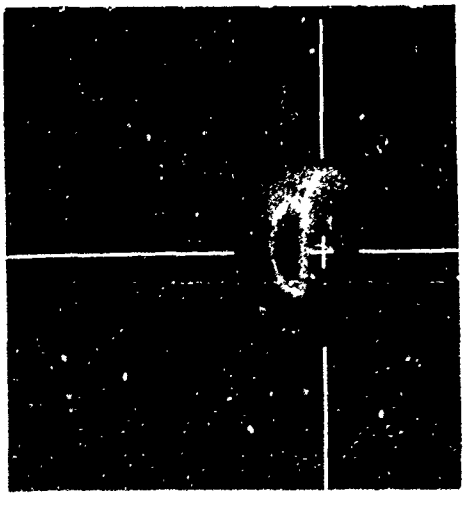

N = 2.7
P = 3.6W
v = 1 cm/sec

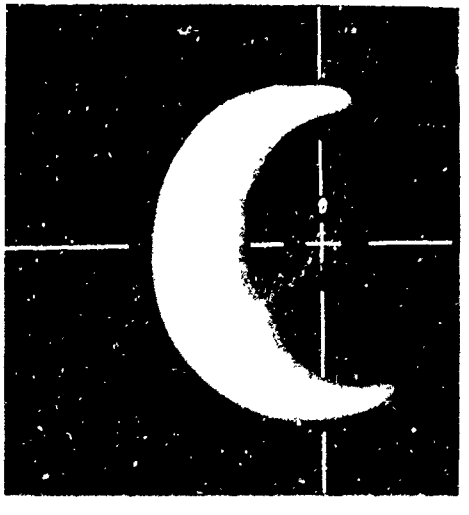

N = 21.6
P = 7.2W
v = 0.25 cm/sec

FIG. 4

THERMALLY DISTORTED INTENSITY PROFILES

COLLIMATED BEAM

HORIZONTAL SCALE = 1.9 mm/div

7/6/71

WIND

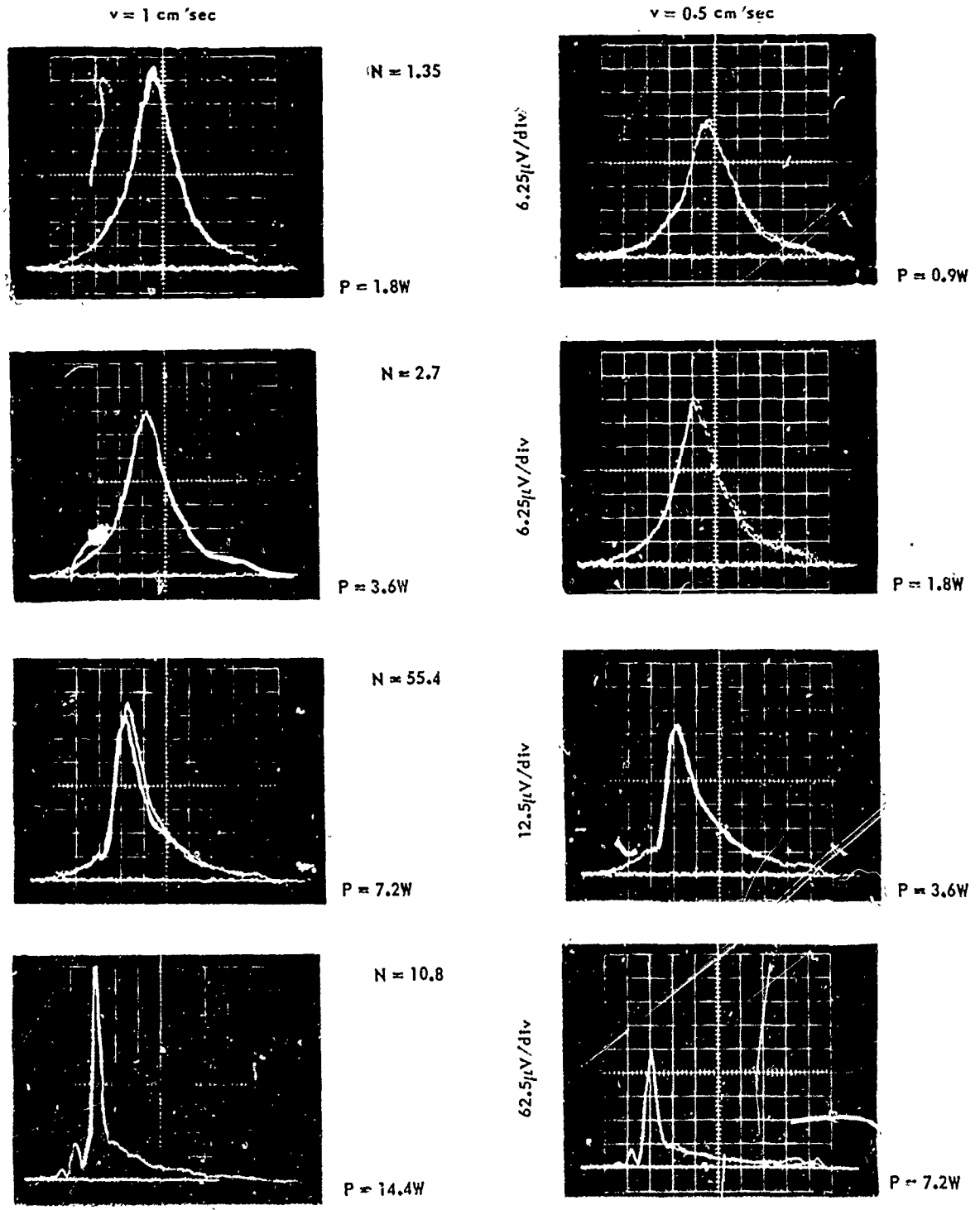

UNDISTORTED FOCUSED BEAM DATA

6/23/71

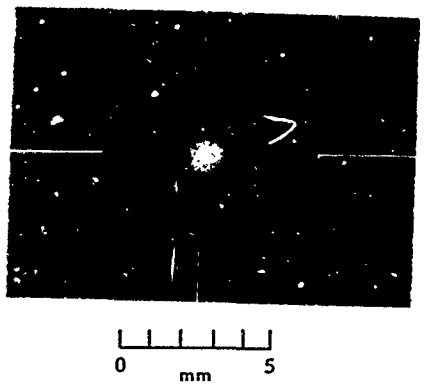

INPUT BEAM
P = 0.4W

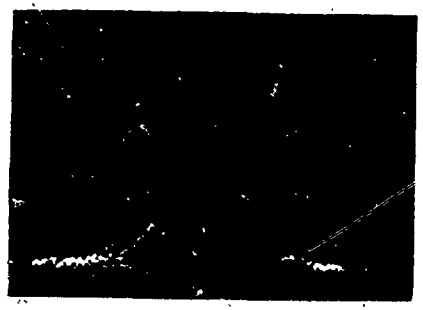

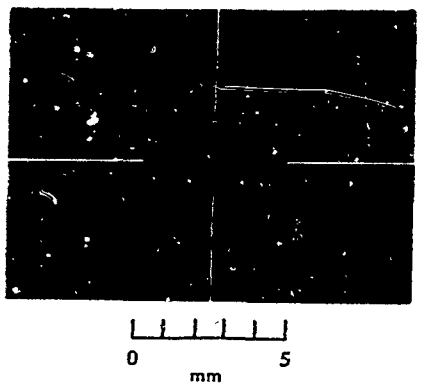

OUTPUT BEAM
P = 0.4W

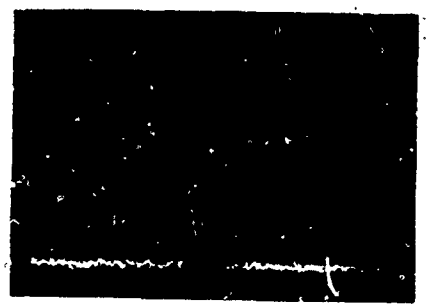

L921004-8

FIG. 5

L921004-8

FIG. 6

THERMALLY DISTORTED INTENSITY PATTERNS

FOCUSED BEAM

6/23/71

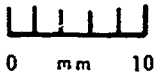

WIND →

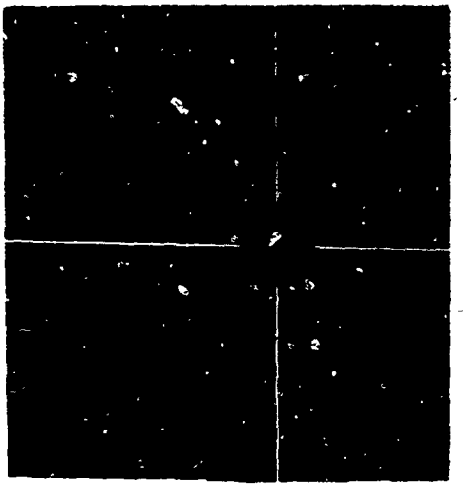

N = 0
P = 0.36W

N = 23
P = 16.2W
v = 1 cm/sec

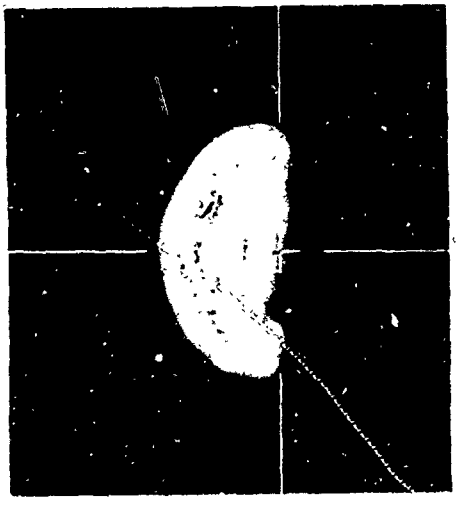

N = 12.7
P = 9W
v = 1 cm/sec

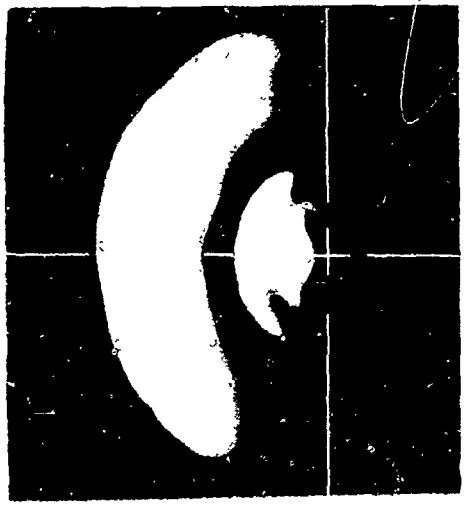

N = 35
P = 12.6 W
v = 0.5 cm/sec

N = 18
P = 12.6 W
v = 1 cm/sec

N = 45
P = 16.2W
v = 0.5 cm/sec

FIG. 7

THERMALLY DISTORTED INTENSITY PROFILES
FOCUSED BEAM - I

6/23/71

HORIZONTAL SCALE = 1.9 mm/div

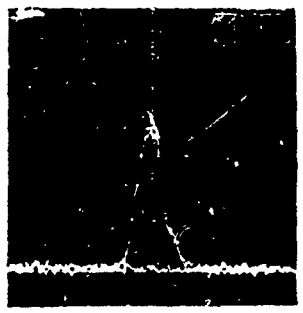

N = 0
P ~ 0.36W

UNDISTORTED

WIND →

v = 1cm/sec

v = 0.5 cm/sec

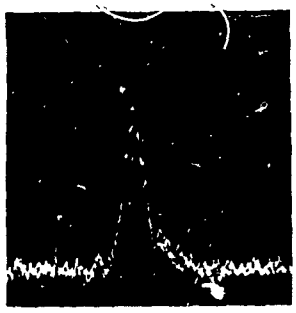

N ~ 1

P = 0.9W

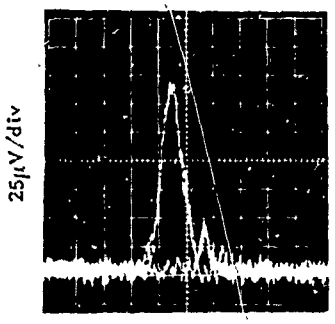

P = 0.4W

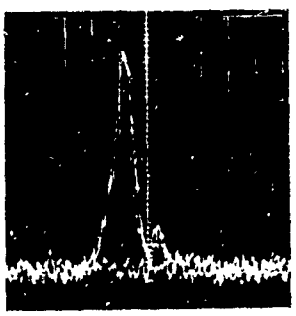

N ~ 3

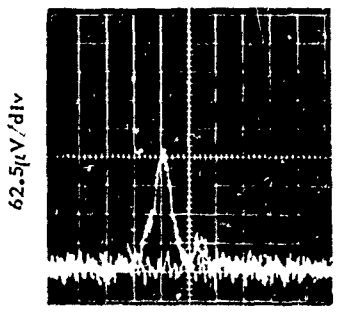

P = 0.9W

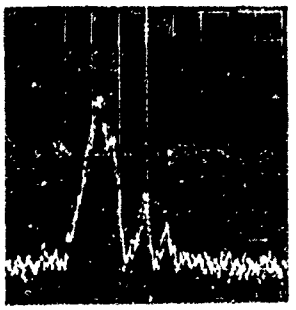

N ~ 5

P = 3.6W

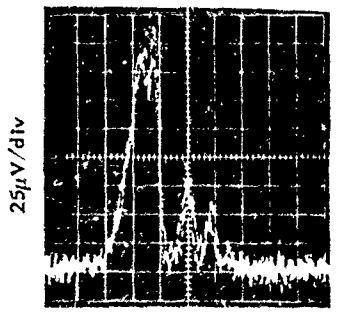

P = 1.8W

FIG. 8

THERMALLY DISTORTED INTENSITY PROFILES
FOCUSED BEAM – II

6/23/71

HORIZONTAL SCALE = 1.9 mm/div

WIND →

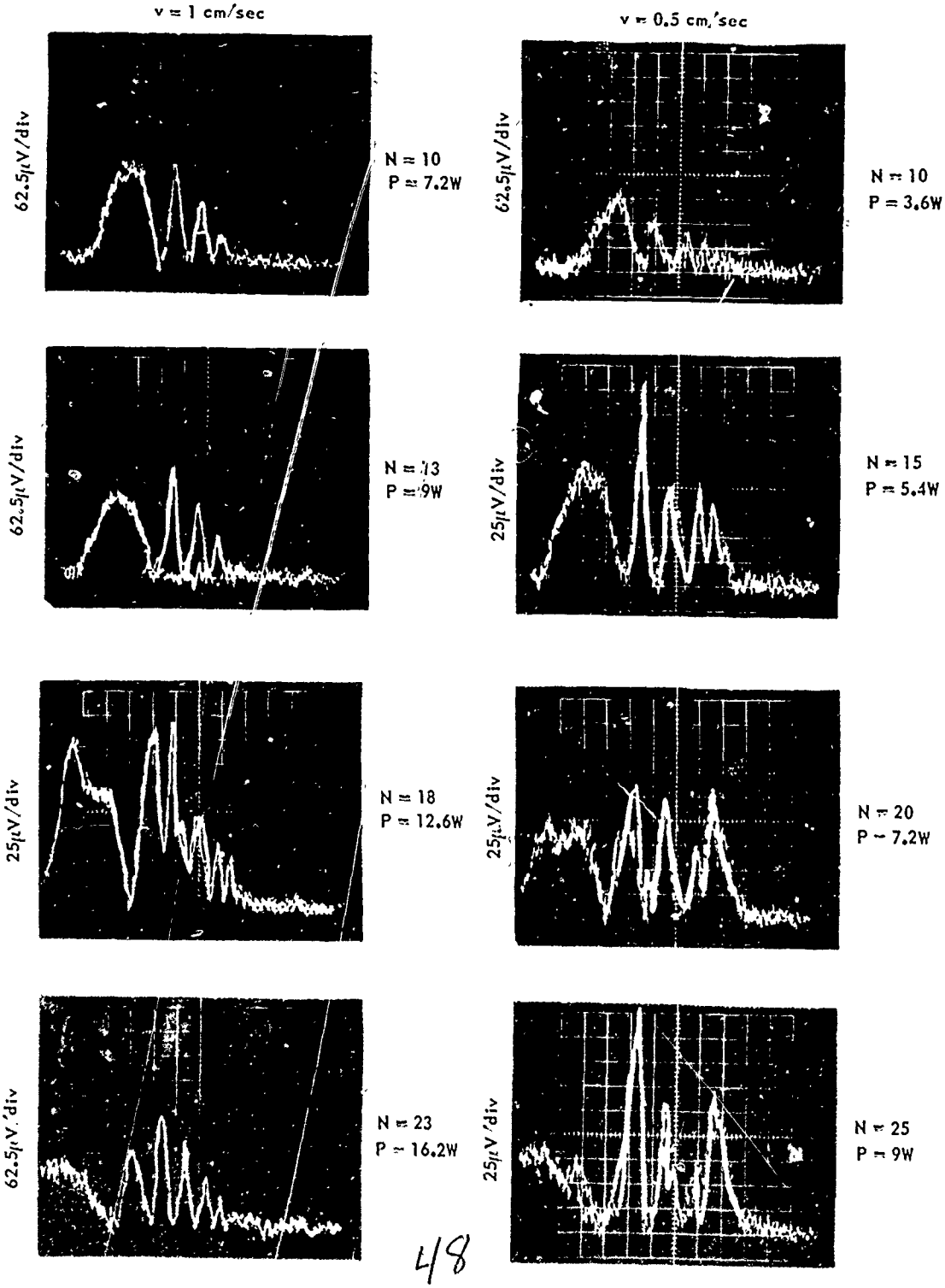

FIG. 9

NATURAL CONVECTION EFFECTS

VERTICAL PATH
COLLIMATED BEAM
7 6 71
v = 0.5 cm sec
WIND →

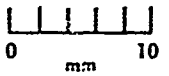

HORIZONTAL SCALE = 1.9 m m div

N = 11
P = 7.2W

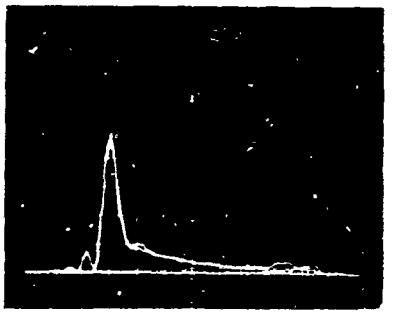

N = 17
P = 11.2W

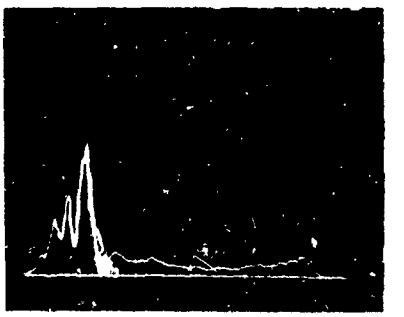

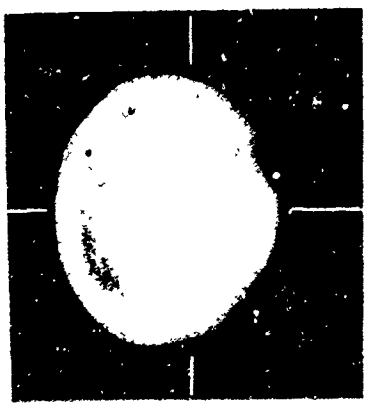

N = 22
P = 14.4W

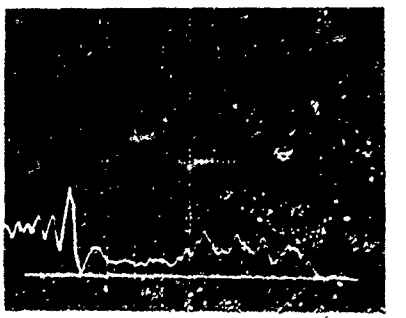

FIG. 10

NORMALIZED PEAK INTENSITY DEPENDENCE ON N

HIGH PRESSURE GAS CELL

	BEAM	DATE	a_i/a_o	a_1, mm
○	FOCUSED	6/23/71	2.6	3.1
●	FOCUSED	8/8,17,20	7.4	3.4
△	COLLIMATED	7/6/71	0.9	2.4

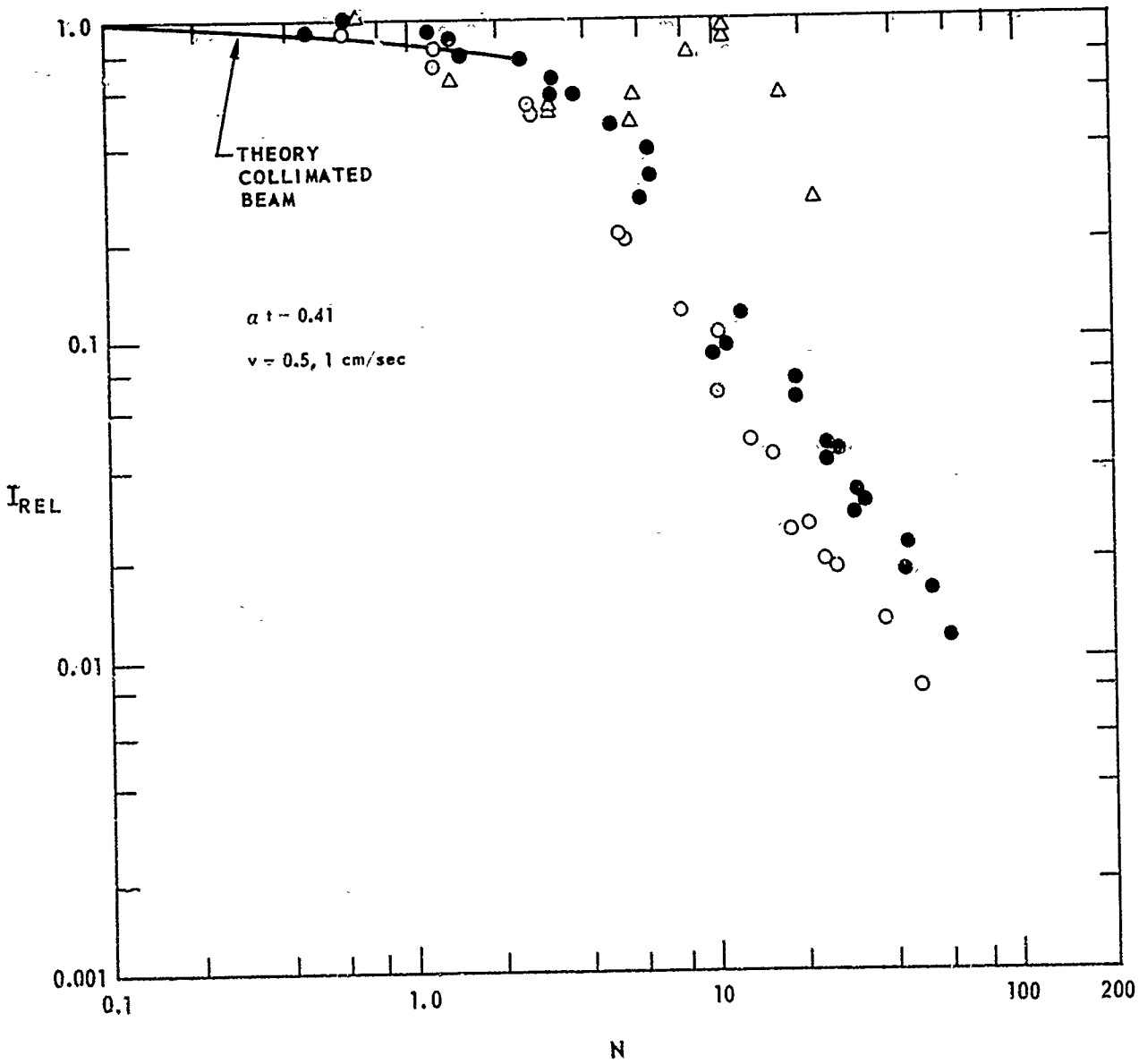

NORMALIZED BEAM DEFLECTION DEPENDENCE ON N

HIGH PRESSURE GAS CELL

BEAM	DATE	a_i/a_o	a_i, mm
○ FOCUSED	6/23/71	2.6	3.1
● FOCUSED	8/8,17,26	7.4	3.4
△ COLLIMATED	7/6/71	0.9	2.4

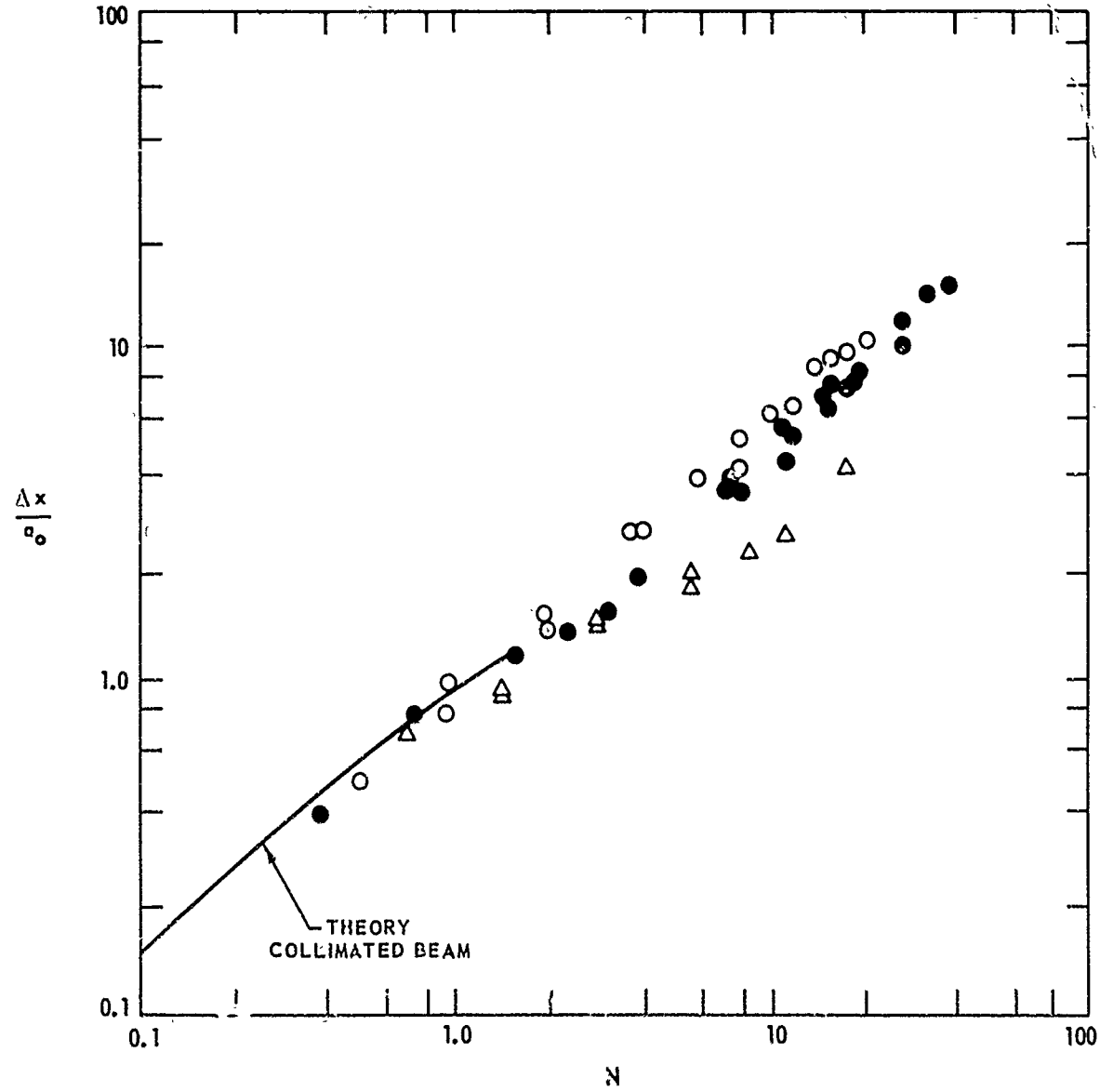

FIG. 12

PEAK INTENSITY DEPENDENCE ON POWER

HIGH PRESSURE GAS CELL

$\alpha t = 0.41$

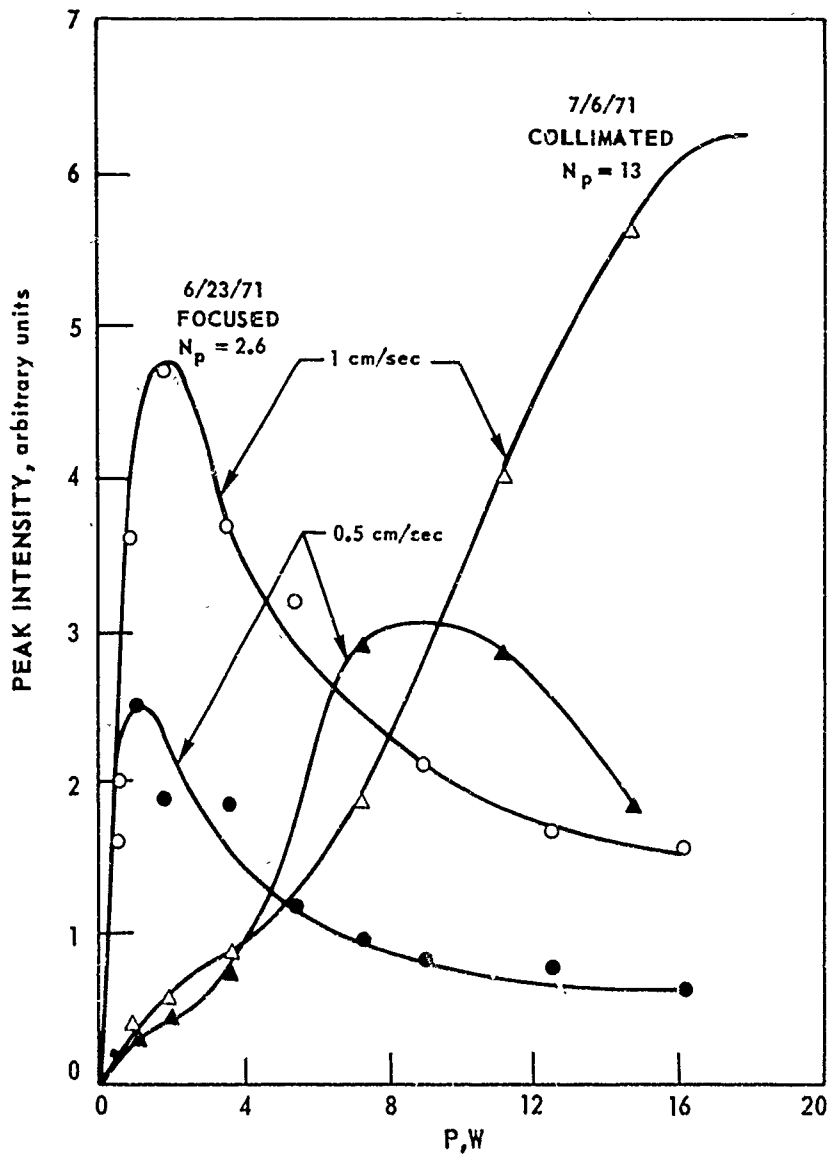

FIG. 13

NORMALIZED PEAK INTENSITY DEPENDENCE ON N

CO_2 BEAM IN MOVING CS_2 CELL

$\alpha t = 2.2$; $t = 12.7$ cm $v = 1.5$ cm/sec

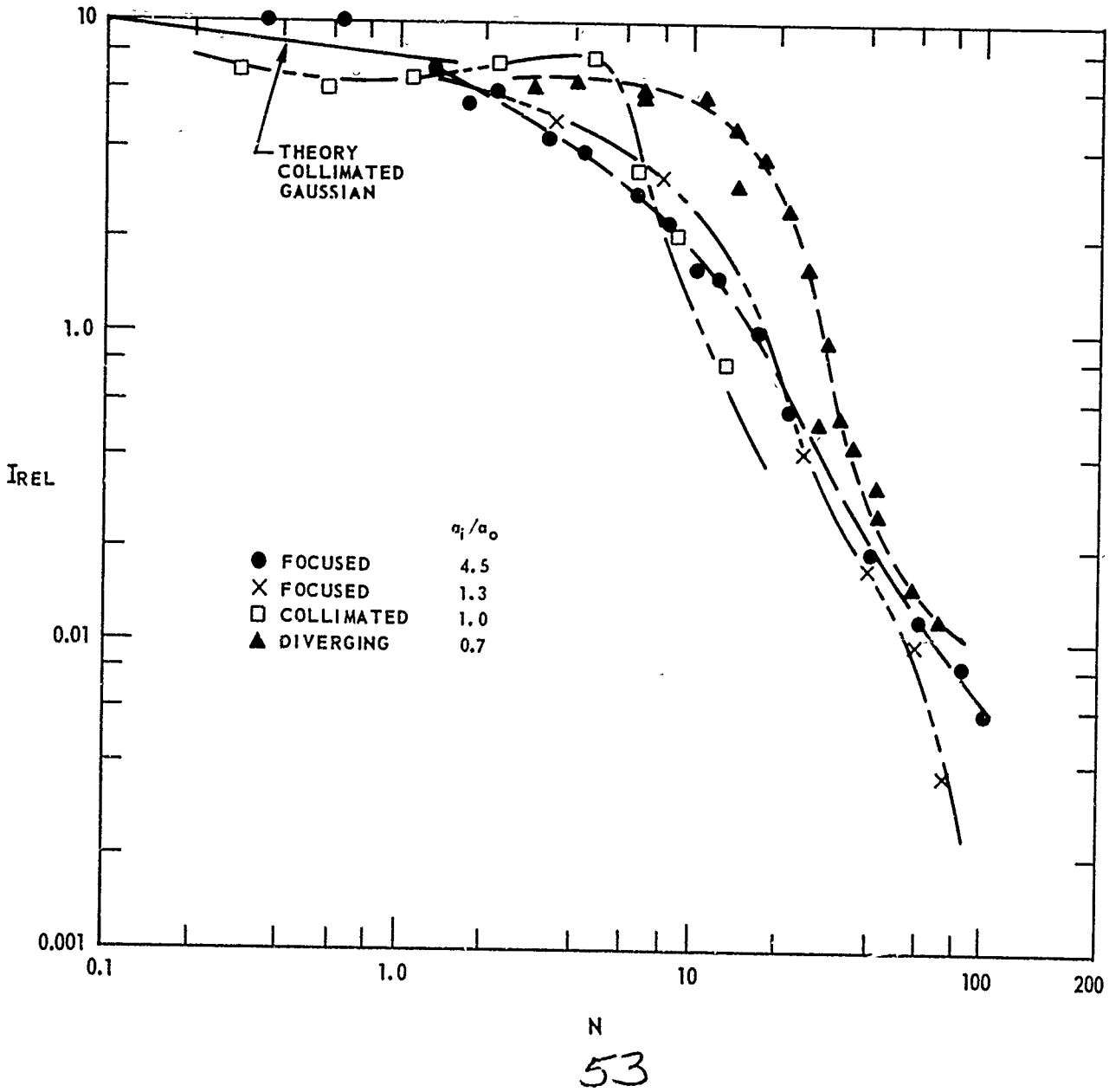

FIG. 14

NORMALIZED BEAM DEFLECTION DEPENDENCE ON N

CO_2 BEAM IN MOVING CS_2 CELL

$\alpha^2 = 2.2$ $t = 12.7$ cm $v = 1.5$ cm/sec

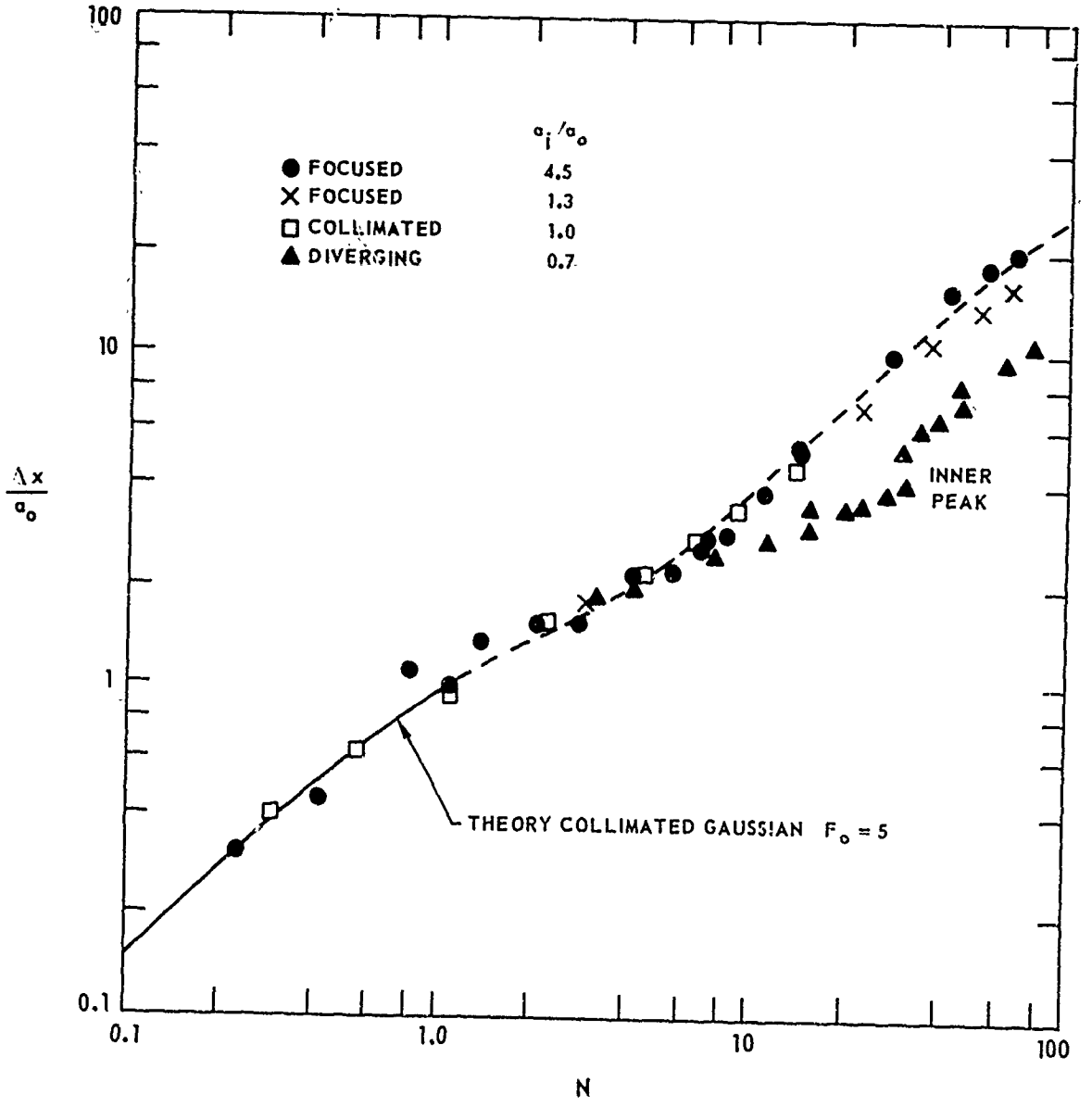

FIG. 15

PEAK INTENSITY DEPENDENCE ON POWER

CO_2 BEAM IN MOVING CS_2 CELL

$\alpha t = 2.2$

$v = 1$ cm/sec

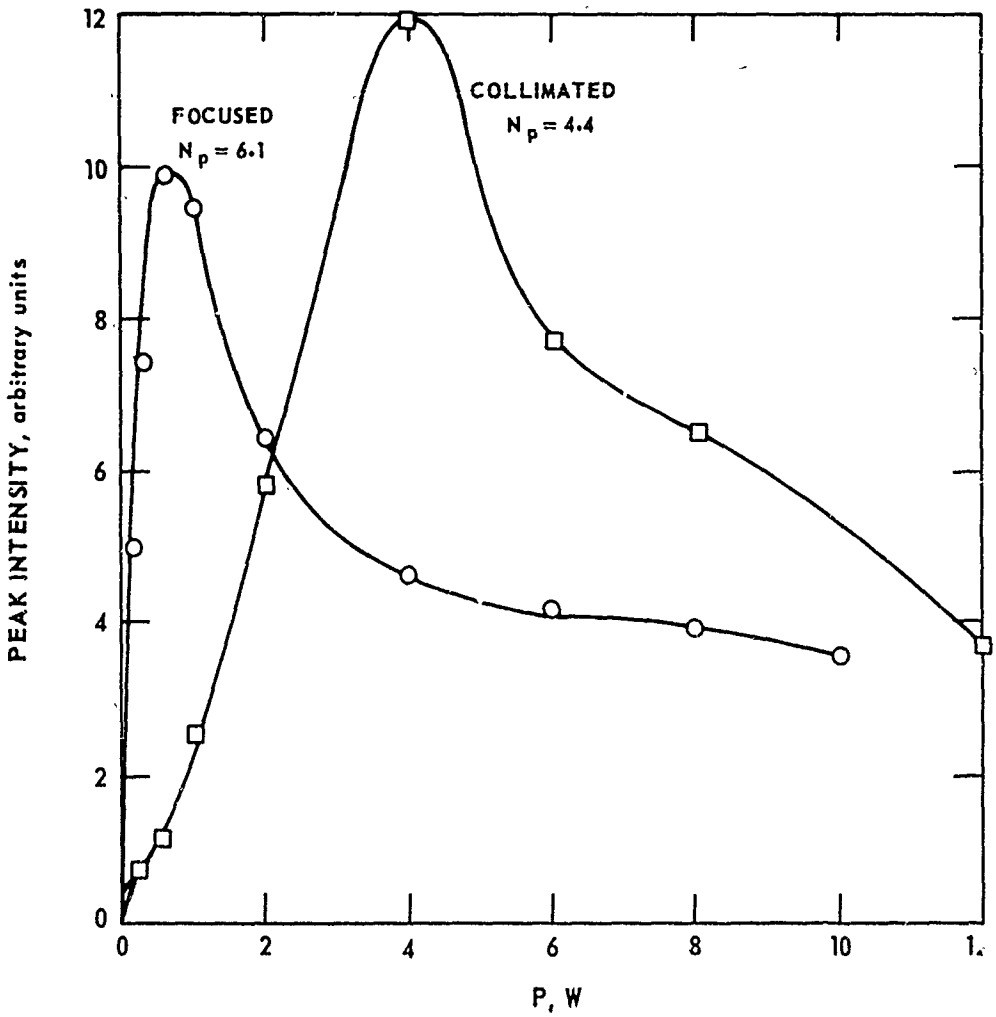

FIG. 16

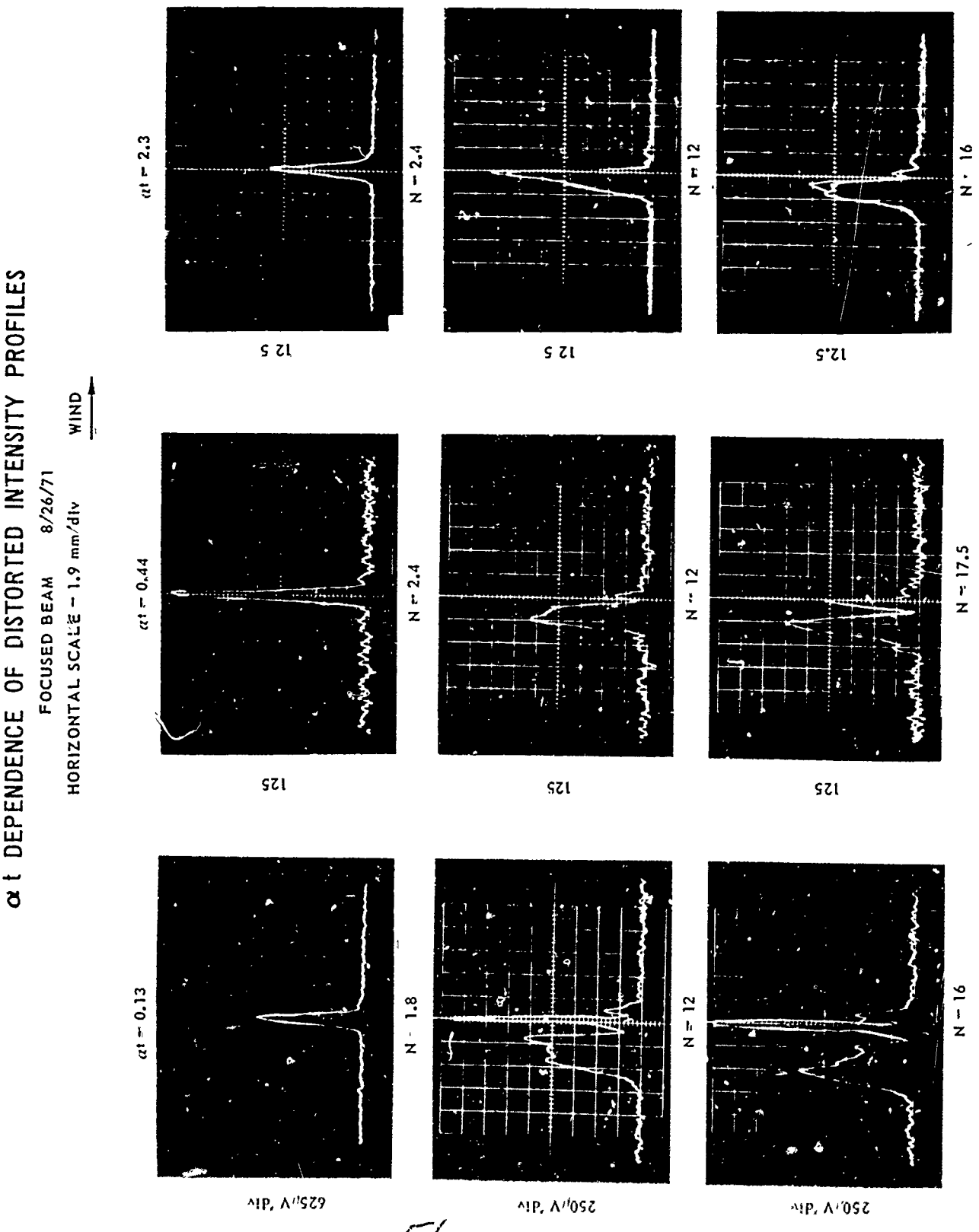
αt DEPENDENCE OF DISTORTED INTENSITY PROFILES
FOCUSED BEAM 8/26/71
HORIZONTAL SCALE = 1.9 mm/div
WIND
αt = 2.3
N = 2.4
N = 12
N = 16
αt = 0.44
N = 2.4
N = 12
N = 17.5
αt = 0.13
N = 1.8
N = 12
N = 16
12.5
250 V/div
625 V/div

FIG. 17

INFLUENCE OF αt ON THE NORMALIZED PEAK INTENSITY DEPENDENCE ON N

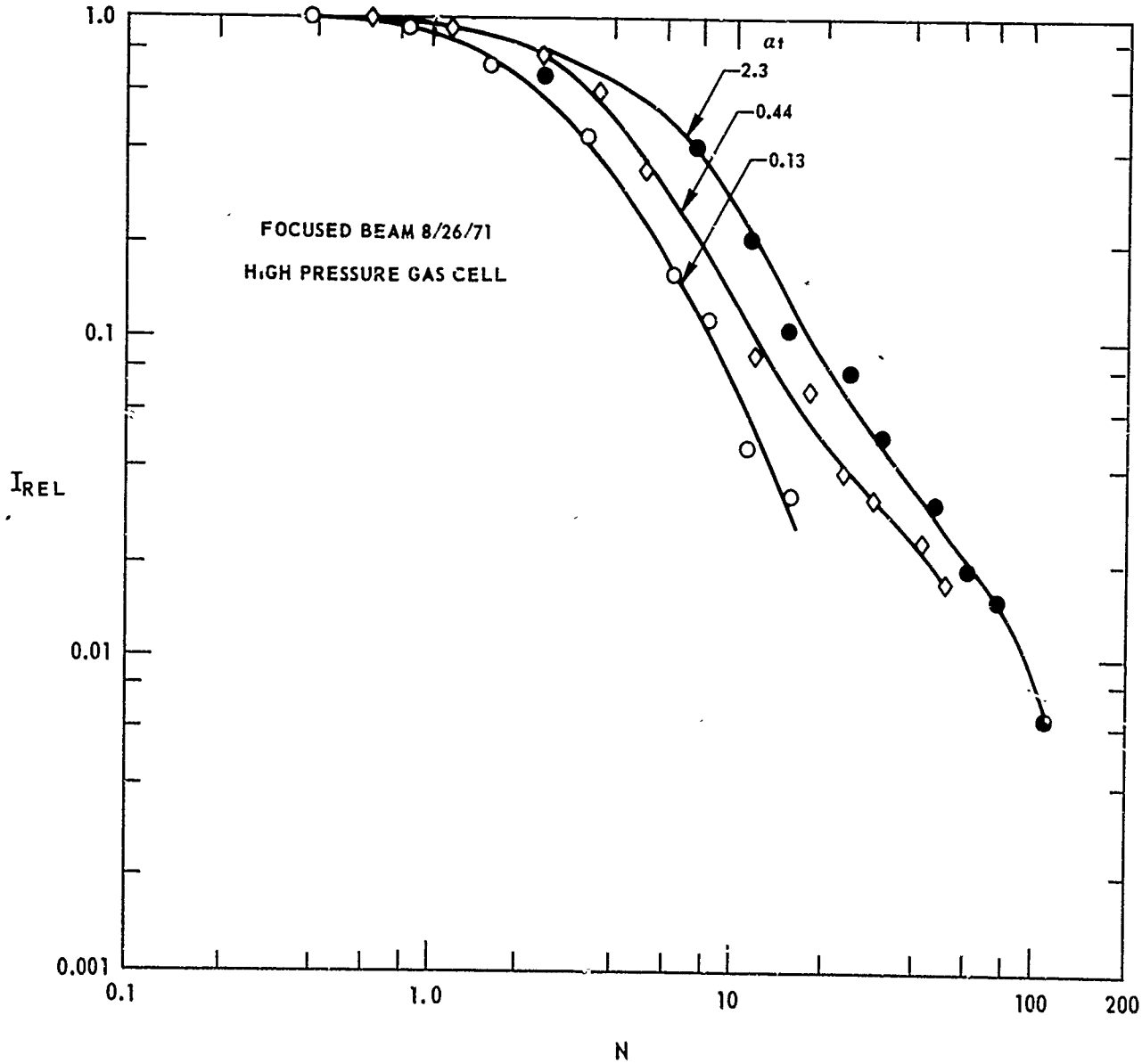

INFLUENCE OF αt ON THE NORMALIZED BEAM DEFLECTION DEPENDENCE ON N

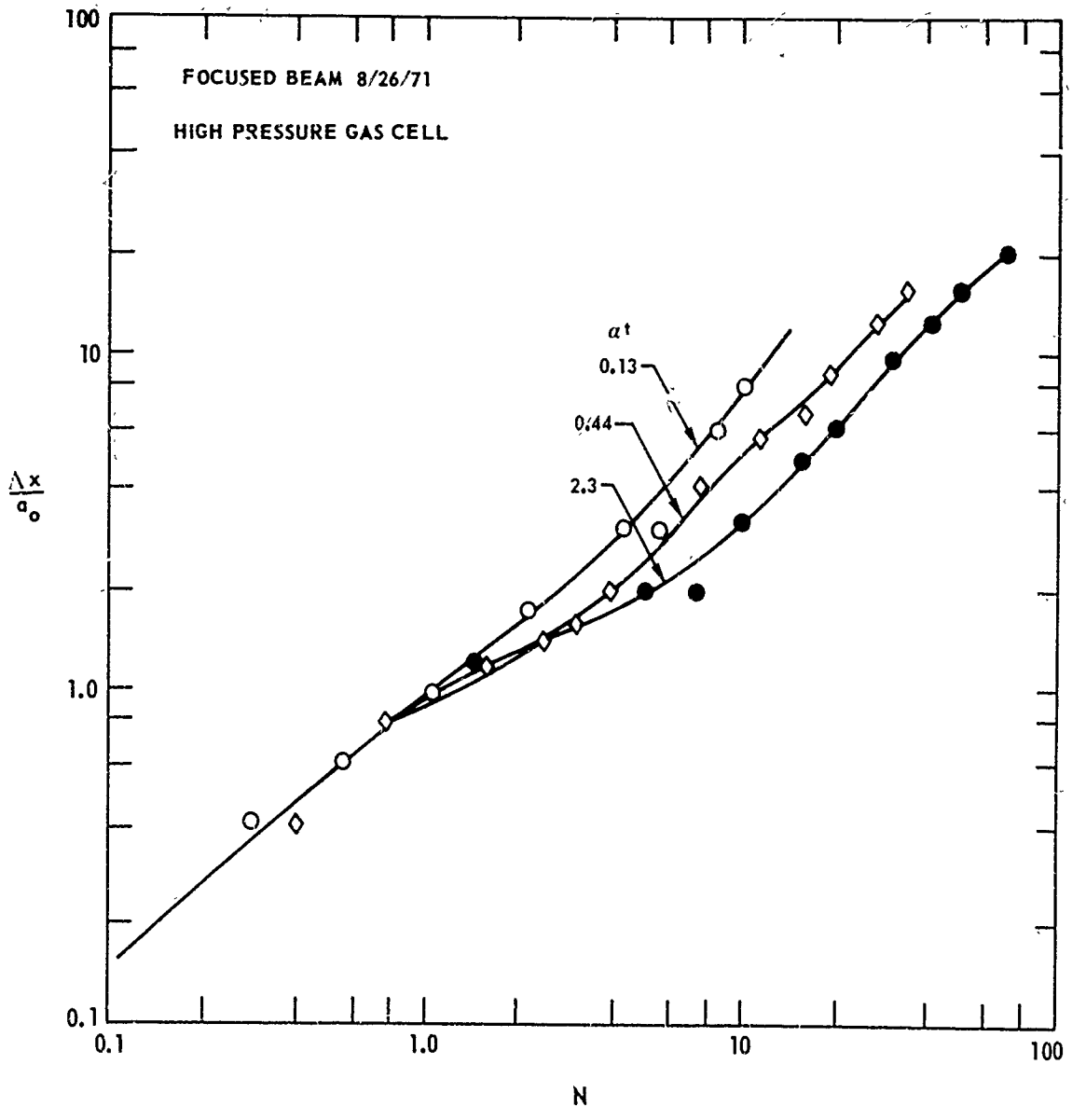

EFFECT OF FOCAL RANGE VARIATION ON THERMAL DISTORTION

HIGH PRESSURE GAS CELL

(8/8,9/71)

P = 8.4W; v = 1cm/sec

F = CELL INPUT–TO–FOCUSED SPOT PATH LENGTH

Z = CELL INPUT–TO–DETECTOR PATH LENGTH (114 cm)

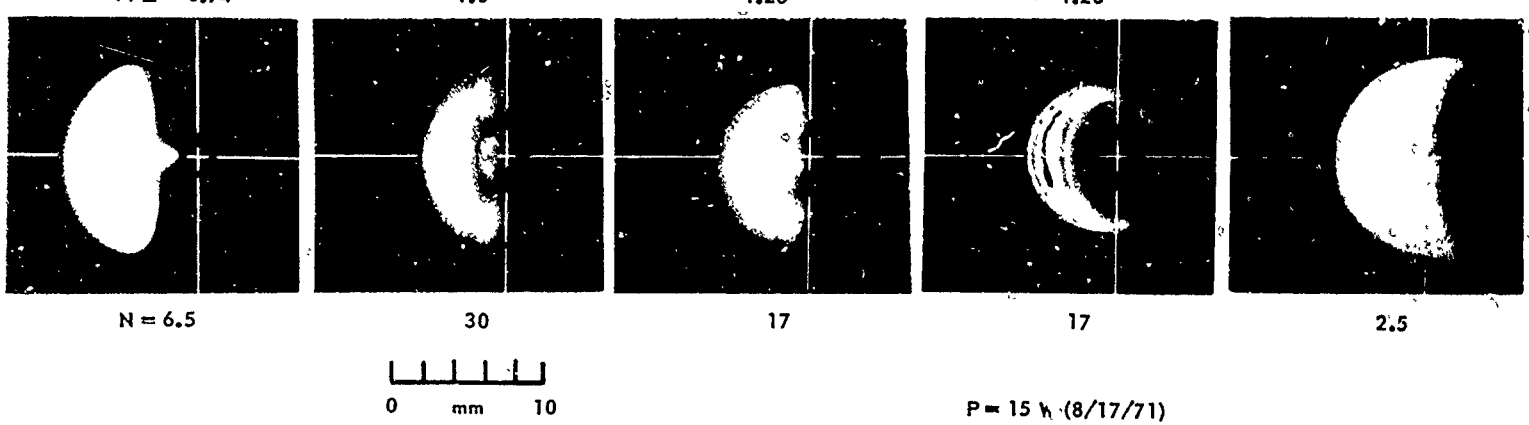

P = 15 W (8/17/71)

FIG. 19

EFFECT OF FOCAL RANGE VARIATION ON INTENSITY PROFILES – I

8 17 '71

HORIZONTAL SCALE = 1.9 m m div

NO ABSORPTION

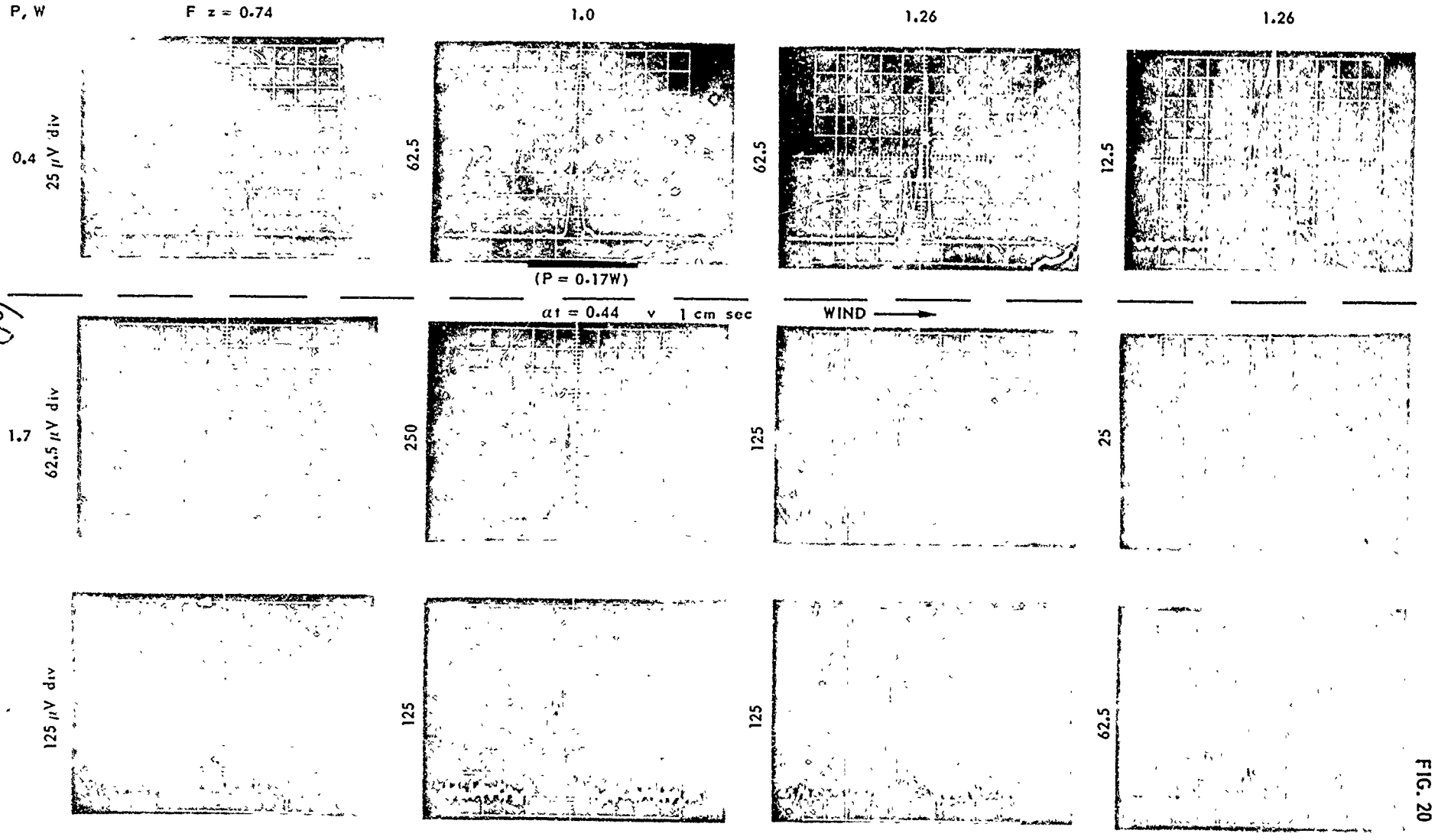

L921004-8

FIG. 20

EFFECT OF FOCAL RANGE VARIATION ON INTENSITY PROFILES – II

8 17 71

HORIZONTAL SCALE - 1.9 mm/div WIND ⟶

$\sigma_1 = 0.44$ v = 1 cm sec

L921004-8

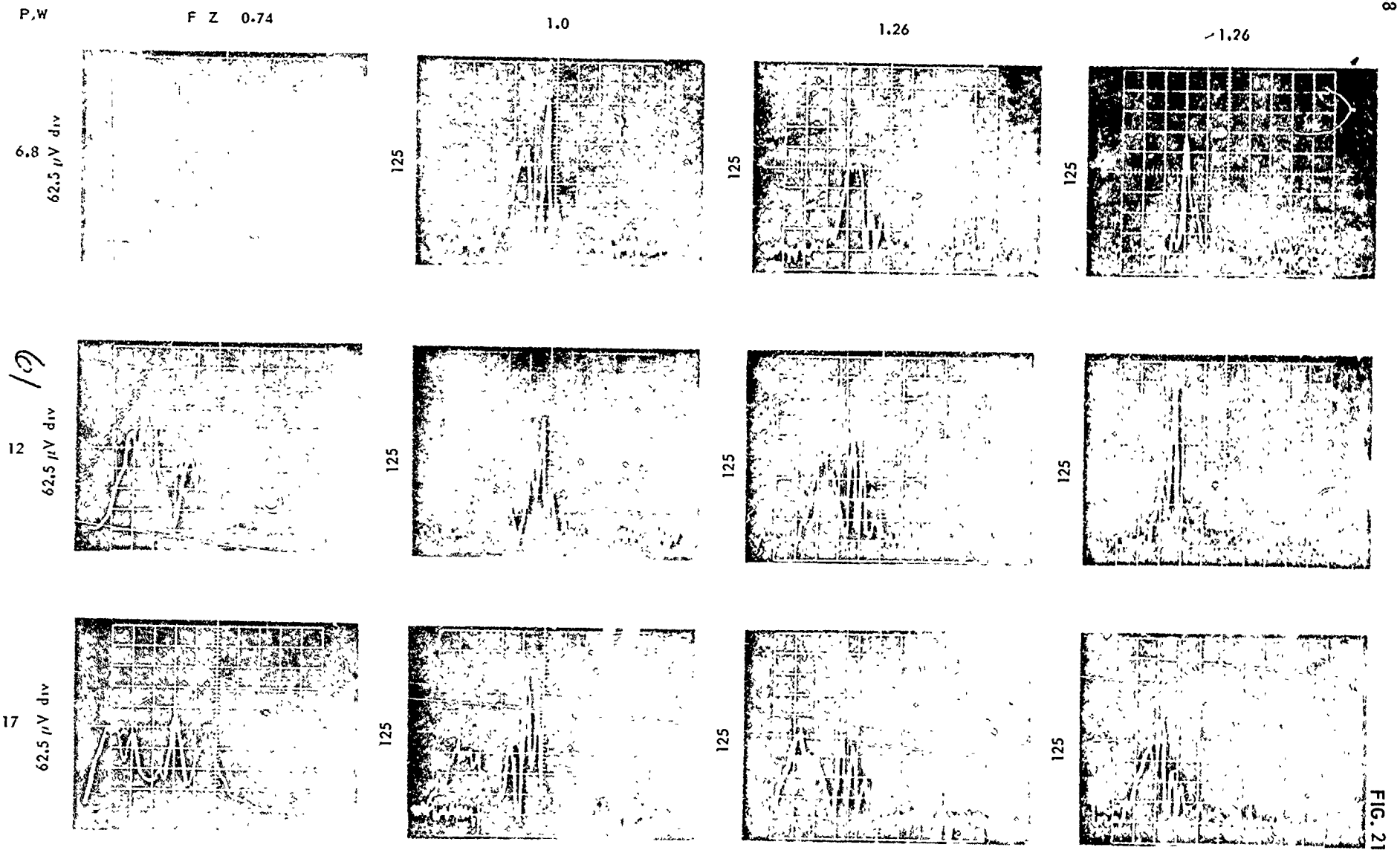

FIG. 21

FIG. 22

PEAK INTENSITY DEPENDENCE ON POWER
HIGH PRESSURE GAS CELL

$\alpha t = 0.44$
$v = 1$ cm/sec

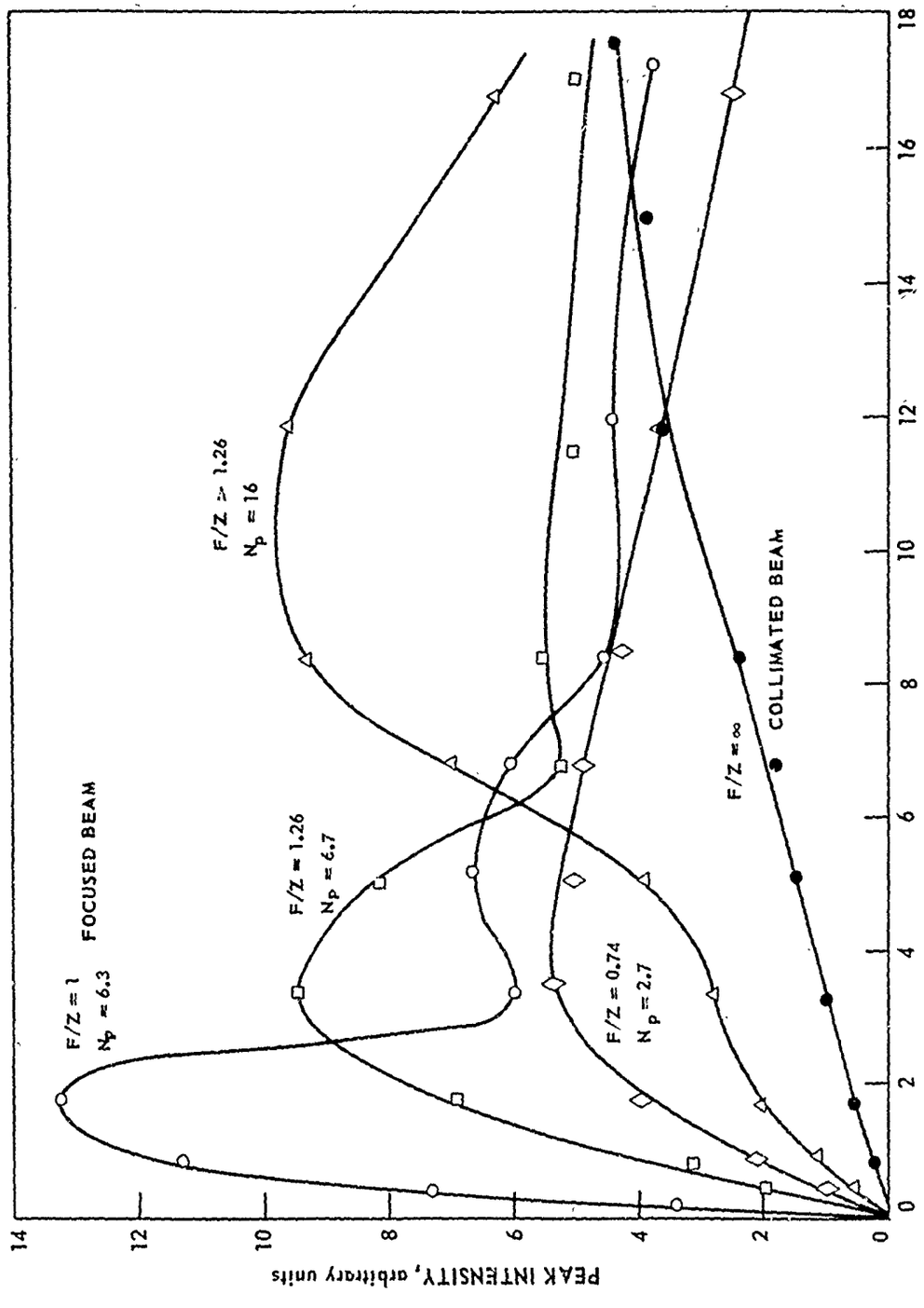

62

FIG. 23

COMPARISON OF BEAM DISTORTION WITH AND WITHOUT KINETIC COOLING

COLLIMATED GAUSSIAN BEAM

INTENSITY CONTOURS – 40 PERCENT OF PEAK

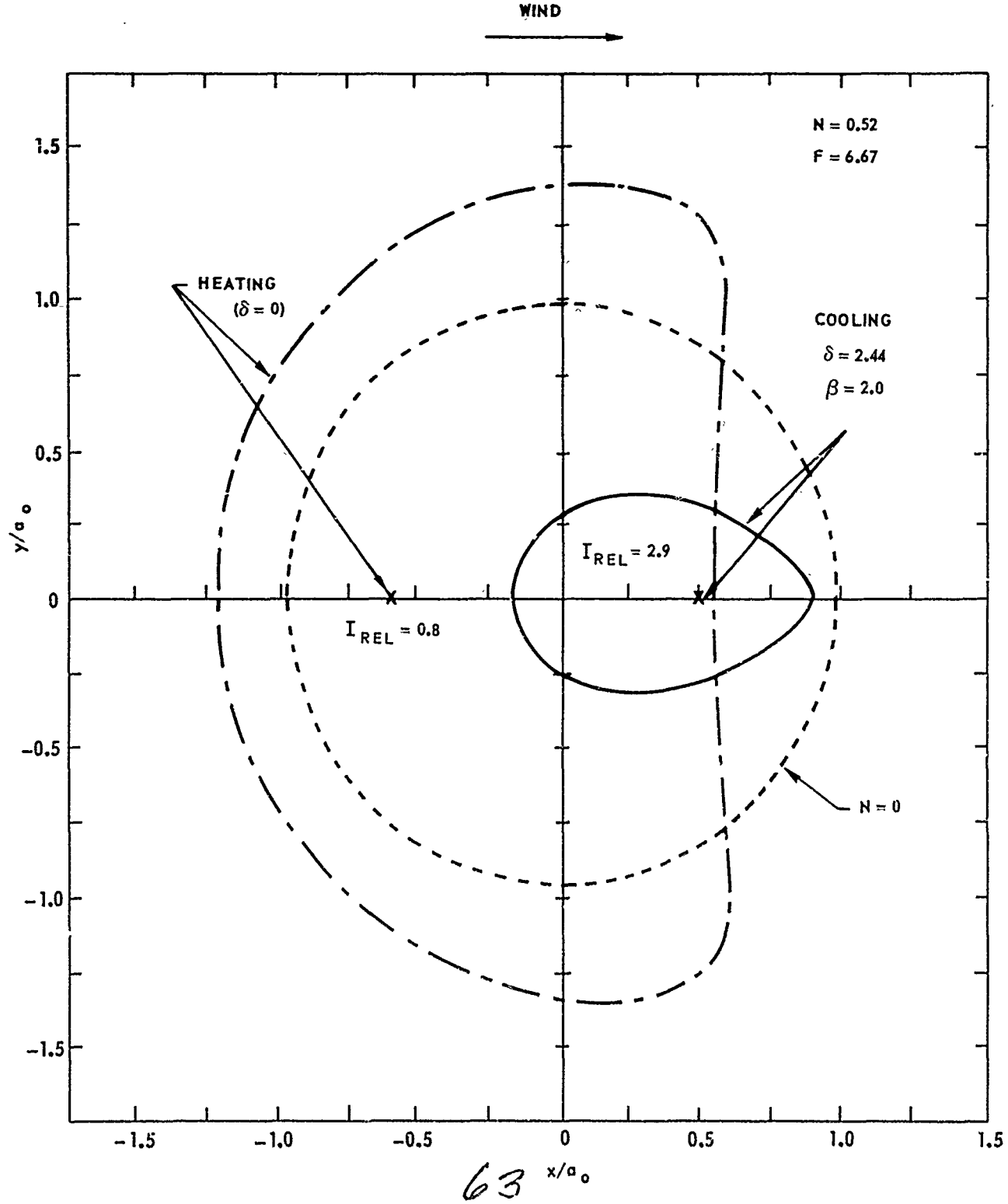

FIG. 24

RELATIVE PEAK AND AVERAGE INTENSITY VS N

COLLIMATED GAUSSIAN BEAM

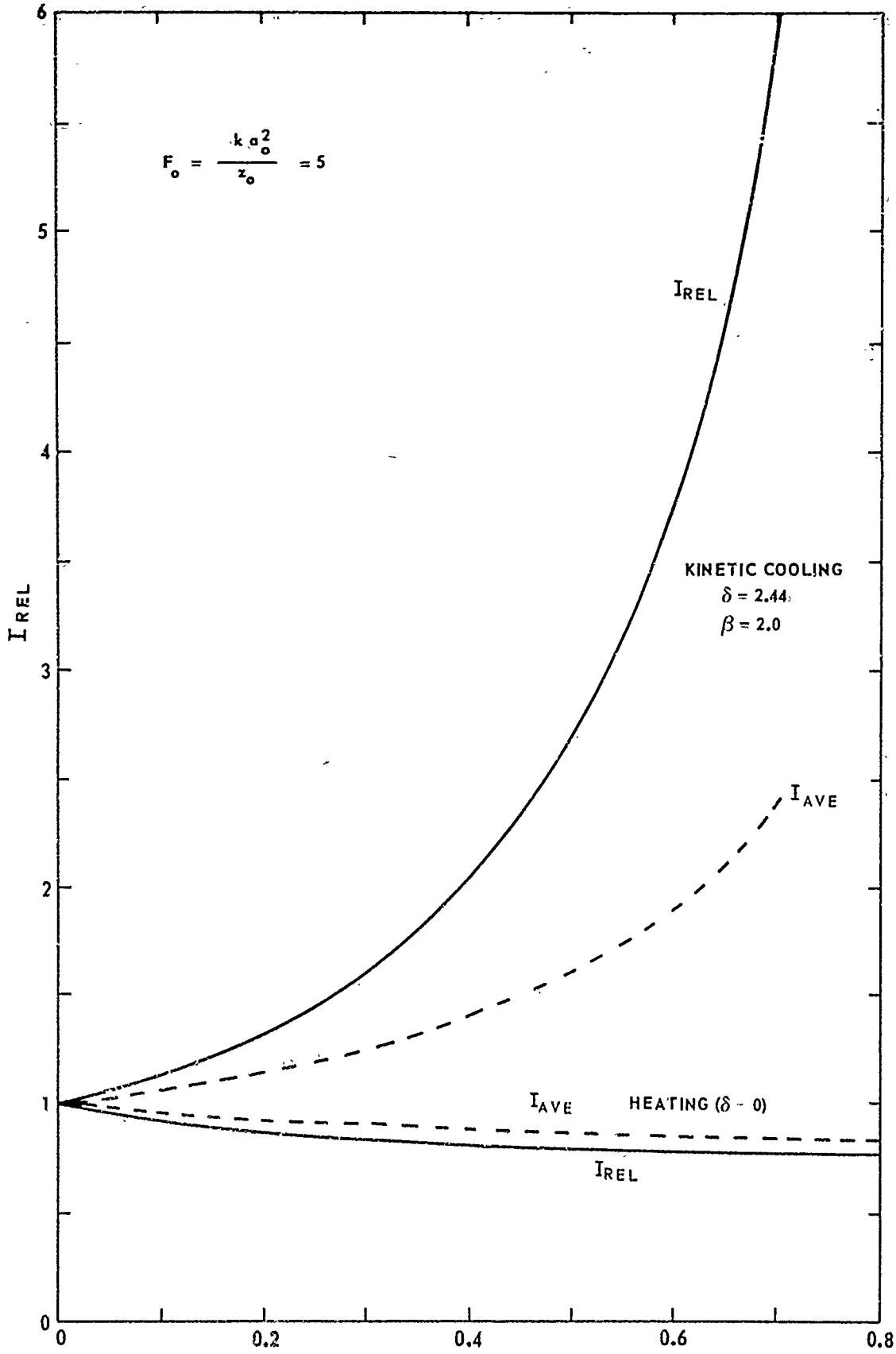

FIG. 25

NORMALIZED PEAK INTENSITY SHIFT VS N

COLLIMATED GAUSSIAN BEAM

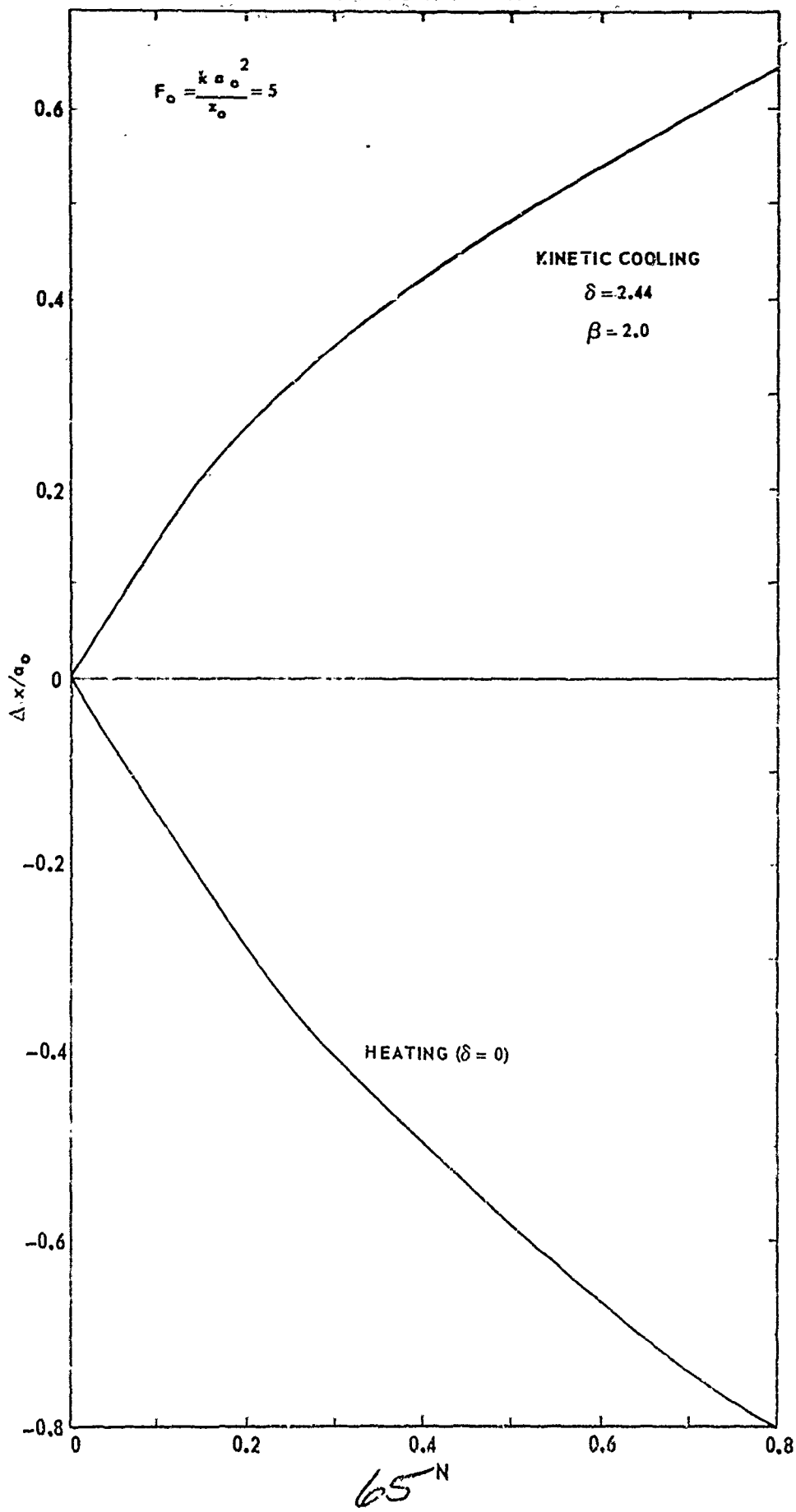

65

FIG. 26

DEPENDENCE OF TEMPERATURE PROFILE COEFFICIENTS ON γ

(FROM ALESHKEYICH & SUKHORUKOV, JETP LETTERS, 12, 77 (1970))

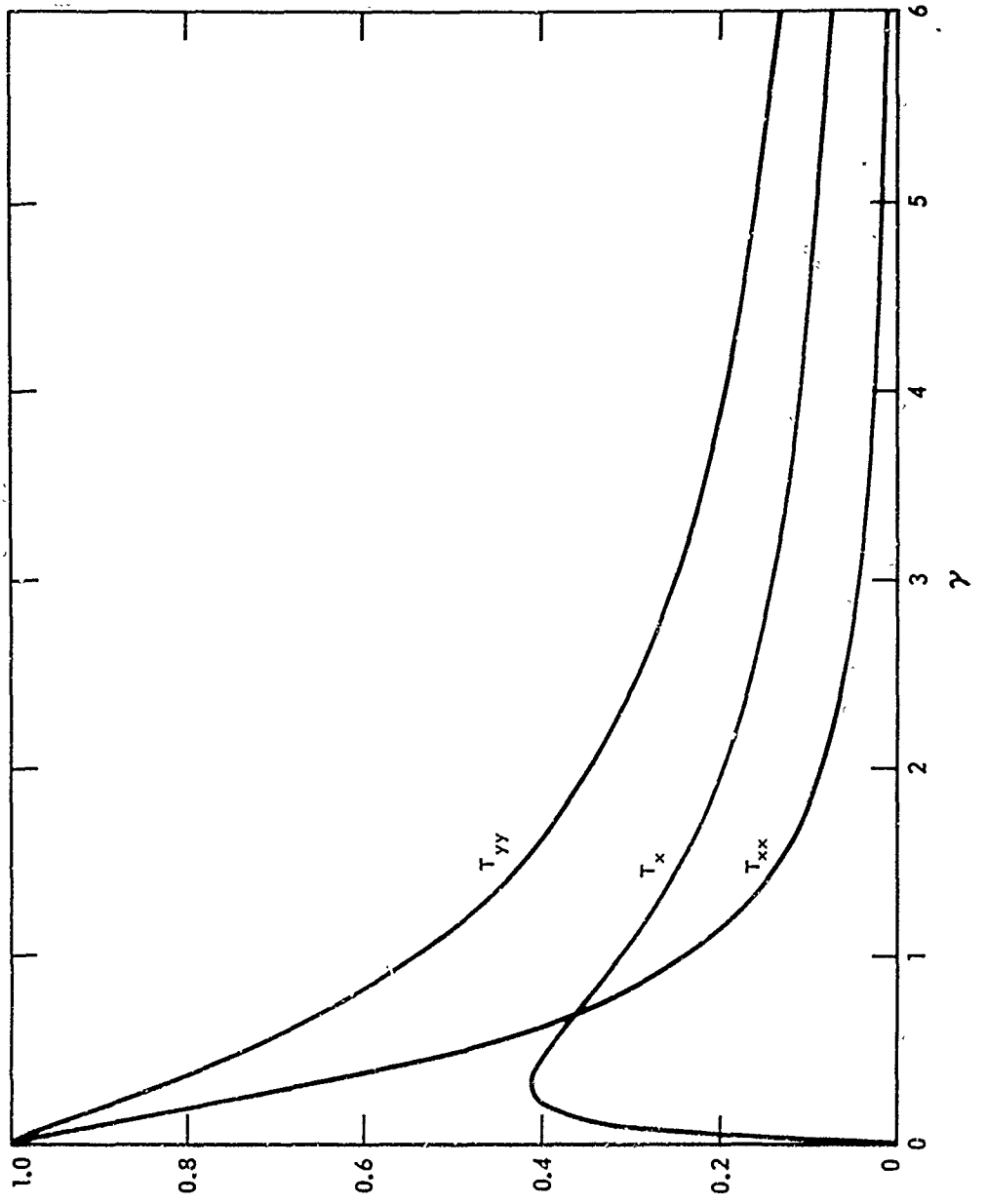

FIG. 27

TURBULENCE EFFECT ON THERMALLY DISTORTED INTENSITY

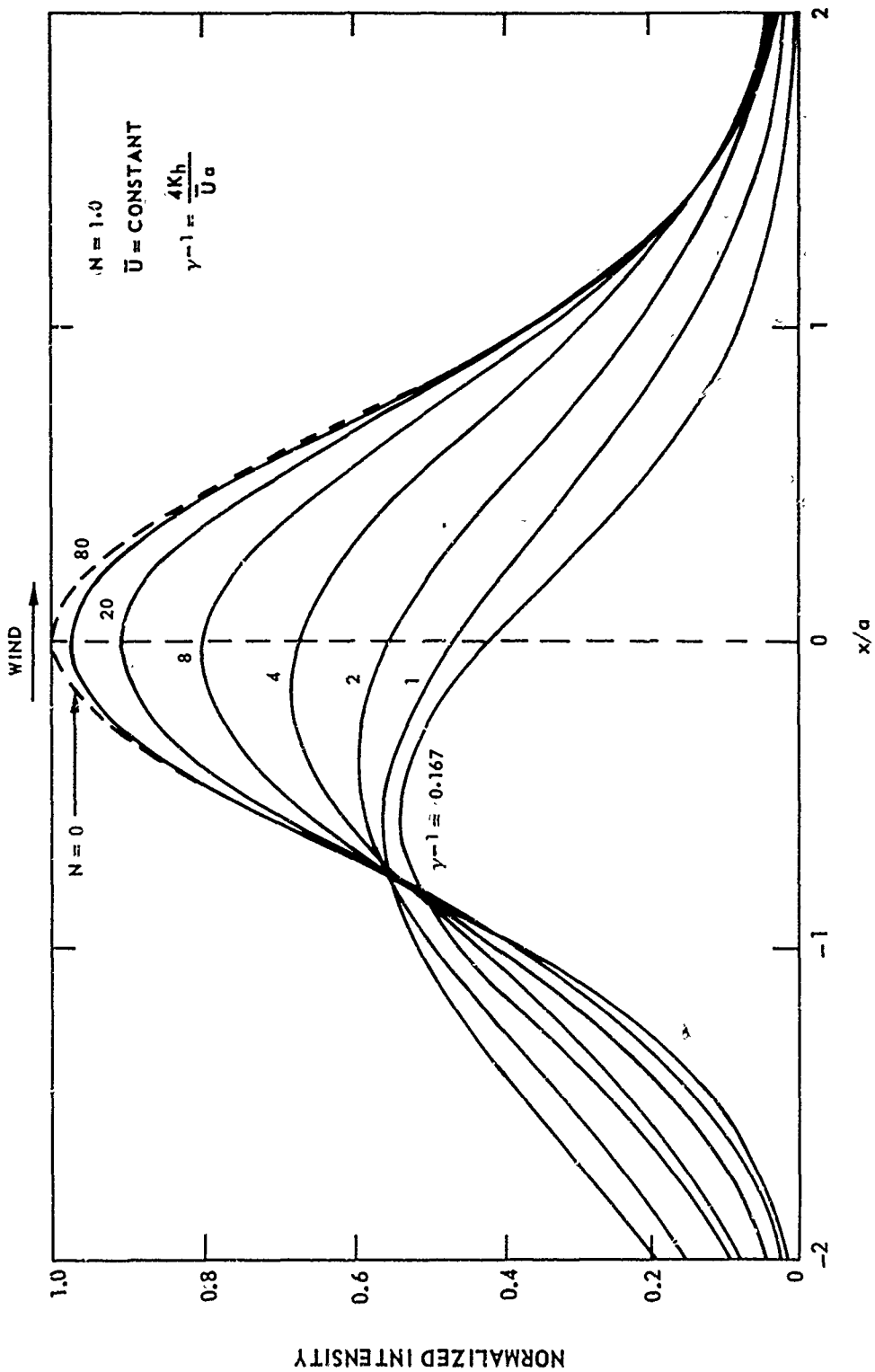

CALCULATED ON-AXIS INTENSITY DEPENDENCE ON TURBULENT DIFFUSION

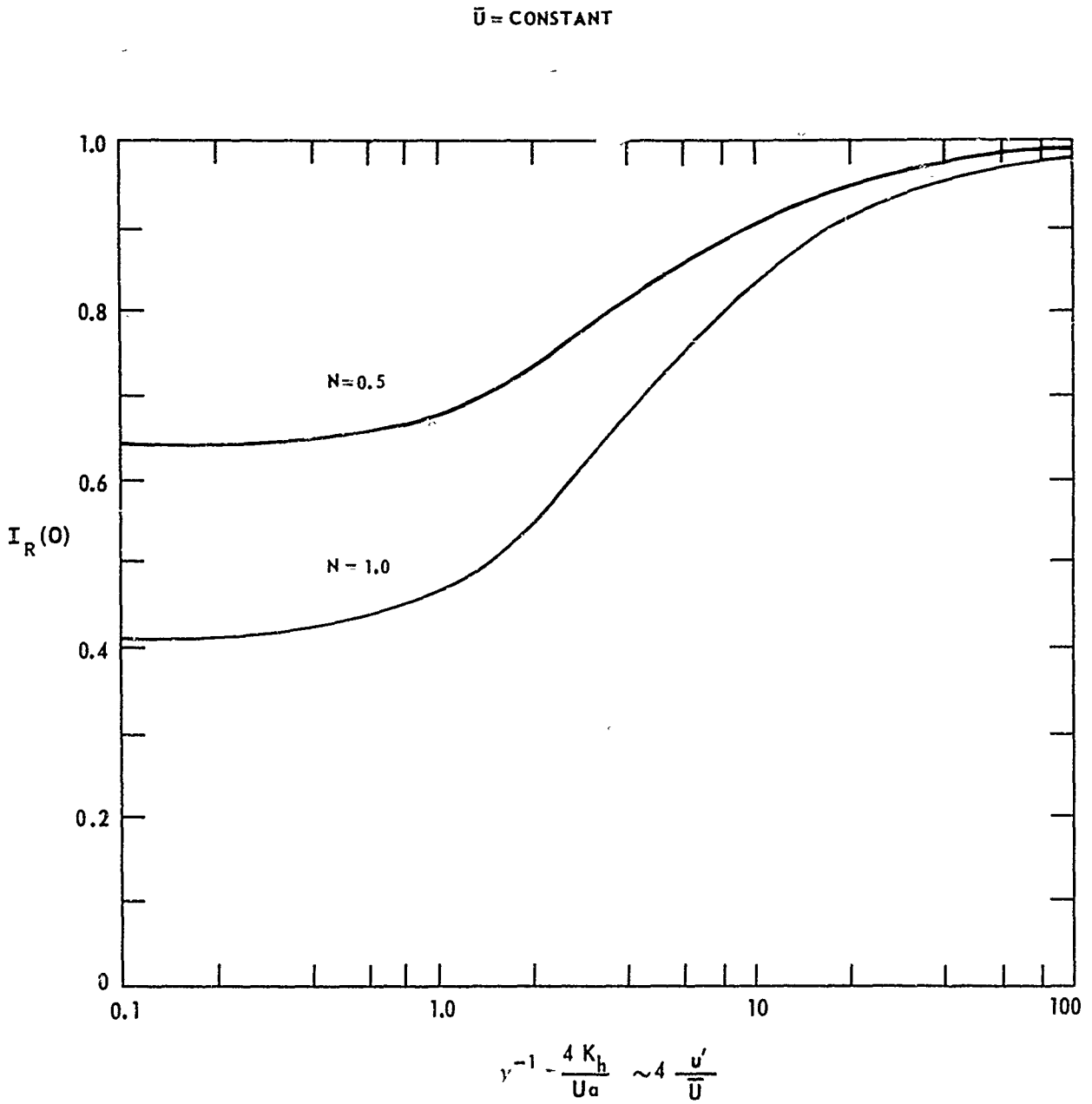

FIG. 29

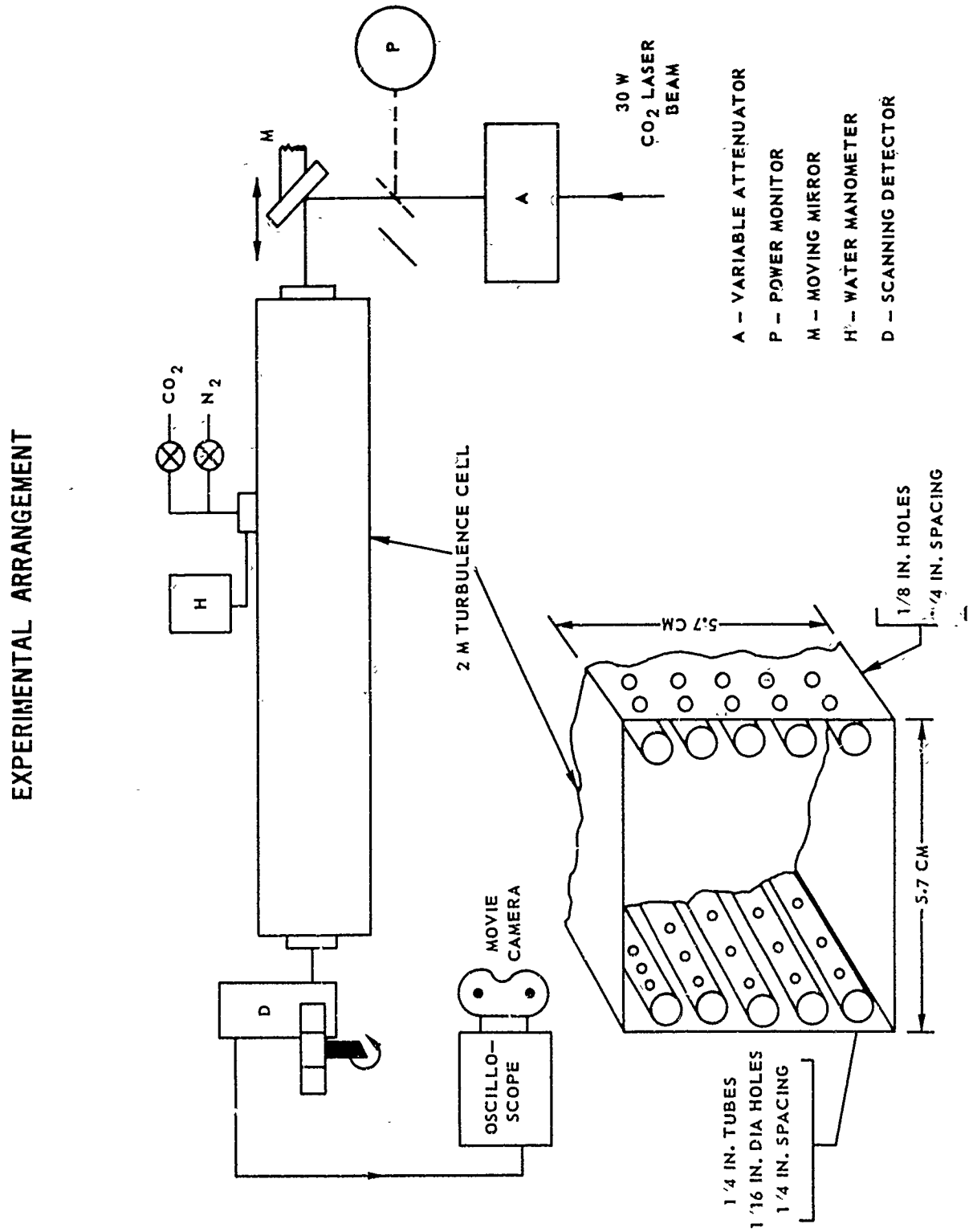
EXPERIMENTAL ARRANGEMENT
A – VARIABLE ATTENUATOR
P – POWER MONITOR
M – MOVING MIRROR
H – WATER MANOMETER
D – SCANNING DETECTOR
30 W CO_2 LASER BEAM
P
M
A
CO_2
N_2
H
2 M TURBULENCE CELL
D
MOVIE CAMERA
OSCILLO-SCOPE
5.7 CM
1/8 IN. HOLES
1/4 IN. SPACING
5.7 CM
1 1/4 IN. TUBES
1 1/16 IN. DIA HOLES
1 1/4 IN. SPACING

TURBULENCE EFFECTS ON STATIONARY CO_2 BEAM

100% CO_2

L921004-8

UNDISTORTED BEAM

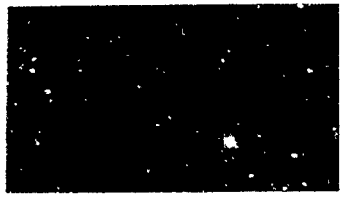

0 1 CM

TURBULENCE

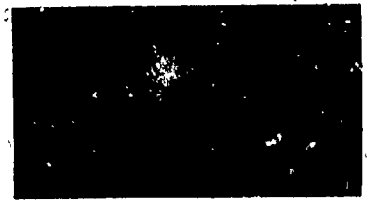

16 CM H_2O

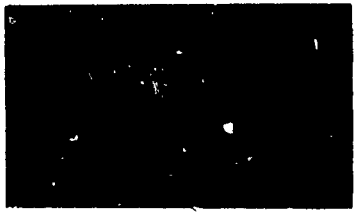

10 CM H_2O

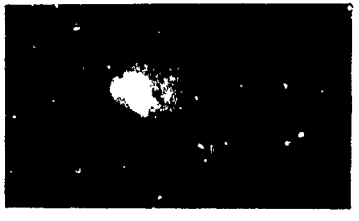

6 CM H_2O

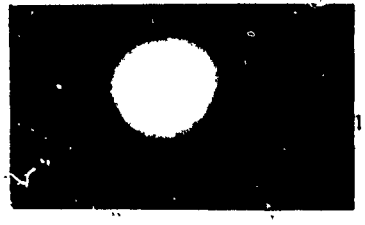

1.5 CM H_2O

$N_{nc} = 3.4$

$P = 8.8$ W

$\alpha t = 0.37$

$z = 2.1$ M

$a_i = 1.86$ MM

$a_o = 3.33$ MM

NATURAL CONVECTION

$V_{nc} \sim 3.4$ CM/SEC

FIG. 30

L92104-8

HeNe BEAM SUPERIMPOSED ON CO_2 BEAM

100% CO_2

STATIONARY BEAM

TURBULENCE LEVEL : 10 CM H_2O

$\alpha t = 0.37$

$t = 2M$

$Z = 2.2$ M

NO ABSORPTION

P_{CO_2} - 8W

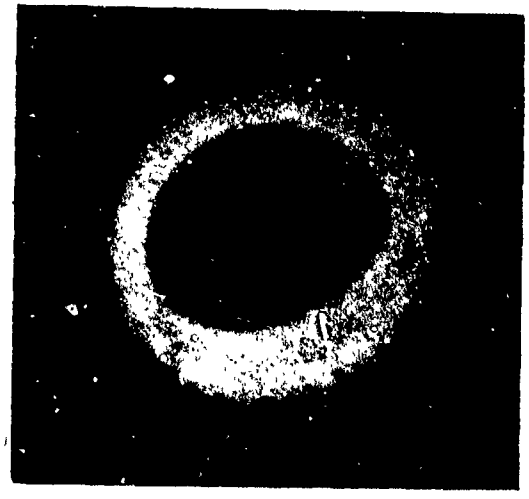

P_{CO_2} 27 W

FIG. 31

TURBULENCE EFFECTS ON STATIONARY BEAM

TURBULENCE LEVEL : 6 CM H_2O

100% CO_2

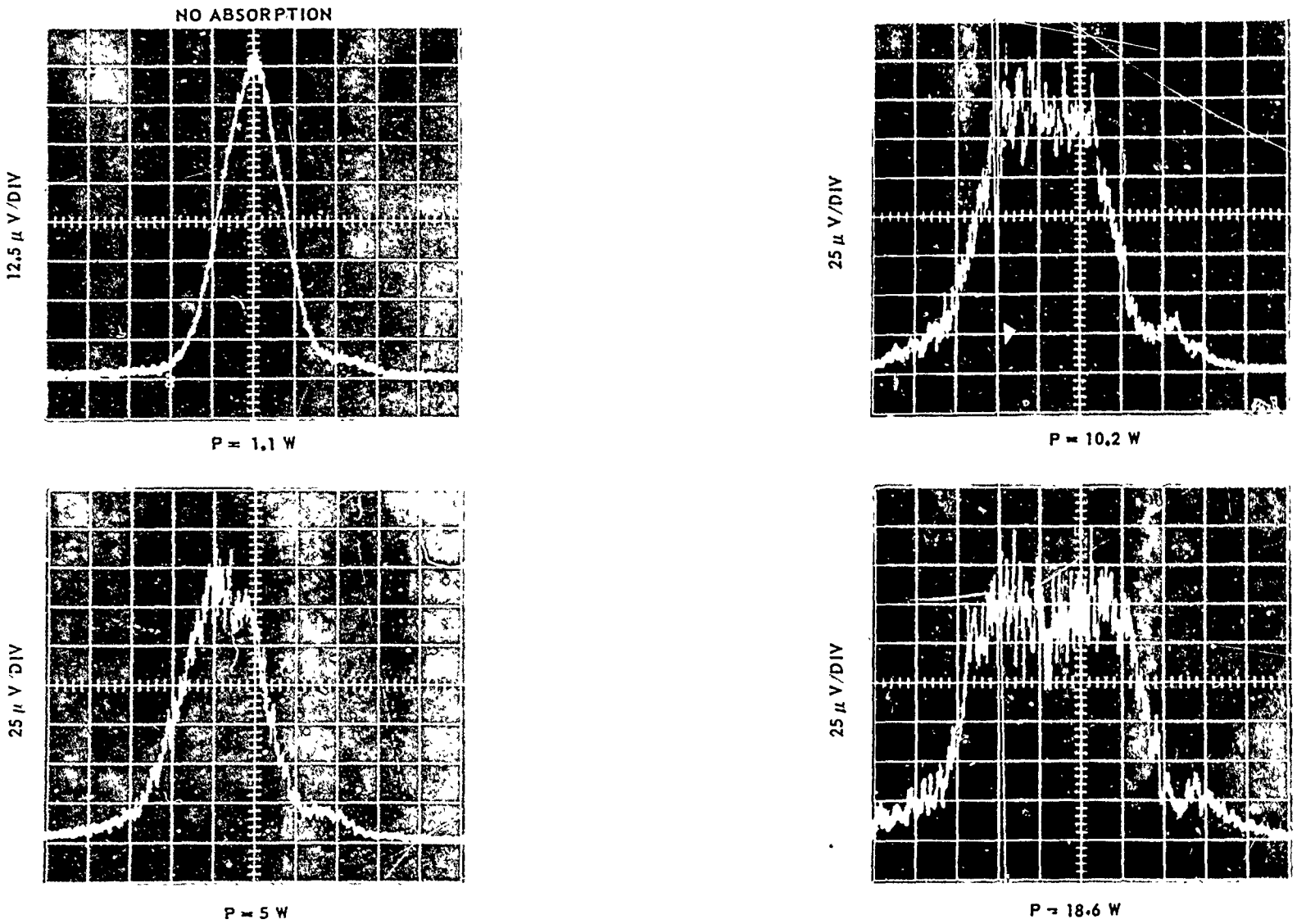

HORIZONTAL SCALE : 2.4 MM/DIV

L921004-8

FIG. 32

NORMALIZED MEAN ON-AXIS INTENSITY VS. POWER

STATIONARY BEAM

TURBULENCE LEVEL : 1.5 CM H_2O

100% CO_2

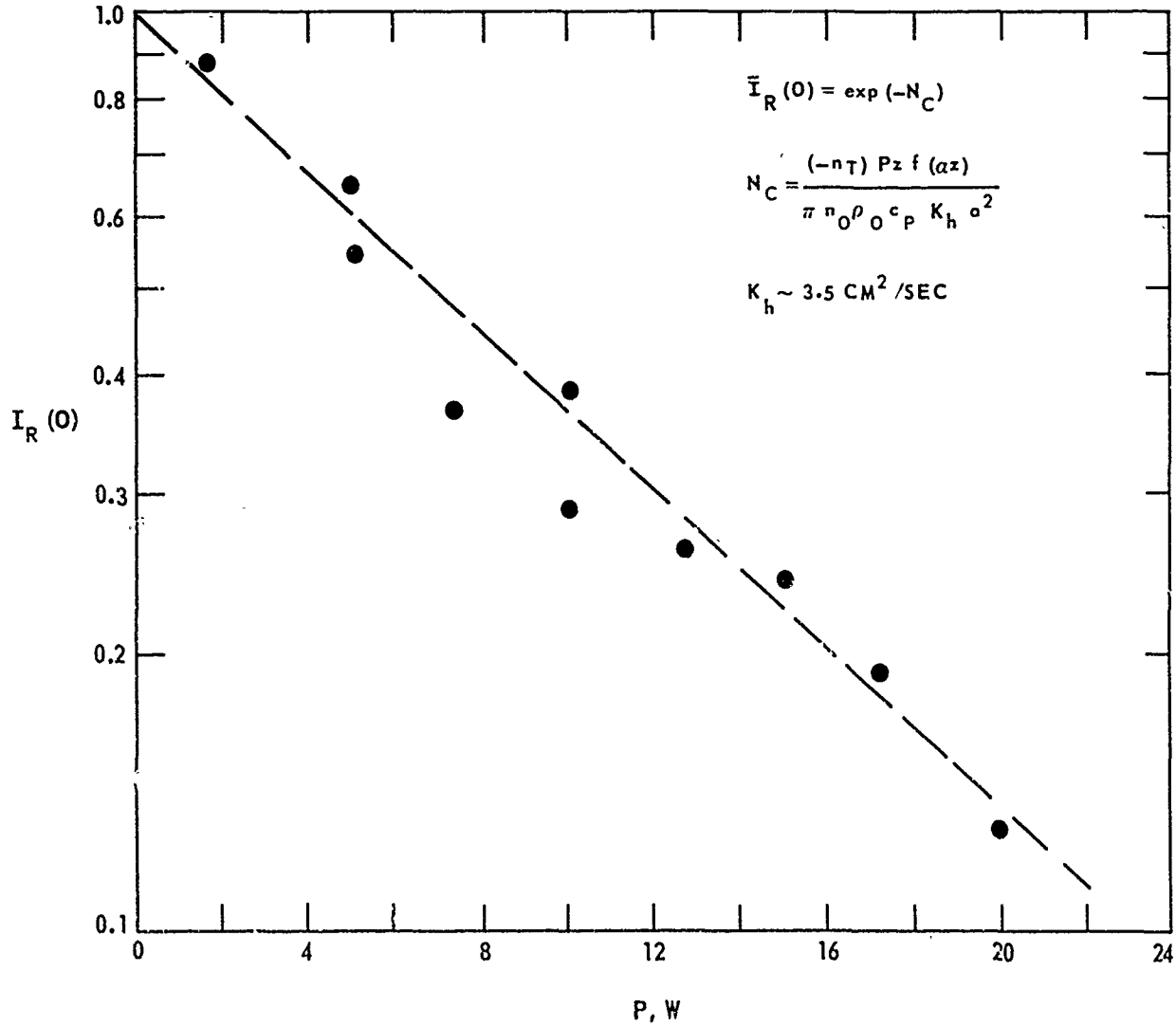

TURBULENCE EFFECTS ON THERMAL DISTORTION

WIND ⟶

HORIZONTAL SCALE : 3.8 MM DIV

VERTICAL SCALE : 62.5 μ V DIV

100% CO_2

UNDISTORTED BEAM

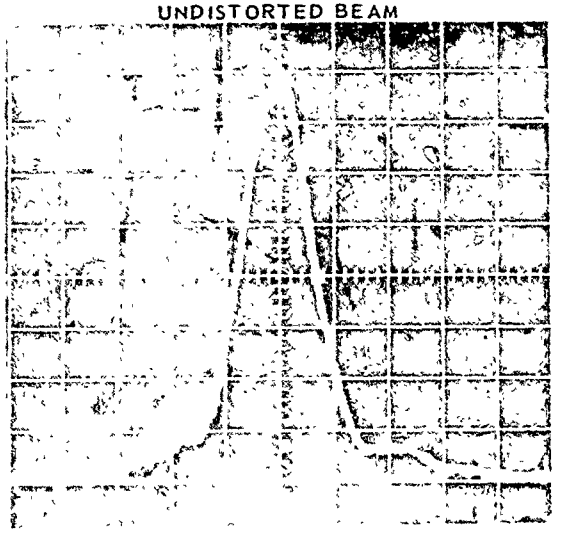

N = 11.3

P 17.7 W

$\bar{U}$ 2 CM SEC

αt 0.37

Z = 2.1 M

a_i = 1.86 MM

a_o = 3.43 MM

LAMINAR WIND

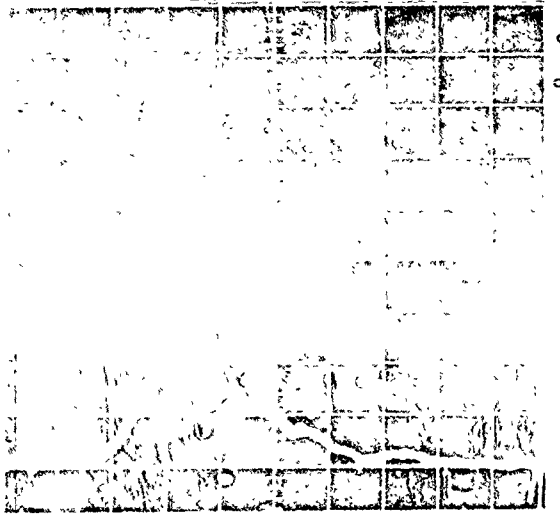

TURBULENCE AND WIND

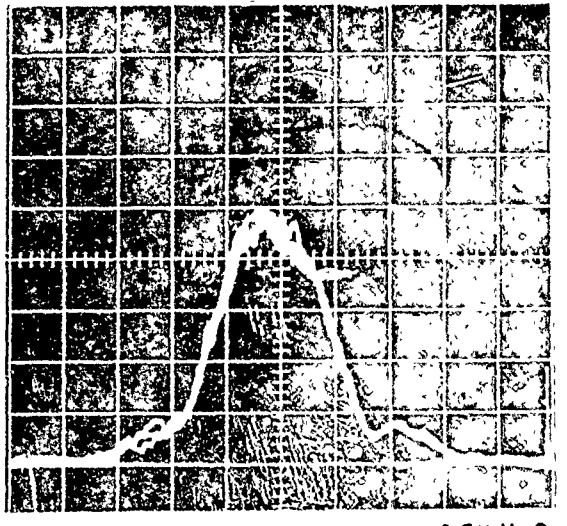

40 CM H_2O

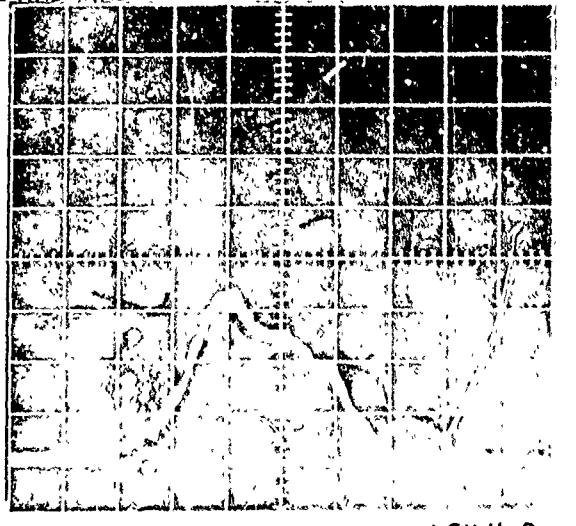

4 CM H_2O

10 CM H_2O

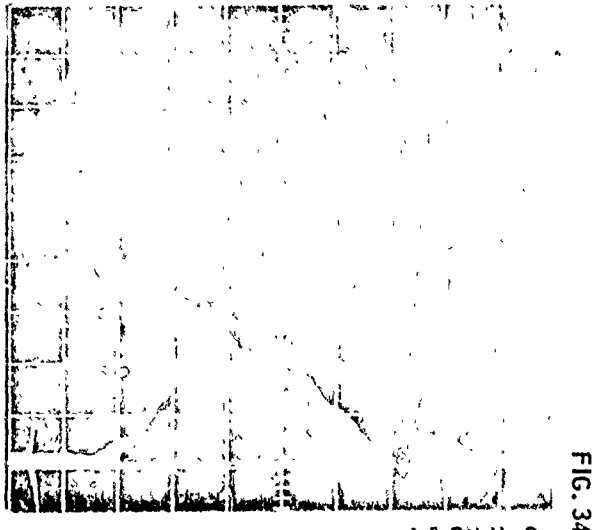

1.5 CM H_2O

L921064-8

FIG. 34

TURBULENCE EFFECTS ON THERMAL DISTORTION

WIND ⟶
HORIZONTAL SCALE 3.8 MM DIV
VERTICAL SCALE 31.25 μ V DIV
100% CO_2

UNDISTORTED BEAM

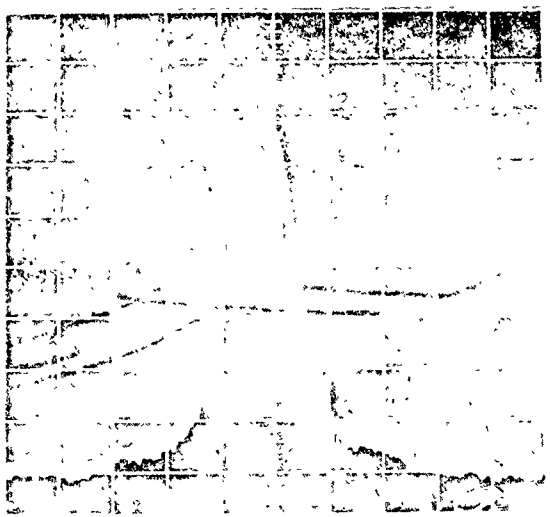

LAMINAR WIND

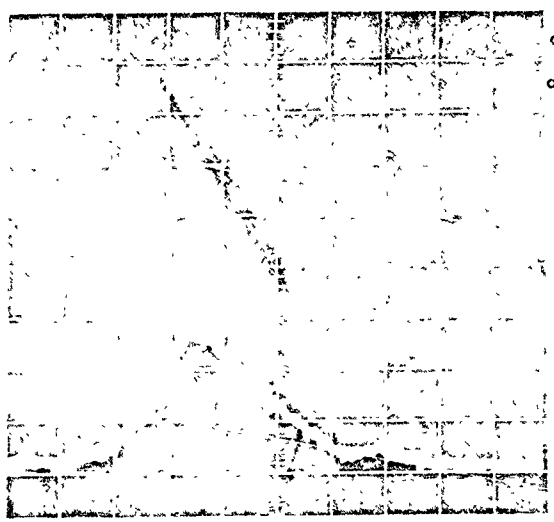

N = 11.8
P = 8.8 W
$\bar{U}$ = 1 CM SEC
αt = 0.37
Z = 2.1 M
a_i = 1.86 MM
a_o 3.33 MM

TURBULENCE AND WIND

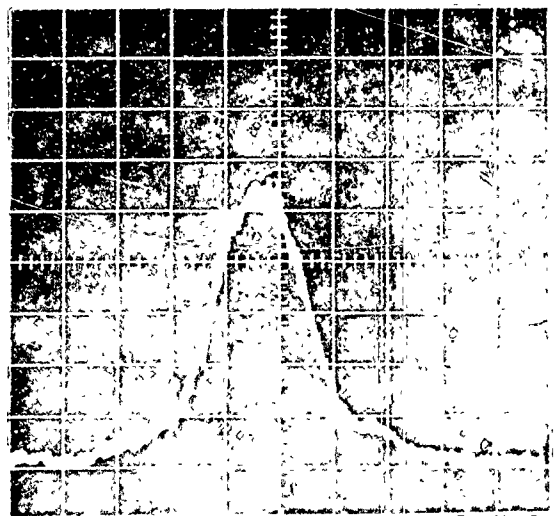

16 CM H_2O

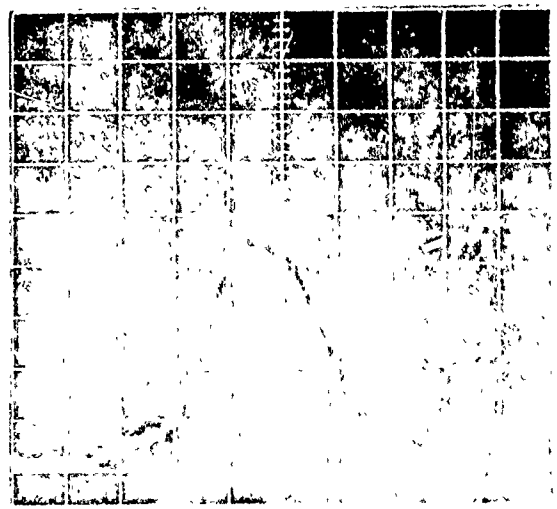

6 CM H_2O

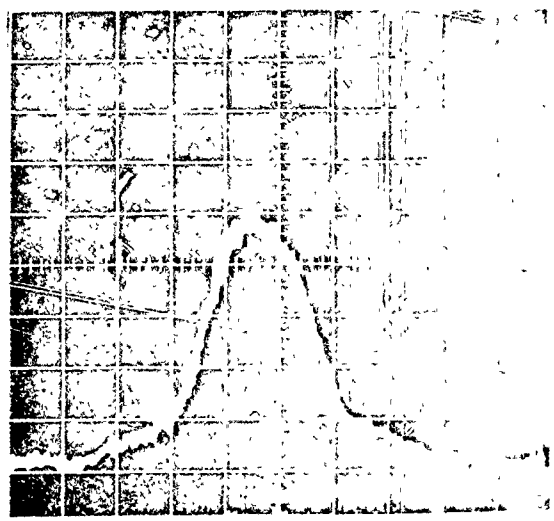

10 CM H_2O

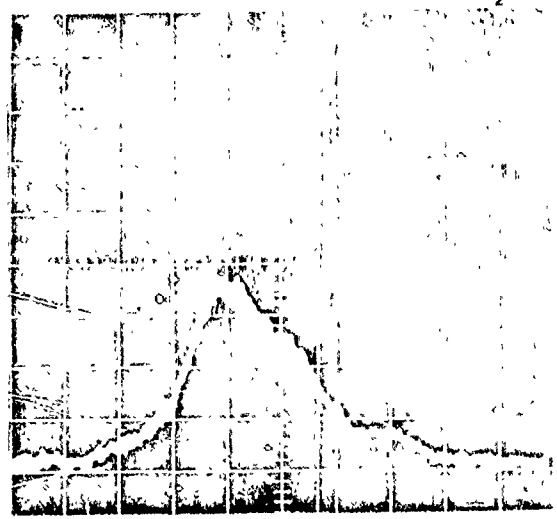

1.5 CM H_2O

L92004-8

FIG. 35

MEASURED CONSTANT INTENSITY CONTOURS

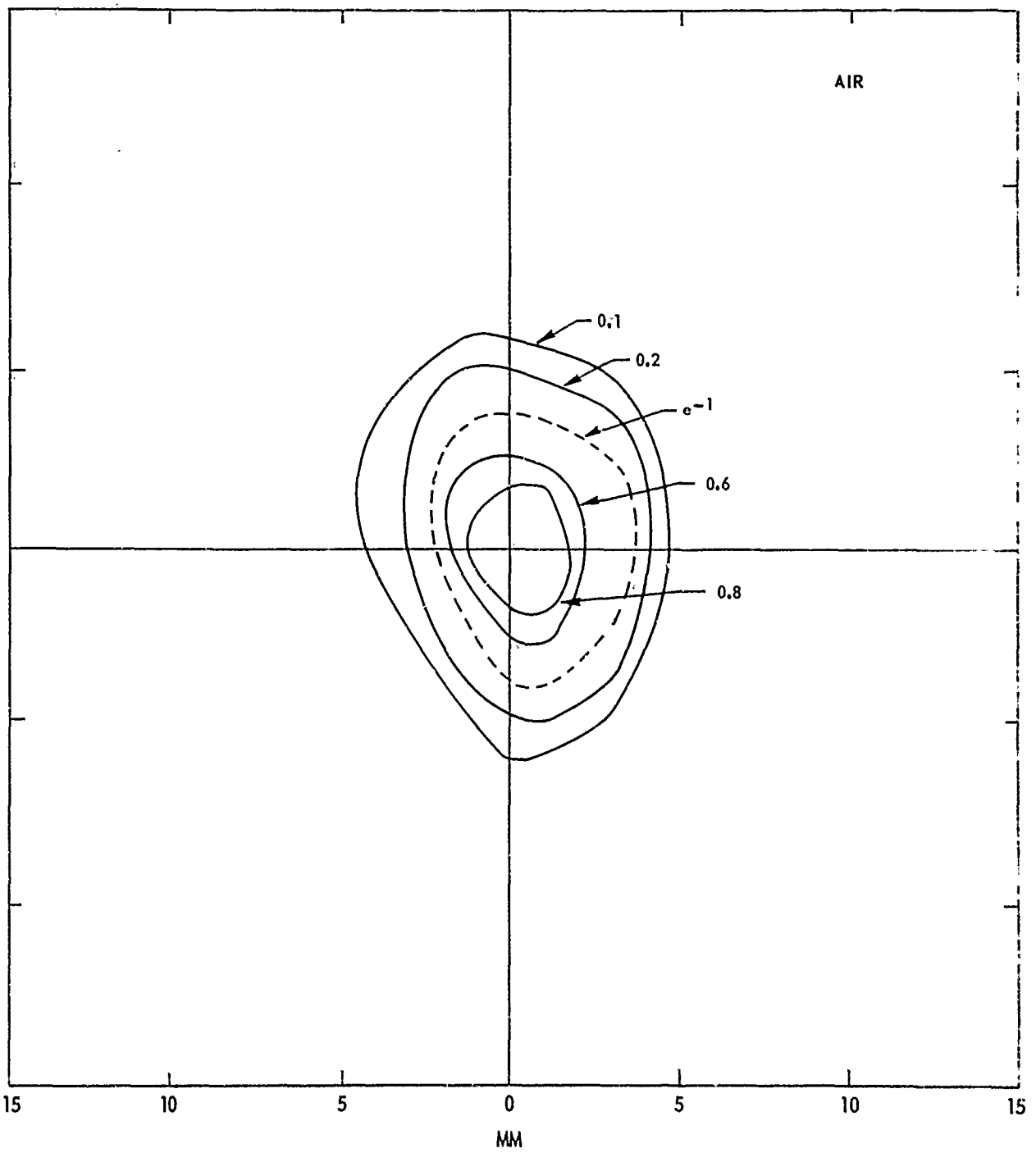

FIG. 37

MEASURED CONSTANT INTENSITY CONTOURS

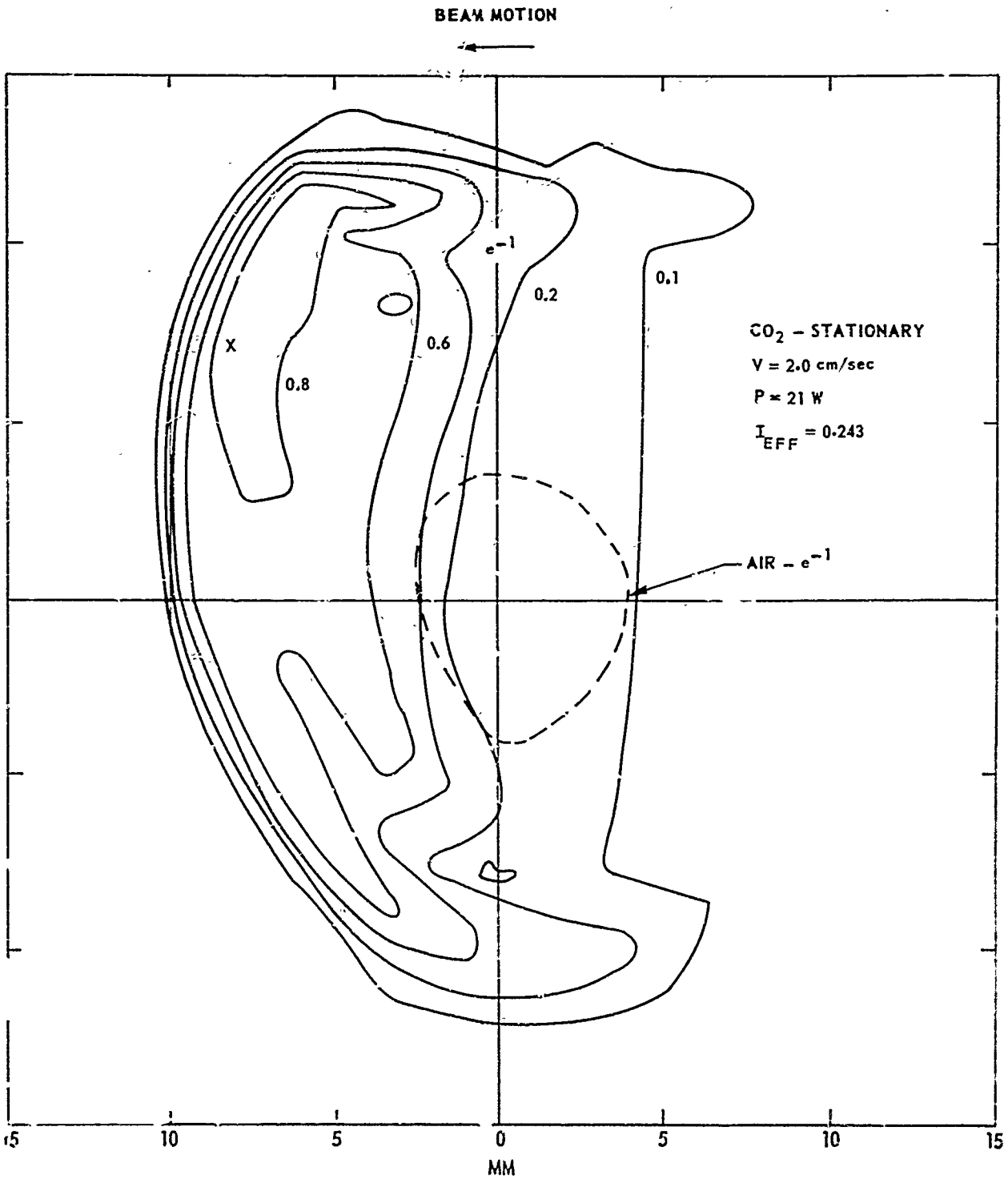

MEASURED CONSTANT INTENSITY CONTOURS

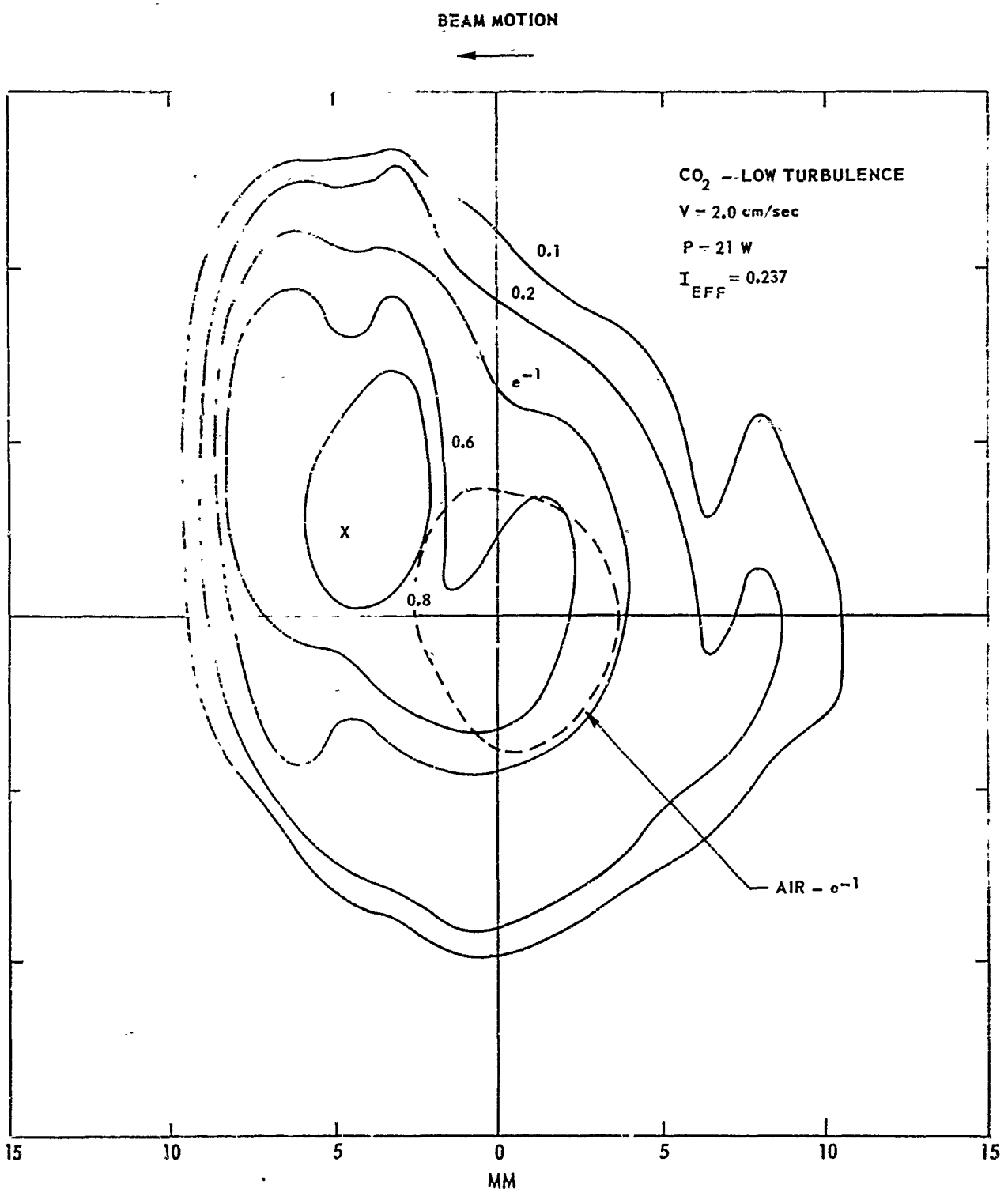

FIG. 39

MEASURED CONSTANT INTENSITY CONTOURS

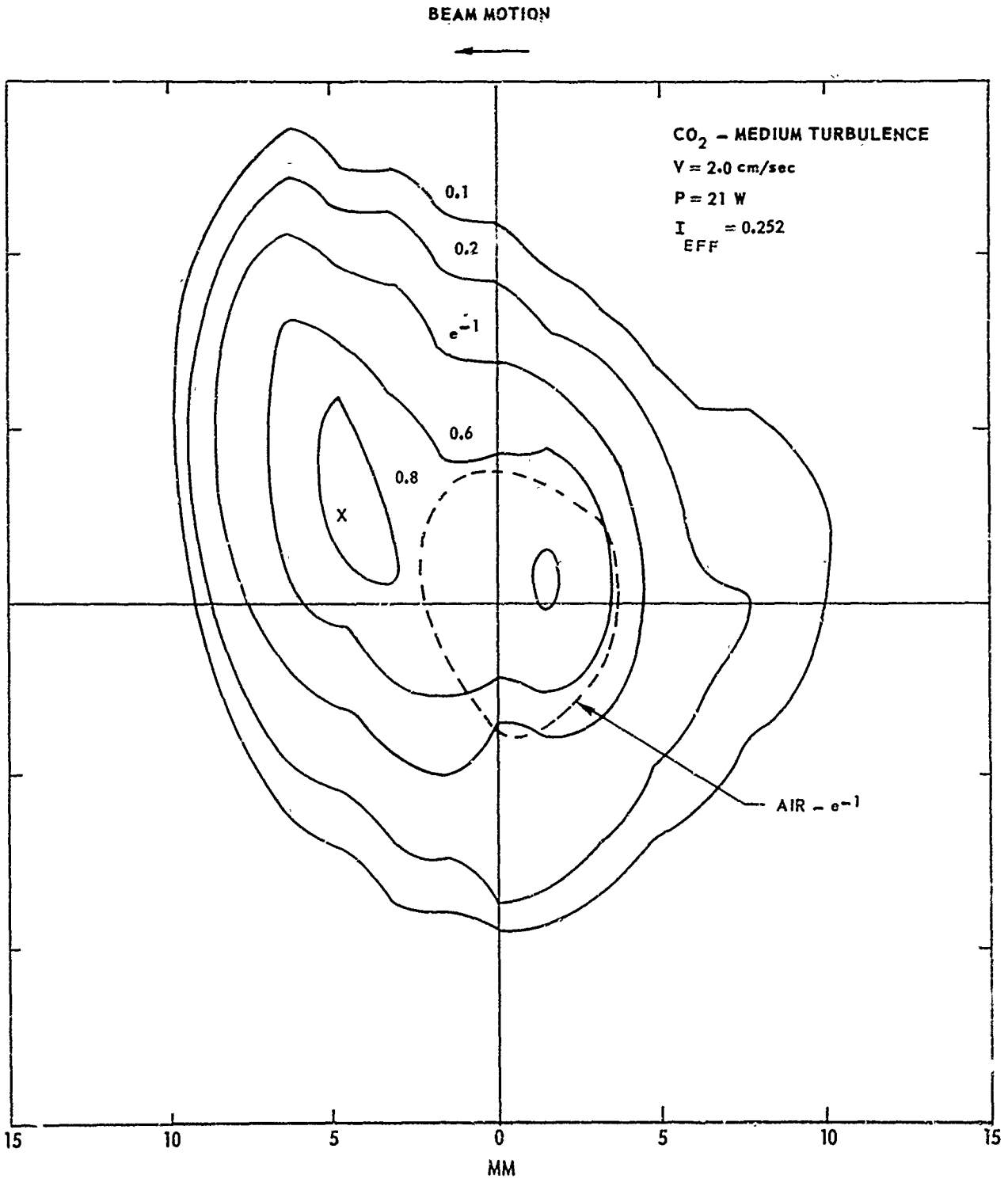

MEASURED CONSTANT INTENSITY CONTOURS

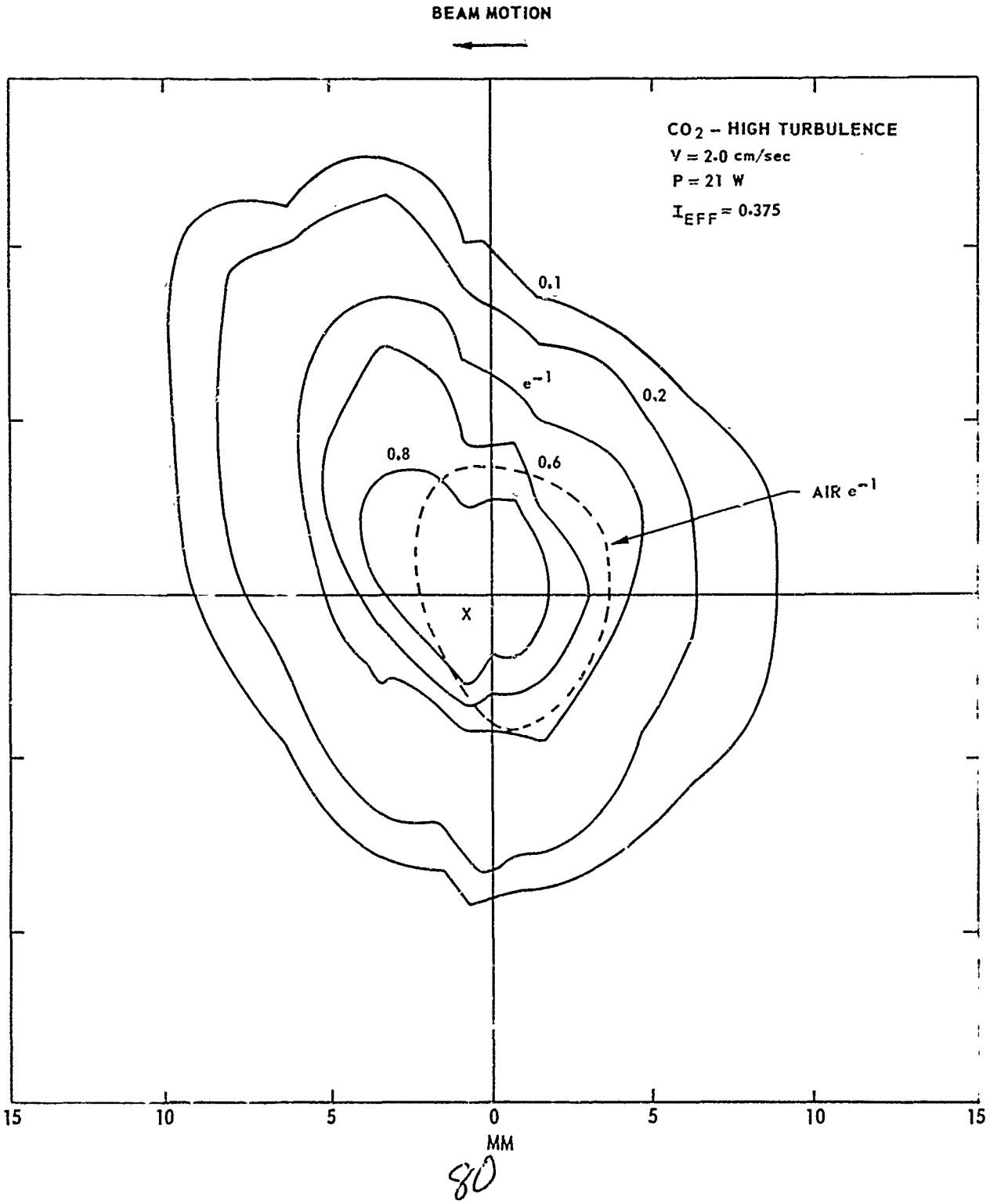

FIG. 41

MEASURED CONSTANT INTENSITY CONTOURS

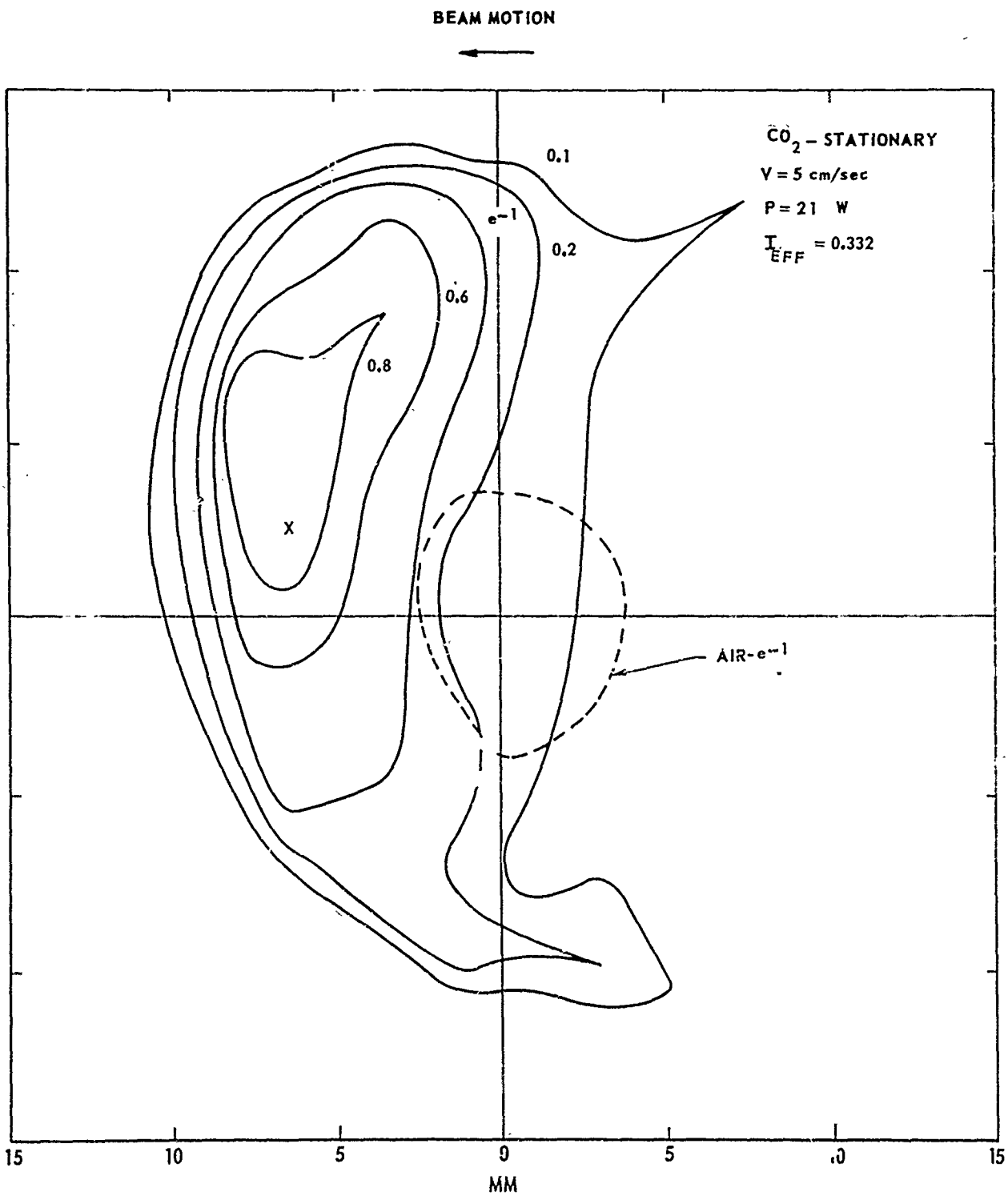

FIG. 42

MEASURED CONSTANT INTENSITY CONTOURS

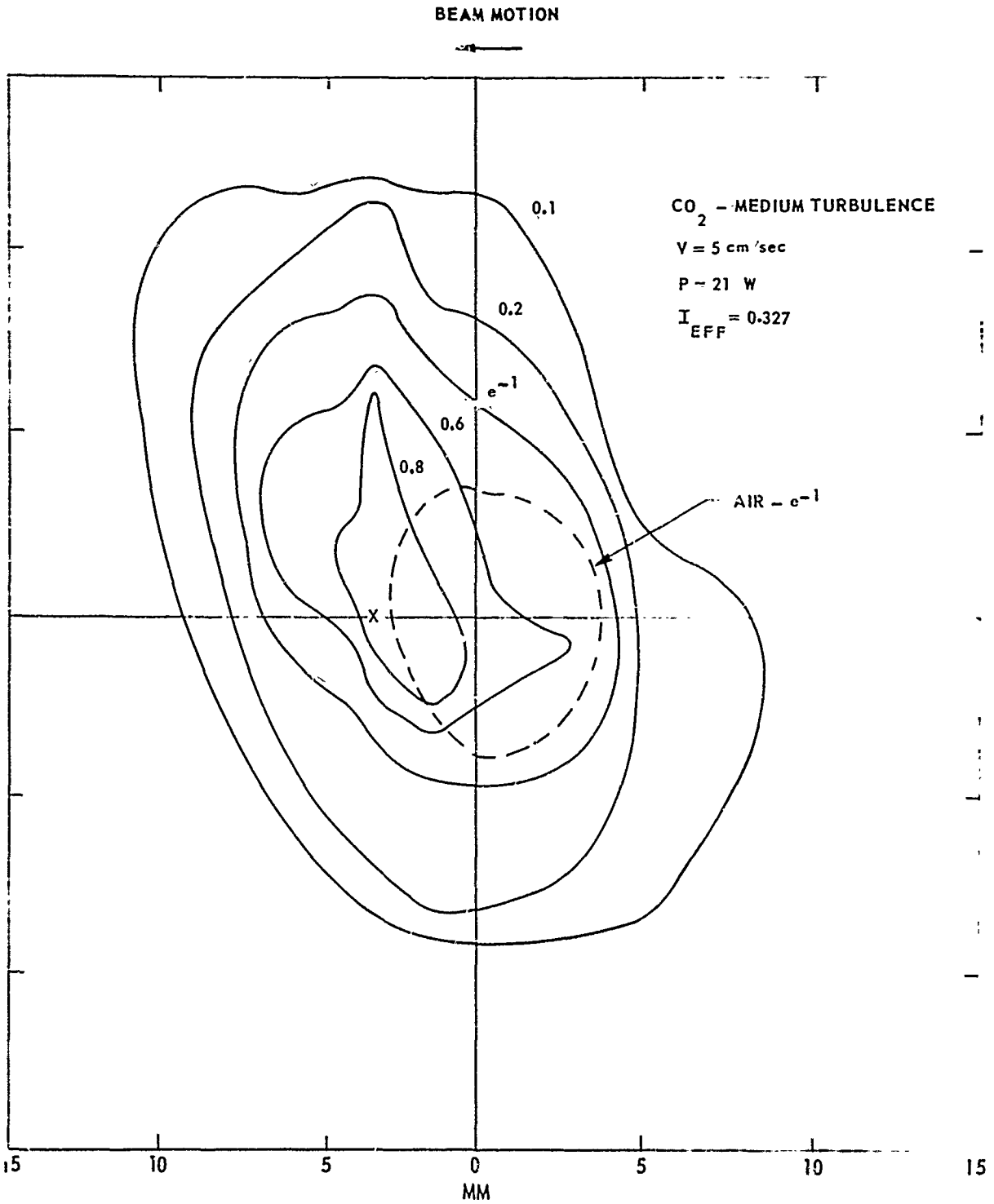

FIG. 43

MEASURED CONSTANT INTENSITY CONTOURS

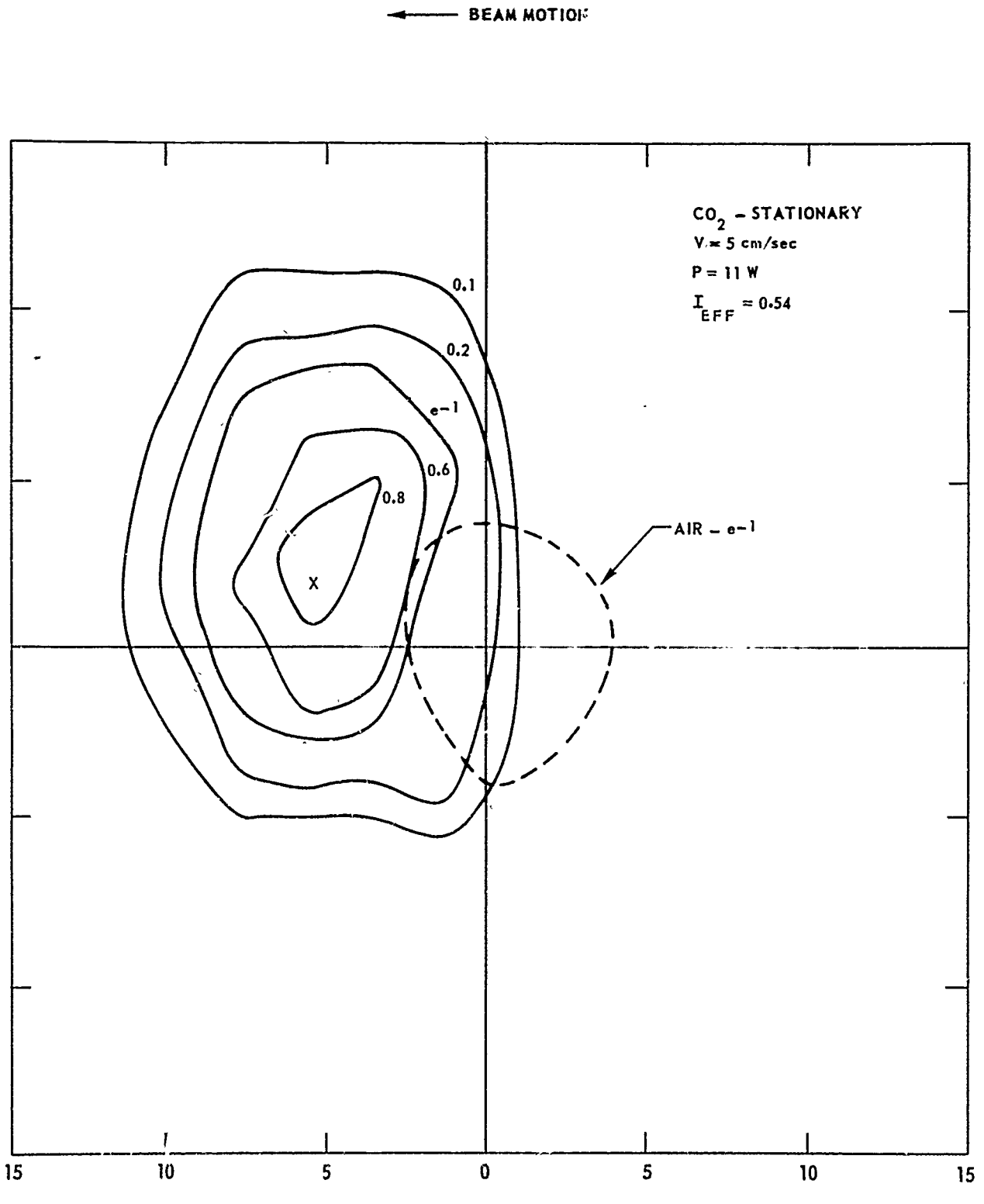

FIG. 44

MEASURED CONSTANT INTENSITY CONTOURS

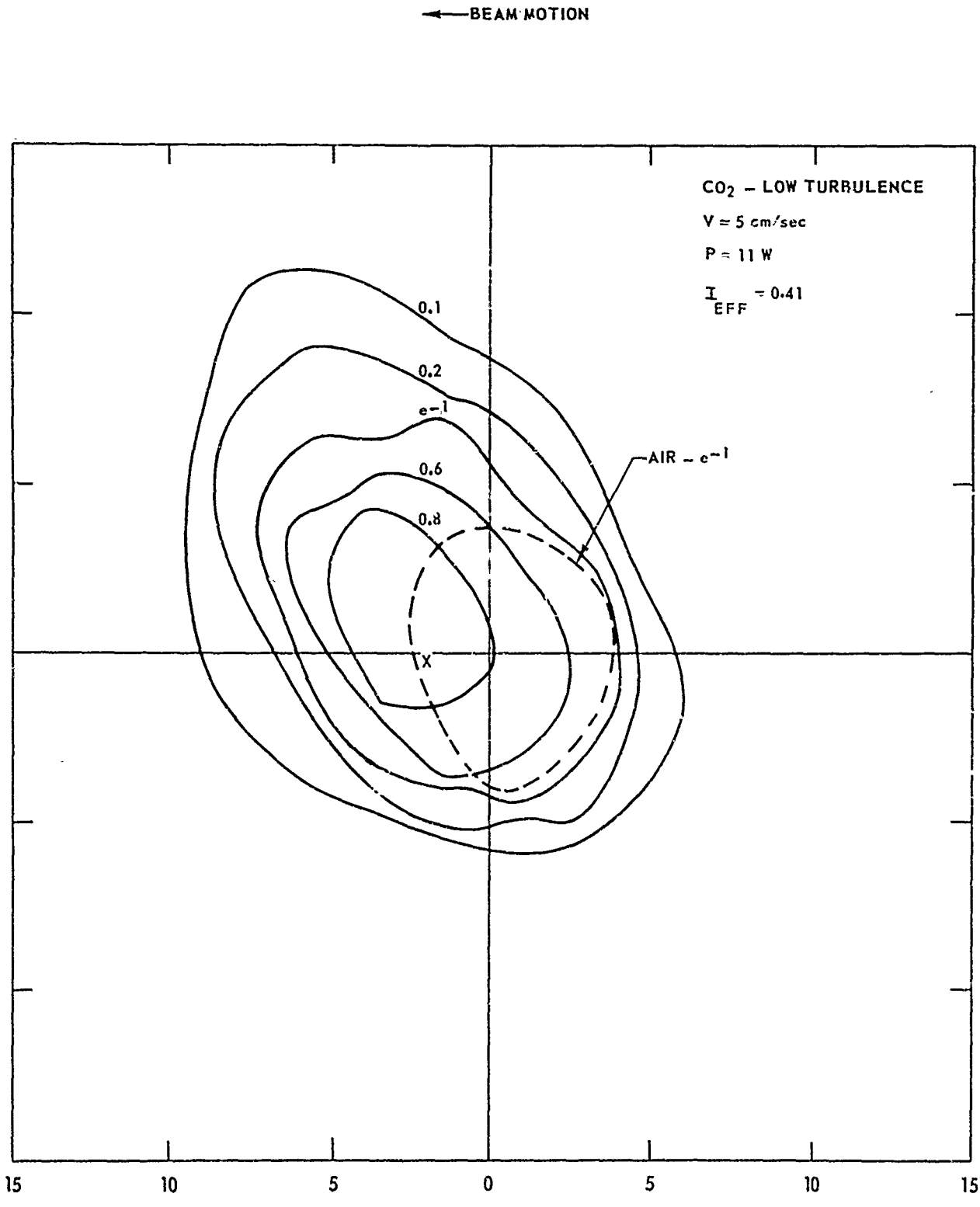

MEASURED CONSTANT INTENSITY CONTOURS

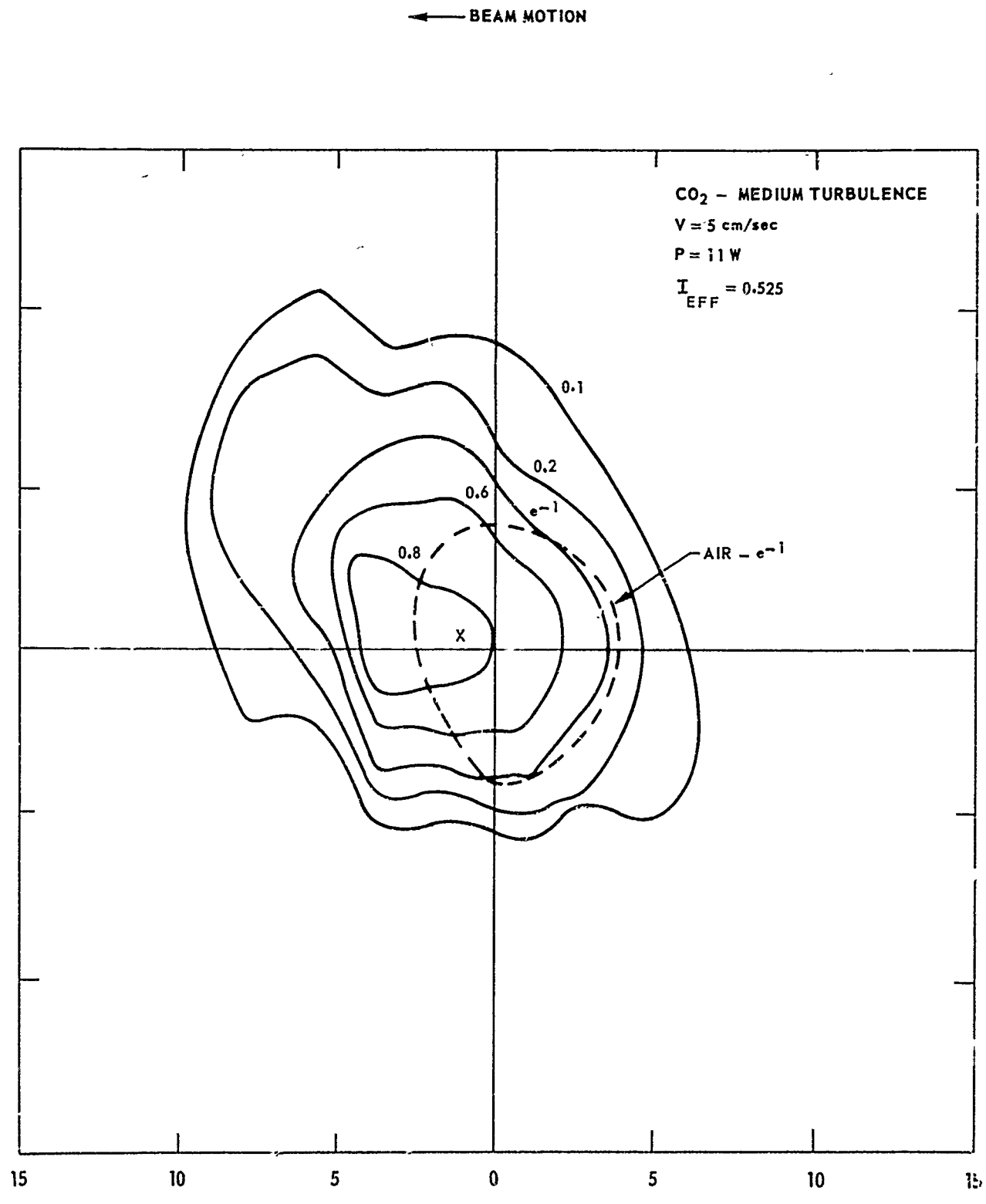

FIG. 46

MEASURED CONSTANT INTENSITY CONTOURS

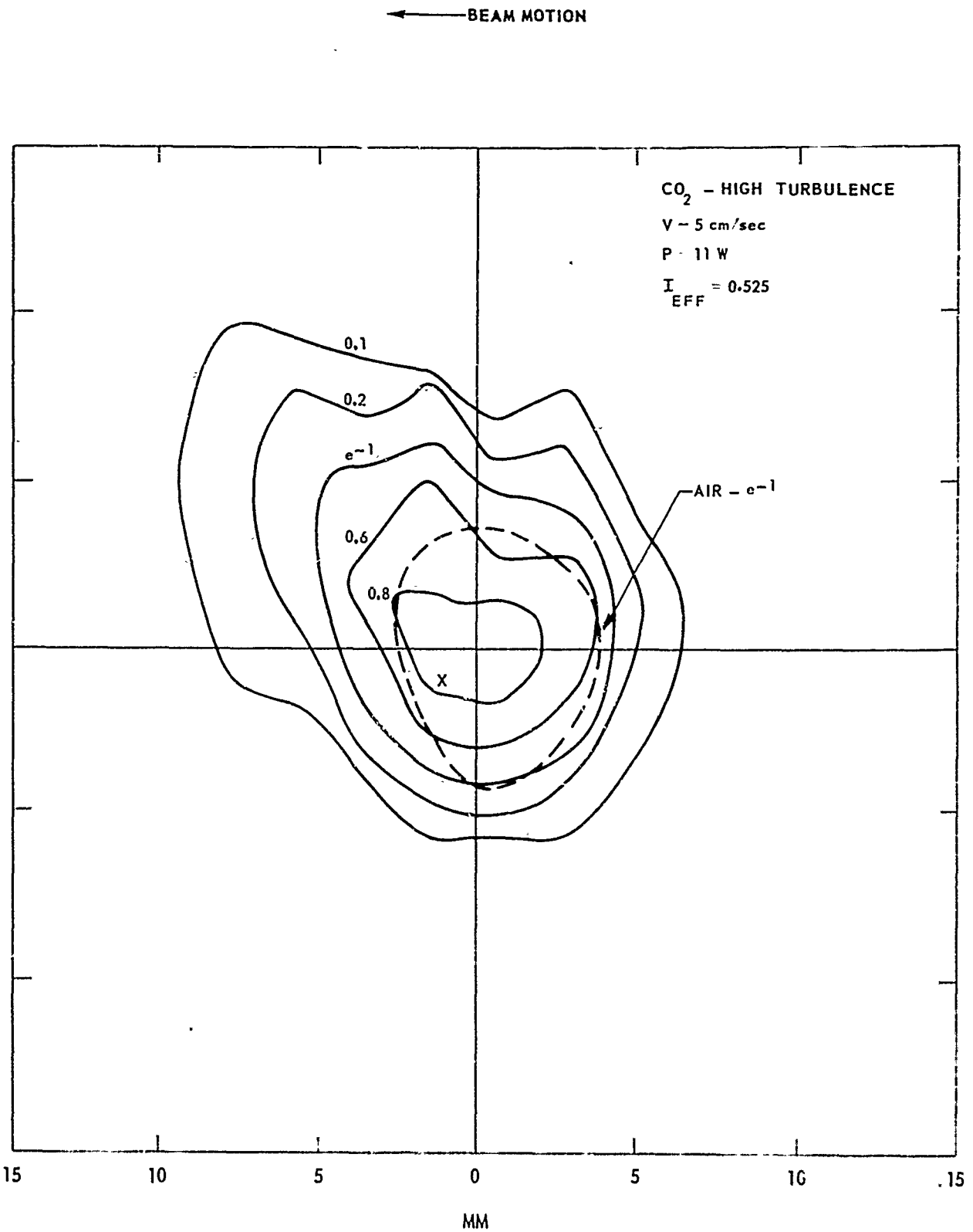

FIG. 47

TURBULENT DIFFUSION DIAGRAM

(FROM H. LETTAU, "COMPENDIUM OF METEOROLOGY," 1951)

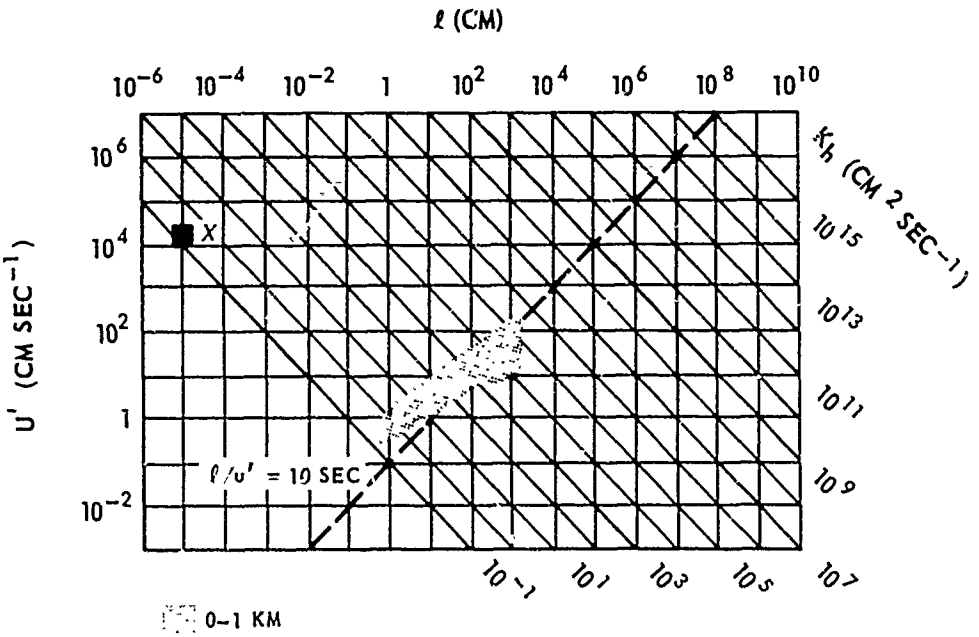

$\ell \approx$ BEAM RADIUS a

$a = 10$ CM

$u' = 1\text{–}10$ CM/SEC $\quad (\bar{u} \approx 10\text{–}200$ CM/SEC)

$K_h = 10\text{–}10^2$ CM^2/SEC

$$\gamma - 1 = \frac{4K_h}{\bar{u}a} \approx 0.4\text{–}0.2$$

57

APPENDIX A

Comparison of Beam Translation with Wind Tunnel Flow

As a result of some previous discussions regarding the poor agreement with theory of the beam deflection results obtained in gases (see Ref. 1, Fig. 27), it was decided to compare the thermal distortion effects obtained with beam translation in a quiet gas with those obtained using the gas flow in the circulating, 50 cm path wind tunnel. The wind tunnel was filled with a mixture of air and propylene which provided enough absorption to give a value of $N \sim 4$ with a 5 cm/sec wind or translation velocity and a 10 watt laser beam power. The distorted profiles were measured first with the laser beam translating across the quiet gas and then with the laser beam stationary in the wind tunnel gas flow. The hot wire anemometer used to measure the wind tunnel flow velocity was calibrated by placing the probe on the mechanical scanner used for beam translation. In Fig. A-1, the results are shown comparing the thermal distorted intensity profiles as obtained by the two different methods. There is a significant difference between the distortion obtained with beam translation at 5 cm/sec and the 5 cm/sec wind tunnel gas flow velocity. With beam translation, the shape and deflection of the distorted intensity profile appear to be in reasonable agreement with theoretical predictions. In the wind tunnel flow case, however, the distorted intensity profile has two peaks and is broader than with beam scanning at 5 cm/sec. Although increasing the wind velocity and laser beam power by a factor of two leaves the distortion parameter, N, unchanged, the resulting distorted intensity profile in Fig.A-1is clearly seen to more closely approximate the distortion obtained using beam translation. Increasing the wind tunnel velocity further decreases the the distortion parameter, N, while improving the agreement of the distorted intensity profiles with theory. Thus, the discrepancy between the case of beam translation and the use of wind tunnel gas flow appears to be associated with the magnitude of the flow velocity.

To investigate the wall boundary layer as a possible cause for the observed discrepancy, the wind velocity profiles near the wall were measured for the two free-stream velocities of 5 and 20 cm/sec. The results, shown in Fig.A-2, indicate an increase in the boundary layer thickness from $\frac{1}{2}$ to $1\frac{1}{2}$ inches as the velocity decreases from 20 to 5 cm/sec. This suggests that the reduced velocity associated with the boundary layer near the wind tunnel entrance window may be responsible for the difference between the gas flow and beam translation cases.

Turbulence effects do not appear to be important in these wind tunnel gas flow experiments since the distorted profiles are observed to be very repeatable (e.g., the data in Fig.A-1, represent several scans of the distorted beam) with essentially no random fluctuations.

Based on the results of this experiment, the relatively poor agreement with theory of some of the previous data obtained using wind tunnel flow (e.g., see Ref. 1, Fig. 27) may be attributed to the boundary layer thickness rather than the effects of conduction or gas heating as cited earlier. Thus, for the largest values of N, where the largest deviations from theory were observed, the wind tunnel velocities were becoming very small with an accompanying increase in the boundary layer dimension.

In summary, it is now clear that thermal distortion experiments using wind tunnel gas flow must be carefully monitored to avoid boundary layer and possibly turbulence effects. It also appears that with beam translation, the experiments can be carried out much more simply and with accurately simulated conditions for large values of N, even in gases.

COMPARISON OF BEAM TRANSLATION WITH WIND TUNNEL FLOW

L92104-8

UNDISTORTED BEAM
N = 0

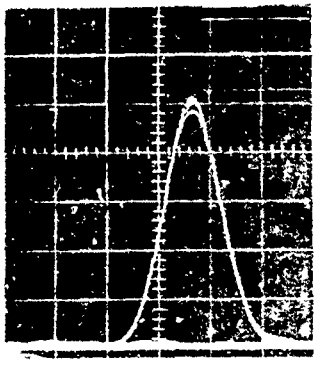

50 cm PATH WIND TUNNEL
GAS MIXTURE: AIR + PROPYLENE
z = 60 cm
HORIZONTAL SCALE: 1.9 mm/div

BEAM TRANSLATION

WIND TUNNEL FLOW

v_S = 5 cm/sec P = 10 W

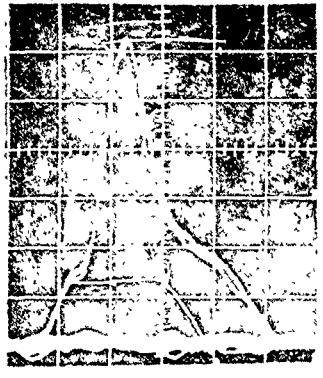

N = 4

v_W = 5 cm/sec P = 10 W

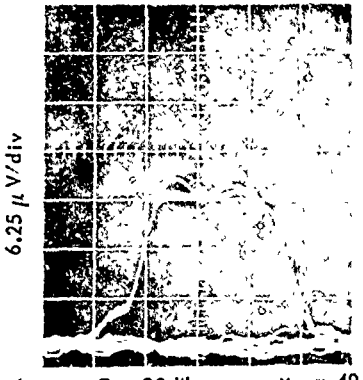

v_W = 10 cm/sec P = 20 W

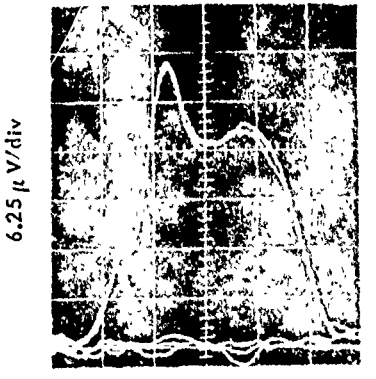

v_W = 20 cm/sec P = 20 W

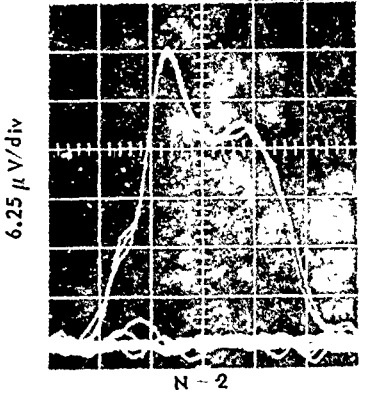

N = 2

v_W = 40 cm/sec P = 20 W

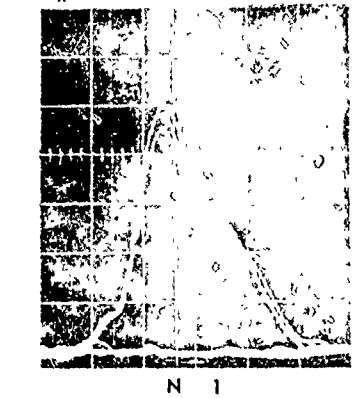

N 1

v_W = 80 cm/sec P = 20 W

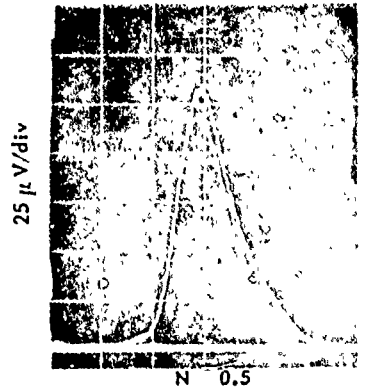

N 0.5

A-3

FIG. A-1

FIG. A -2

MEASURED WIND TUNNEL VELOCITY PROFILE

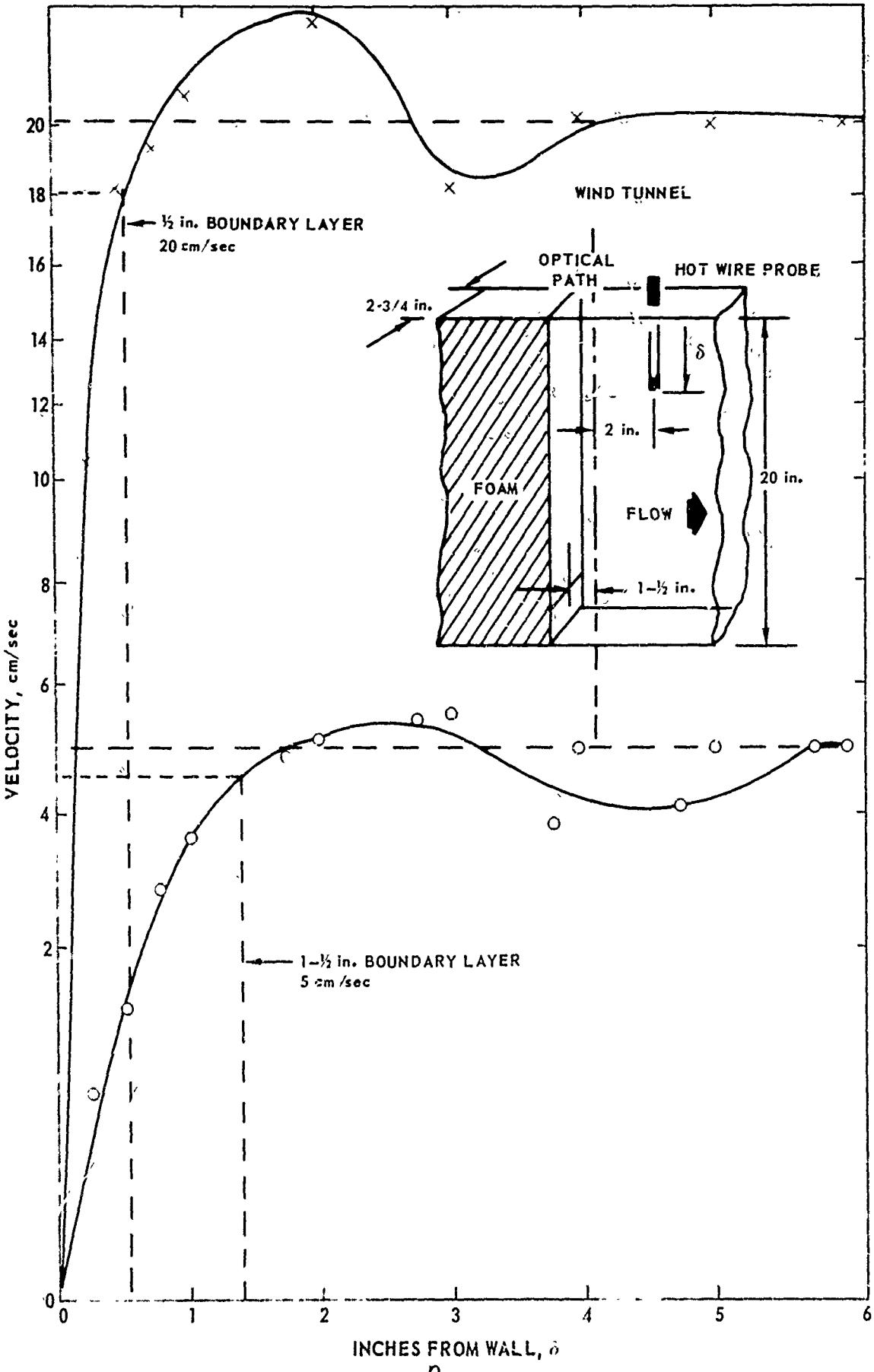

APPENDIX B

The Distortion Parameter for Focused and Diverging Beams and for Beam Slewing

The form of the distortion parameter N derived previously (Ref. 1, Sec. 3.3) to account for focused beam propagation has been found to be correct only in the limit of a very small amount of focusing or divergence of the beam. The general form of the distortion parameter for focused or diverging gaussian beams in a uniform laminar wind is derived in this appendix. The form of N appropriate for the slewing of a collimated gaussian beam is also given.

The change in intensity of a laser beam due to gradients in the refractive index can be written (Ref. 19)

$$\frac{I(x,y,z)}{I_u\, e^{-\alpha z}} = \exp\,(\Psi) \qquad \text{(B-1)}$$

where

$$\Psi = -\int_o^z \left(\nabla_t + \frac{\nabla_t I}{I}\right) \cdot \int_o^{z'} \frac{\nabla_t n}{n_o}\, dz''\, dz' \,, \qquad \text{(B-2)}$$

I_u is the indistorted intensity, i.e., the intensity in a homogeneous loss-free medium, $n = n_o + \delta n$ is the refractive index with $|\delta n/n_o|$ assumed to be $\ll 1$, α is the linear attenuation coefficient, z is the propagation direction and ∇_t is the transverse gradient operator. For the case of a convection dominated thermal lens (i.e., a transverse wind or beam motion from slewing or a moving source) the normalized refractive index gradient is (Ref. 19)*

$$\frac{\nabla_t n}{n_o} = \epsilon(z)\left(\hat{x}\, I + \hat{y} \int_{-\infty}^{x} \frac{\partial I}{\partial y}\, dx'\right) \qquad \text{(B-3)}$$

where

$$\epsilon\,(z) = \frac{(dn/dT)\,\alpha}{n_o\,\rho\,c_p\,v} \,, \qquad \text{(B-4)}$$

*Although kinetic cooling is not included here to simplify the derivation it could easily be incorporated in Eq. (B-3) by comparison with Eq. (15) and (16). The expression for N is the same in both cases, however.

which is written as a function of z to account for changes in the properties of the medium along the propagation path. For example, the altitude dependence of the absorption coefficient and the properties of the air could be accounted for along a non-horizontal propagation path; or, the wind velocity may be non-uniform along the propagation path. The distortion parameter N is essentially the dimensionless factor that multiplies the geometric terms in Eq. (B-2) if a perturbation expression is obtained by assuming $I = I_u e^{-\alpha z}$. Here we wish to obtain the general form for Ψ that applies for an uncollimated gaussian beam with a nonuniform transverse wind or beam motion, e.g., such as slewing along a horizontal propagation path.

Thus, assuming for the undistorted beam the uncollimated gaussian intensity profile

$$I_u(x,y,z) = \frac{P}{\pi a^2(z)} e^{-(x^2+y^2)/a^2(z)} \quad . \tag{B-5}$$

The beam radius a(z) can be written

$$a(z) = a_o f(z) \quad , \tag{B-6}$$

where a_o is the beam radius in the source plane z=0. For the velocity we assume

$$v(z) = v_o g(z) \tag{B-7}$$

where v_o is the velocity at z=0. Changing to the normalized variables

$$\begin{aligned} u &= x/a(z) \\ w &= y/a(z) \end{aligned} \tag{B-8}$$

and using Eqs. (B-5) - (B-7) in Eq. (B-3) gives

$$\frac{\nabla_t n}{n_o} = \frac{\epsilon_o P}{\pi a_o^2} \left(\hat{x}\, h + \hat{y} \int_{-\infty}^{u} \frac{\partial h}{\partial w} \, du' \right) \frac{e^{-\alpha z}}{g f^2} \quad , \tag{B-9}$$

where $\epsilon_o = \epsilon(z=0)$ is a constant and

$$h(u,w) = e^{-(u^2+w^2)} \quad . \tag{B-10}$$

Using Eq. (B-9) in Eq. (B-2) leads to the general expression for the thermal distortion exponent

$$\Psi = -\frac{\epsilon_o P}{\pi a_o^3}\left\{\int_o^z \left[\hat{x}\left(\frac{\partial}{\partial u} + \frac{1}{h}\frac{\partial h}{\partial u}\right) + \hat{y}\left(\frac{\partial}{\partial w} + \frac{1}{h}\frac{\partial h}{\partial w}\right)\right]\frac{1}{f(z)} \cdot \int_o^{z'}\left[\hat{x}\, h + \hat{y}\int_{-\infty}^{u}\frac{\partial h}{\partial w}\,du'\right]\frac{e^{-\alpha z''}}{g(z'')\,f^2(z'')}\,dz''\,dz'\right\}. \quad \text{(B-11)}$$

To obtain a tractable expression for the distortion parameter it is necessary to ignore the z- dependence in h and the coordinates u,w, so that the terms within the square brackets can be removed from the z- integrations. This can be regarded as being equivalent to evaluating Ψ near the axis (i.e., for $u \approx w \approx 0$) where it becomes simply a constant indicating the change in on-axis intensity. Equation (B-11) thus becomes

$$\Psi = N\left\{\frac{\partial h}{\partial u} + \tfrac{1}{2}\int_{-\infty}^{u}\frac{\partial^2 h}{\partial w^2}\,du' + \frac{1}{2h}\frac{\partial h}{\partial w}\int_{-\infty}^{u}\frac{\partial h}{\partial w}\,du'\right\} \quad \text{(B-12)}$$

where

$$N = N_c\left\{\frac{2}{z^2}\int_o^z \frac{1}{f(z')}\int_o^{z'}\frac{e^{-\alpha z''}}{g(z')\,f^2(z'')}\,dz''\,dz'\right\} \quad \text{(B-13)}$$

is the general expression for the distortion parameter for the case of an uncollimated beam with a varying velocity along the propagation path. N_c is the familiar (e.g., see Ref. 19 Eq. (2.4)) collimated beam distortion parameter given by

$$N_c = \frac{-\epsilon_o P z^2}{\pi a_o^3} = \frac{(-dn/dT)\,P\,\alpha\, z^2}{\pi n_o \rho c_p v_o a_o^3}, \quad \text{(B-14)}$$

which is valid for $\alpha z \ll 1$ for a laser beam of radius a_o with the uniform wind velocity v_o. The term in brackets in Eq. (B-13) can be regarded as a correction factor that modifies N_c to account for finite αz, focusing and a variable wind or

slewing velocity.

The form of the correction factor for focused beam propagation with a uniform wind velocity is derived first. Thus, taking $g(z) = 1$ and assuming the linear beam profile

$$f(z) = \frac{a(z)}{a_o} = 1 - \left(1 - \frac{a_f}{a_o}\right) \frac{z}{z_f} \quad , \tag{B-15}$$

where $a_f = a(z_f)$ is the beam radius at the focal range z_f, and also assuming $\alpha z \ll 1$, the evaluation of Eq. (B-13) is straight forward and yields the result

$$N = N_c \left(\frac{a_o}{a_f}\right) q \quad , \tag{B-16}$$

with N_c evaluated for $z = z_f$ and

$$q = \frac{2x}{x-1} \left[1 - \frac{\ell n\, x}{x-1}\right] \quad , \tag{B-17}$$

where $x = a_o/a_f$. The focused beam N in Eq. (B-16) differs from the incorrect expression derived previously (Ref. 1, Eq. (17)) only by the factor q which is plotted as a function of a_o/a_f in Fig. B-1. For the case $a_o/a_f < 1$, the beam is diverging while for $a_o/a_f > 1$, the beam focuses. In the limit of very strong focussing, i.e., $a_o/a_f \to \infty$, the factor q approaches 2 and hence $N \to 2 N_c (a_o/a_f)$.

Next, the case of slewing is considered for a collimated beam (i.e., for $f(z) = 1$) with $\alpha z \ll 1$. For this situation the velocity can be written

$$v(z) = v_o + \Omega z \quad , \tag{B-18}$$

where, as shown in Fig. B-2, the slewing rate is

$$\Omega = (v_f - v_o)/z_f \quad , \tag{B-19}$$

and $v_f = v(z_f)$. From Eqs. B-7 and B-18 we have that

$$\tau(z) = 1 + \frac{\Omega}{v_o} z \quad , \tag{B-20}$$

and thus Eq. B-13 (with z replaced by z_f) becomes

$$N_e = N_c \left\{ \frac{2}{z_f^2} \int_o^{z_f} \int_o^{z} \frac{dz'dz}{\left(1 + \frac{\alpha}{v_o} z'\right)} \right\} . \tag{B-21}$$

The evaluation of the integrals is straight forward giving the result

$$N_e = N_c \frac{2}{(x-1)^2} [x \ln x - (x-1)] \quad , \tag{B-22}$$

where $x = v_f/v_o$ is the ratio of the final to initial velocities. The ratio N_e/N_c (with $N_c = N(v_o)$) is plotted in Fig B-3 as a function of v_f/v_o. Thus, with $v_f = 10\ v_o$, the effective distortion parameter N_e is ~ 0.35 times the value associated with the initial velocity, v_o. For some situations it may be more convenient to express N_e in terms of $N_{\frac{1}{2}} = N(v_{\frac{1}{2}})$, where $v_{\frac{1}{2}}$ is the velocity at $z_f/2$. In this case we can obtain from Eq. B-22 the expression

$$N_e/N_{\frac{1}{2}} = \frac{x+1}{(x-1)^2} [x \ln x - (x-1)] \quad , \tag{B-23}$$

which is plotted in Fig B-4 as a function of $x = v_f/v_o$.

FIG. B-1

CORRECTION FACTOR FOR FOCUSED OR DIVERGING BEAM N

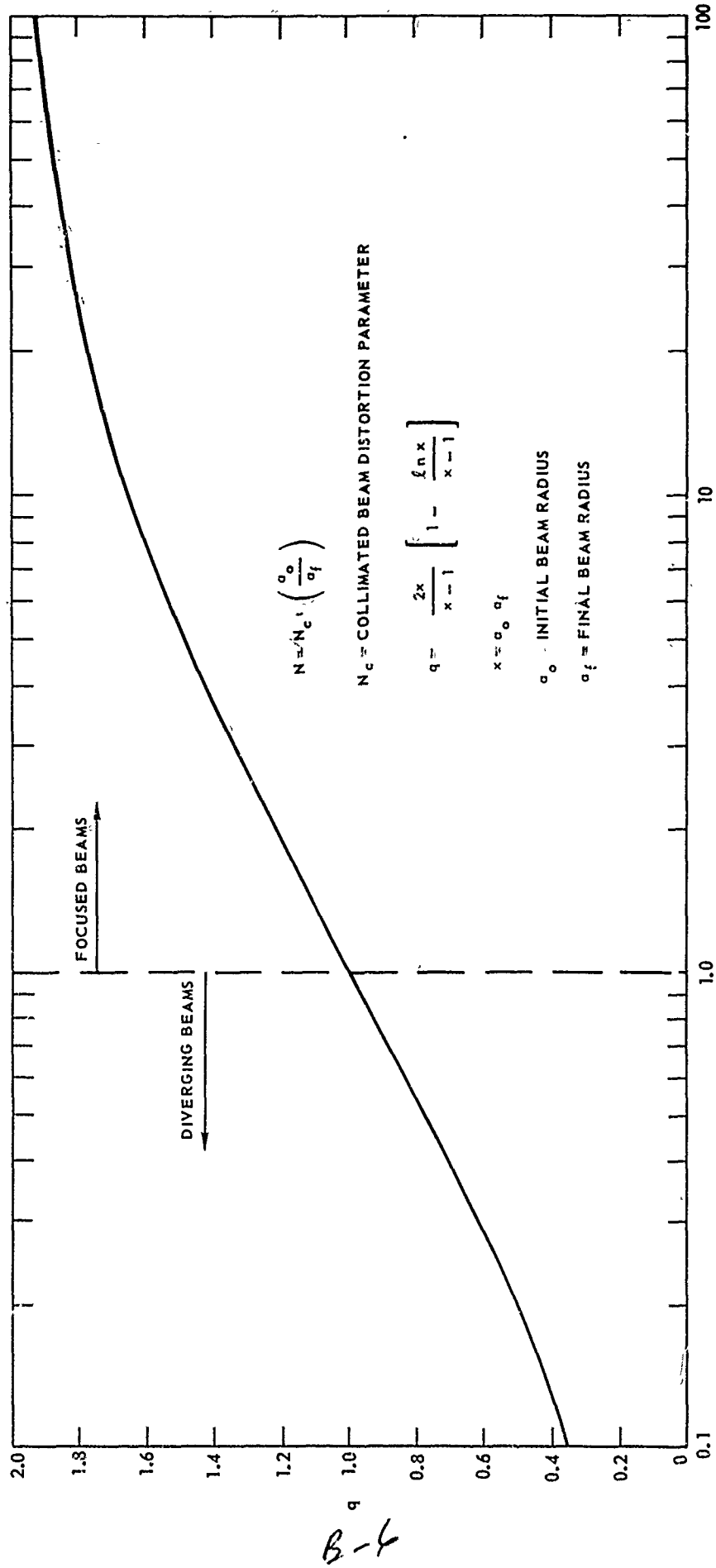

B-4

BEAM SLEWING EFFECT ON DISTORTION PARAMETER

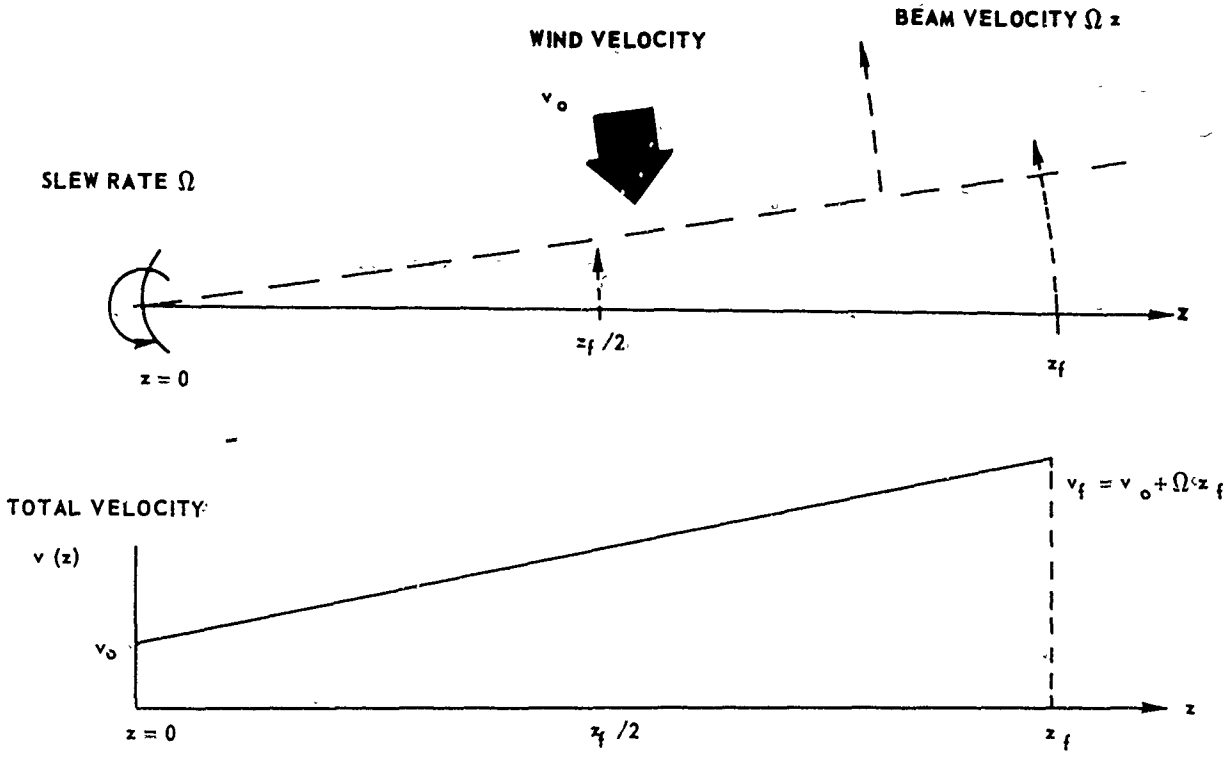

EFFECTIVE DISTORTION PARAMETER – COLLIMATED BEAM:

$$N_e \approx N(v_o) \left(\frac{2 v_o}{z_f^2}\right) \int_0^{z_f} \int_0^{z} \frac{dz'\, dz}{v(z')} \quad ; \alpha\, z_f << 1$$

$N(v_o)$ = DISTORTION PARAMETER FOR UNIFORM VELOCITY v_o

FOR SLEW RATE $\Omega = (v_f - v_o)/z_f$:

$$N_e/N(v_o) = \frac{2}{(x-1)^2} \left[x \ln x - (x-1) \right] \quad ; x = \frac{v_f}{v_o}$$

FIG. B-3

BEAM SLEWING EFFECT ON DISTORTION PARAMETER

COLLIMATED BEAM

$\alpha z_f \ll 1$

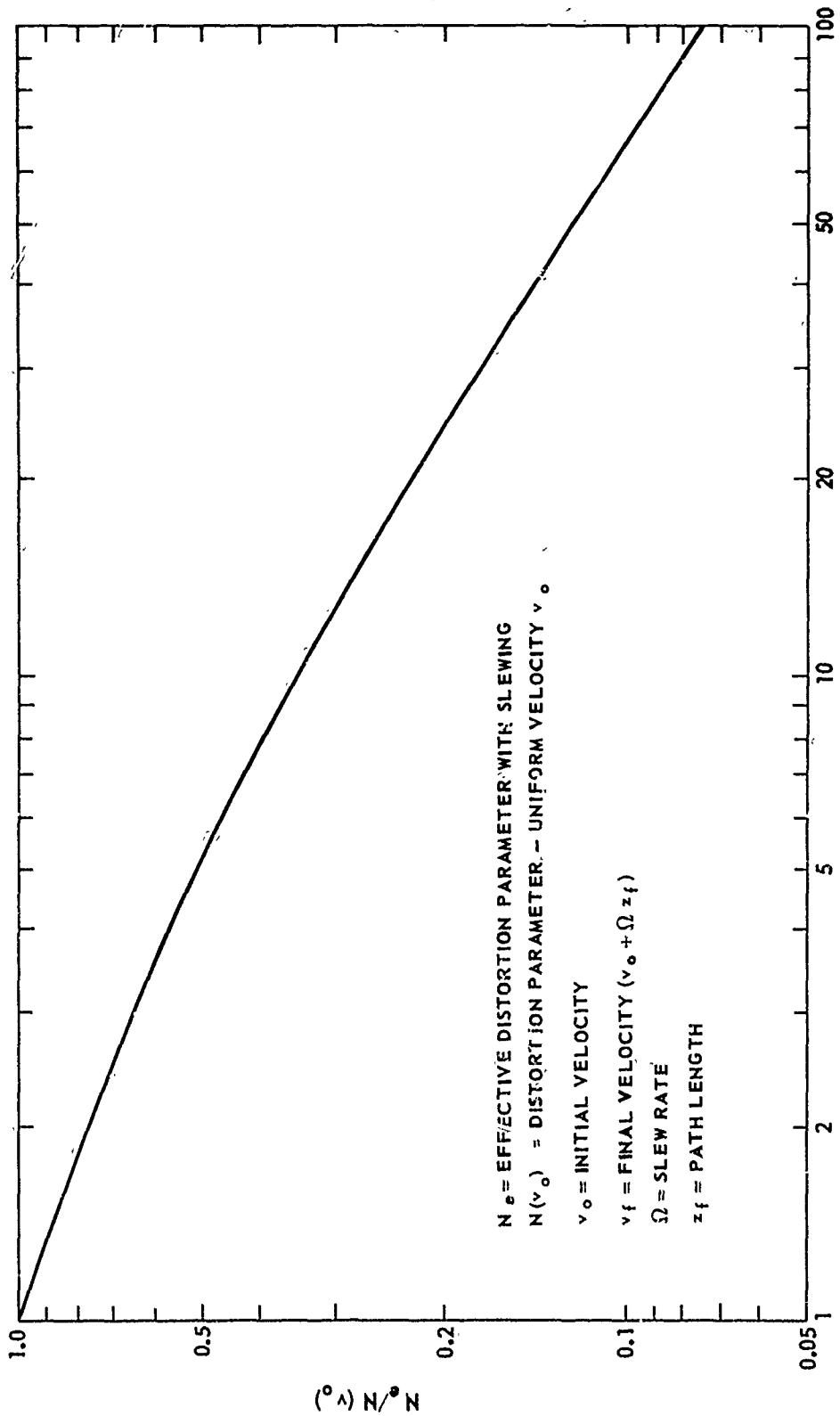

FIG. B-4

BEAM SLEWING EFFECT ON DISTORTION PARAMETER

COLLIMATED BEAM

$\alpha z_f << 1$

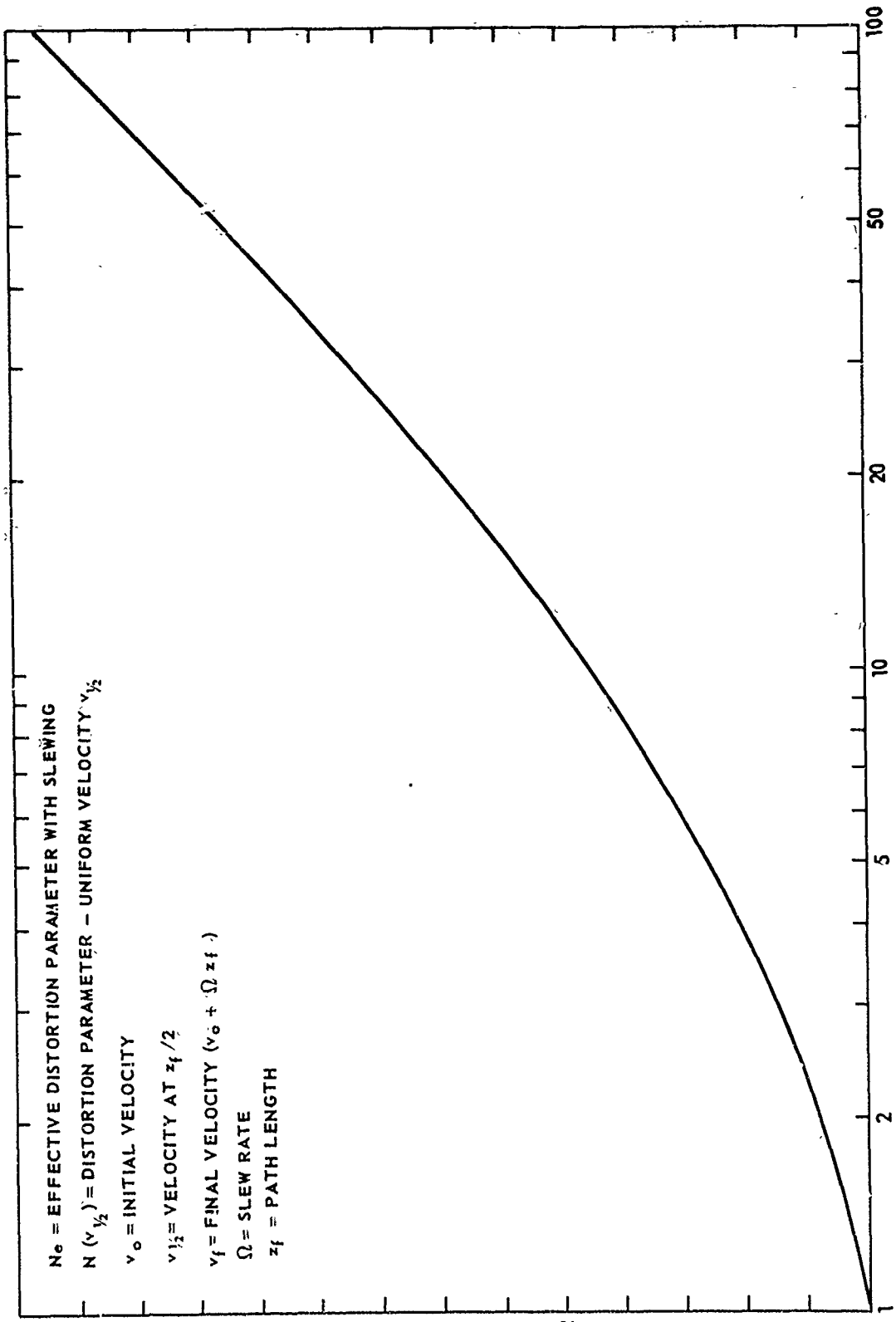

APPENDIX C

Influence of Mirror Aberration on the Thermal Blooming in a Wind

by

Frederick G. Gebhardt
United Aircraft Research Laboratories
East Hartford, Connecticut 06108

December 13, 1971

E921004-8

Influence of Mirror Aberration on the Thermal Blooming in a Wind

by

Frederick G. Gebhardt
United Aircraft Research Laboratories
East Hartford, Connecticut 06108

ABSTRACT

Experiments comparing the thermal distortion effects of wind for laser beams with and without astigmatism are described. The astigmatism, which is obtained by using a spherical mirror at a 45° angle of incidence, produces significant ellipticity in the undistorted beam that, in addition, varies continuously along the propagation path. The results obtained with the aberrated beam show an ~20% higher maximum peak intensity as a function of laser power than the unaberrated beam.

L921004-8

Influence of Mirror Aberration on the Thermal Blooming in a Wind

by

Frederick G. Gebhardt
United Aircraft Research Laboratories
East Hartford, Connecticut 06108

A high power cw CO_2 laser beam propagating in the atmosphere can be severely bent, distorted, and spread by the self-induced thermal lens effects of a transverse wind. Thus, it is of interest to examine techniques for reducing or minimizing the deleterious effects of thermal blooming on the propagation of CO_2 laser radiation in the atmosphere. One approach to this problem is to look for source distributions for the laser transmitter which experience less beam degradation than say, the focused gaussian source. For example, numerical calculations have shown that the form of the initial intensity profile has a significant effect on the details of the thermal distortion of the laser beam.(1) The use of a specially contoured mirror to modify the source wave front shape is also being considered as a possible way of reducing thermal blooming effects.(2) In this report we describe an experiment in which the effect of a mirror aberration on the thermal distortion by a wind is investigated. The astigmatism of a tilted spherical mirror was used as a simple means for modifying the source wave front shape. The objective of the experiment was simply to determine if the astigmatic phase distortion can provide any reduction in the thermal distortion effects over the unaberrated beam case.

Description of Experiment

The thermal distortion effects of wind were examined experimentally by propagating CO_2 laser radiation through liquid CS_2. The CO_2 laser beam was directed downward through a 5 cm-diameter by 12.7 cm-length glass cell containing CS_2 and equipped with NaCl wondows at each end. The liquid cell was moved across the beam with a mechanical scanner at the velocity of 1 cm/sec to simulate the effect of a wind. The laser beam was focused on the detector, which was situated near the cell exit window, with a spherical copper mirror of 68 cm radius of curvature. As shown in Fig. 1, the plane of incidence (defined by the incident laser beam and the normal to the mirror) is perpendicular to the direction of motion of the liquid cell. As the angle of incidence Φ, between the laser beam and the normal to the mirror increases from zero, the aberration known as astigmatism increases in strength.[3] For $\Phi = 8^{\circ}$, the astigmatism is negligibly small for our purposes, and we refer to this as the unaberrated case. For the aberrated case, as shown in Fig. 1, $\Phi = 45^{\circ}$, which results in a significant amount of astigmatism.

To insure that differences observed in the thermal distortion between the aberrated and unaberrated cases could be attributed solely to the astigmatism, special care was taken to keep the distance between the laser output mirror and the curved focusing mirror the same for each case. The 18 cm distance between the curved mirror and the liquid cell was needed to allow clearance between the laser beam and cell for the small (8°) angle of incidence for the unaberrated case.

The cross hatched patterns shown in Fig. 1 represent the undistorted laser beam shapes at the planes indicated. These were determined from measured intensity profiles (Figs. 3 and 4) and photographs of the beam taken with Kalvar film (See Ref. 1, p. 36). For the unaberrated case, the laser beam is circular and focuses slightly through the moving liquid cell. For the aberrated case, on the other hand, the astigmatism produces a pronounced ellipticity in the laser beam shape at the cell entrance. The major axis of the elliptical pattern is parallel with the cell motion simulating the wind. As the beam propagates from the cell entrance to the detector the beam shape becomes circular and the diameter is approximately equal to the mean diameter of the elliptical input beam. The effect of astigmatism is to focus rays lying in the plane of incidence at the distance $(r \cos \phi)/2$ (known as the tangential focus), while rays lying in the plane normal to this are focused at the distance $r/(2 \cos \phi)$ (the saggital focus), where r is the mirror radius of curvature.[3] The observed beam patterns are consistent with this since for $\phi = 45^{\circ}$, the minimum beam dimension transverse to the wind should occur at the tangential focus, which is approximately midway through the cell. Beyond the detector, which is located nearly at the "circle of least confusion," the beam again becomes elliptical but with the major axis normal to the cell motion. The maximum ellipticity with this orientation should occur about 13.5 cm beyond the detector, at the saggital focus.

Experimental data for the thermal distortion for both the aberrated and unaberrated beams were obtained by measuring the intensity profiles through beam center along the "wind" direction. This was accomplished by scanning the detector across the beam along with the liquid cell. The detector was equipped

with a 50μ pin hole aperture and has been described in Ref. 1. The pertinent experimental parameters are summarized in Table I for both the aberrated and unaberrated beam cases.

Experimental Results

Images of the thermally distorted laser beam patterns were obtained using Kalvar film and are shown in Fig. 2 for input powers varying from 0.5 to 7.0 W. The "wind" direction is from right-to-left and the relative beam deflections can be measured from the right edges of the pieces of film. The most striking feature of the distortion obtained with the aberrated beam is the narrow width and small curvature of the patterns as compared with the unaberrated case.

The measured intensity profiles for the unaberrated and aberrated beams are shown in Figs. 3 and 4, respectively. The "input beam" profile refers to the beam at the cell entrance and the remaining profiles were measured ~3 cm from the cell exit window. The various profiles are labeled with both the input laser beam power, P, as well as the value of N, which is evaluated using the relation:

$$N = \frac{(-dn/dT)2Pz}{n_o \rho c_p v a_i^3} \left(\frac{a_i}{b_i}\right) \left(\frac{a_i}{a_o}\right) \left[1 - \frac{(1 - e^{-\alpha t})}{\alpha t}\right] , \qquad (1)$$

where n_o, dn/dT, ρ, c_p, α and v are, respectively, the refractive index, the index change with respect to temperature, density, specific heat, absorption coefficient and velocity of the medium. The remaining quantities are defined in Table I where the material properties of CS_2 are also included. The factors a_i/b_i and a_i/a_o are included to account for the ellipticity and focusing of the beams, respectively.(1)

The case N = 0, in Figs. 3 and 4, corresponds to the undistorted profile obtained without the absorbing liquid cell in place. Two scans of each of the distorted patterns are shown in Figs. 3 and 4 and the repeatability of the data is clearly evident. Comparison of the data for the aberrated beam with the unaberrated case shows that the detailed structure in the distorted patterns is very similar. It should be pointed out that the anomalously small profile for N = 1.2 with the unaberrated beam (Fig. 3) is probably due to error in alignment of the detector with the center of the beam. As the distortion effects, or equivalently, the values of N, become larger, the large thermally induced beam spreading transverse to the wind (c.f., Fig. 2) tends to make this slight misalignment unimportant as indicated by the remaining results in Fig. 3.

Data for the peak intensity of the distorted patterns have been taken from the profiles in Figs. 3 and 4, and are shown in Fig. 5 as functions of the laser power. The dashed lines indicate the peak intensity dependence upon power for the linear propagation case, i.e., in the absence of any thermal distortion. Note that the linear attenuation has been included in these curves so that they are readily compared with the values for the distorted peak intensity. The different slopes of the two dashed lines simply reflect the fact that the spot at the detector is larger for the aberrated beam than for the beam with no aberration (c.f., Figs. 1, 3 and 4). With thermal distortion, the peak intensity increases with power until the beam spreading due to blooming begins to increase in proportion to the power. The peaks of the solid curves in Fig. 5 correspond to this condition. For larger power levels the increase in thermally induced beam spreading with power becomes dominant and the peak intensity decreases

monotonically. Except for very low power levels, where the thermal lens effects are weak, the aberrated beam peak intensity is greater than for the unaberrated case. In particular, the maximum peak intensity achieved by the aberrated beam is ~20% greater than that for the unaberrated beam and, in addition, this maximum occurs at one-half the power. Thus, according to Fig. 5, there is a range of power levels, or equivalently, values of N, for which the aberrated beam provides a greater peak intensity at the target than the beam with no aberration.

In Fig. 6, the relative peak intensities (i.e., the peak intensity normalized by the undistorted value) are plotted versus N. This shows the advantage of the aberrated beam over the unaberrated beam in terms of the amount of distortion relative to the respective undistorted beams. The low data point for the unaberrated beam at N = 1.2 is believed to be due to the detector misalignment; and, as noted earlier, the alignment error becomes less important with increasing values of N.

The normalized beam deflection dependence on N is shown in Fig. 7. Again, the aberrated beam is somewhat less affected by the thermal distortion than the unaberrated beam. The reduced deflection and spreading of the aberrated beam as indicated by Figs. 5, 6 and 7 is clearly consistent with the distorted beam patterns shown in Fig. 2. It is perhaps worthwhile to point out that the use of the parameter N, for characterizing the thermal distortion of the aberrated beam, is not particularly helpful if comparison is to be made with a significantly different type of beam, e.g., the unaberrated beam. In this instance it is more convenient to make the comparison on an absolute basis as

done, for example, in Fig. 5. The use of N in presenting the thermal distortion results in Figs. 6 and 7 indeed shows that the distortion effects for the aberrated and unaberrated beams do not depend on N (as defined in Eq. (1)) in a universal way.

Although the aberrated beam offers some relief from thermal blooming effects in these experiments it is not clear to what extent the elliptical beam shape associated with the astigmatism is responsible. Referring to earlier work with a collimated elliptical gaussian beam (ignoring diffraction effects) one expects a greater amount of transverse beam spreading if $b_i/a_i < 1$, as in the present case.[4] This is consistent with the nearly straight aberrated beam patterns (c.f., Fig. 2) as compared with the more curved crescent patterns of the unaberrated beam. With $b_i/a_i \ll 1$ it is also predicted, however, that the intensity reduction and beam deflection is increased over that of a circular beam of radius a_i with the same power. This appears to be inconsistent with the present results. No doubt diffraction effects (because of the small Fresnel numbers involved) and the complicated combination of beam ellipticity and the aberrated wave front are all important here in the thermal distortion process.

Summary

Experiments comparing the thermal distortion effects of wind for laser beams with and without astigmatism have been described. The astigmatic beam was obtained by use of a spherical mirror at an angle of incidence of 45°. The astigmatic mirror aberration produces significant ellipticity in the undistorted beam which, in addition, is continuously varying along the propagation

path. Although the aberrated beam showed an ~20% higher maximum peak intensity as a function of laser power than the unaberrated beam, the results are difficult to analyze or explain. Without a better understanding of the mechanism by which the astigmatism modifies the thermal lens effects, it is difficult to draw any firm conclusions of a general nature from these experiments. If further experiments along this line are to be carried out, it is recommended that a simpler situation be considered together with the support of an analytical effort.

Helpful discussions with Dr. D. C. Smith and the assistance of Mr. A. Guardiani with the experiments are gratefully acknowledged.

References

1. F. G. Gebhardt and D. C. Smith, "Investigation of Self-Induced Thermal Effects of CO_2 Laser Radiation Propagating in Absorbing Gases," UARL Report K921004-4, July 1971.

2. G. H. McLafferty, private communication.

3. F. A. Jenkins and H. E. White, Fundamentals of Optics, (McGraw-Hill, New York, 1957), p. 94.

4. See Reference 1, Section 3.4.

TABLE I

EXPERIMENTAL PARAMETERS

Cell length t = 12.7 cm
Total path length z = 16 cm (cell input to detector)
Velocity v = 1 cm/sec
αt = 2.2
Cell transmission T = 0.1 (includes ~10% NaCl window reflection loss)
CS_2 Properties: $dn/dT = -0.79 \times 10^{-3}\ ^{\circ}C^{-1}$; $n_o = 1.63$;
$\rho = 1.26\ g/cm^3$; $c_p = 0.95\ J/g^{\circ}C$

	UNABERRATED BEAM	ABERRATED BEAM
* a_i, mm	0.67	0.86
b_i, mm	0.67	0.38
a_o, mm	0.44	0.67
**$F = k_e a_i^2/z$	2.5	4.1
N/P, W^{-1}	12.2	10.9

* a_i = input 1/e beam radius - parallel with wind
b_i = input 1/e beam radius - perpendicular to wind
a_o = output 1/e beam radius

**$k_e = (2\pi/\lambda z) \int_0^z n(z')dz'$ - effective propagation constant

ABERRATED BEAM EXPERIMENT

M - MIRROR, 68cm RADIUS

C - MOVING CS_2 CELL

D - DETECTOR

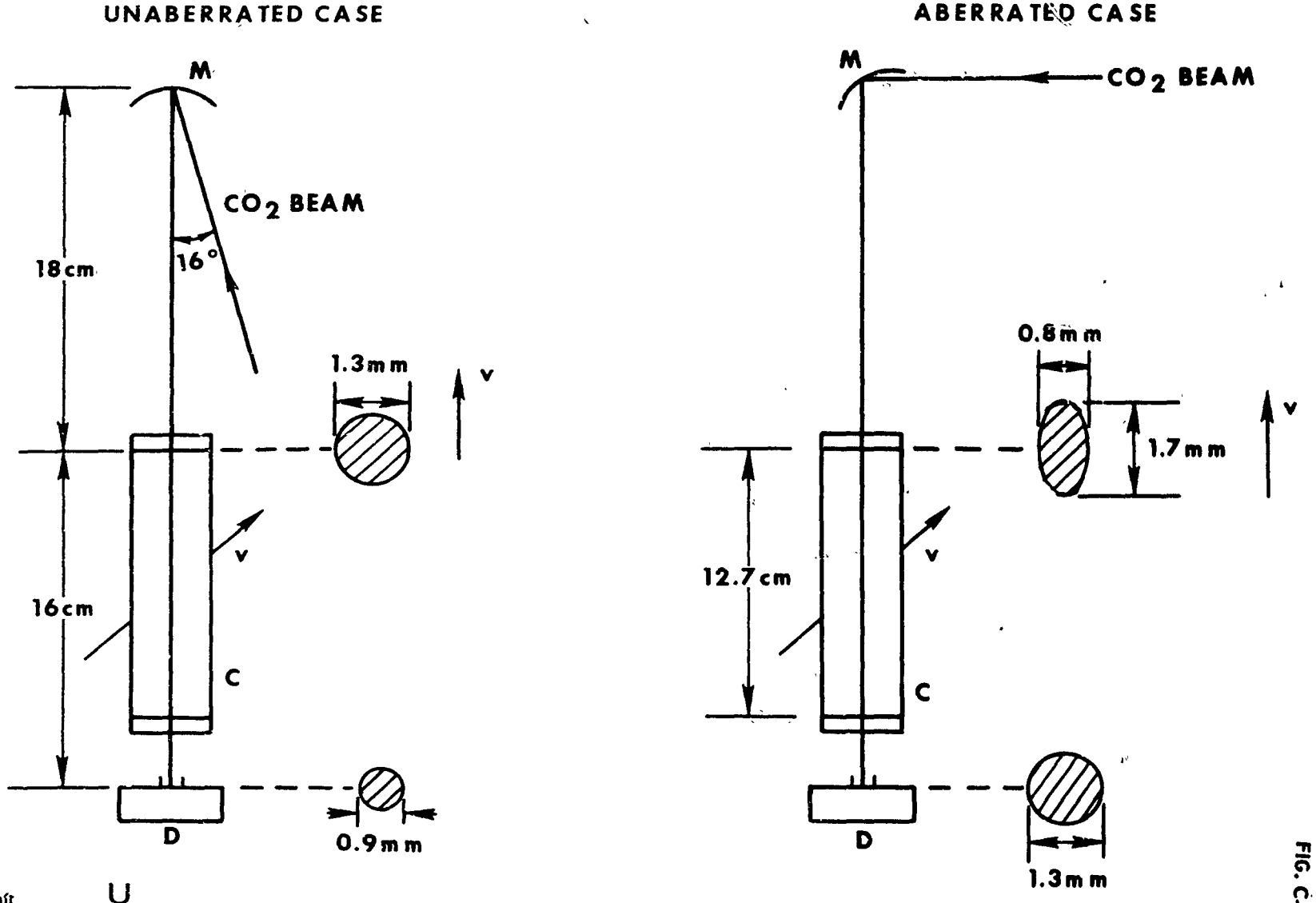

United Aircraft Research Laboratories

L921004-8

FIG. C-1

C-14

COMPARISON OF THERMALLY DISTORTED BEAM PATTERNS WITH AND WITHOUT MIRROR ABERRATION

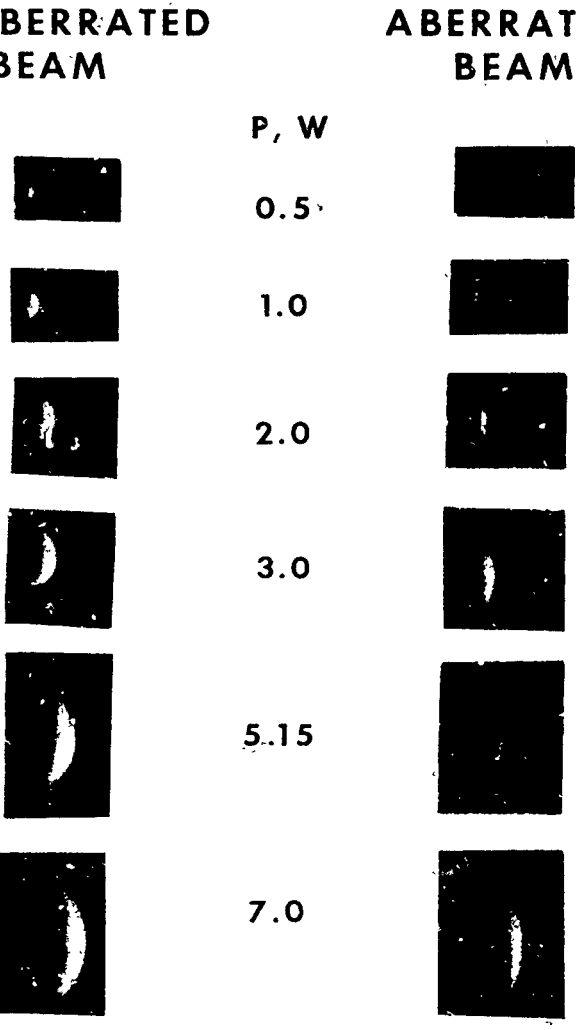

L921004-8

C-13

FIG. C-2

FIG. C- 3

MEASURED INTENSITY PROFILES: UNABERRATED BEAM

HORIZONTAL SCALE = 1.9mm/div

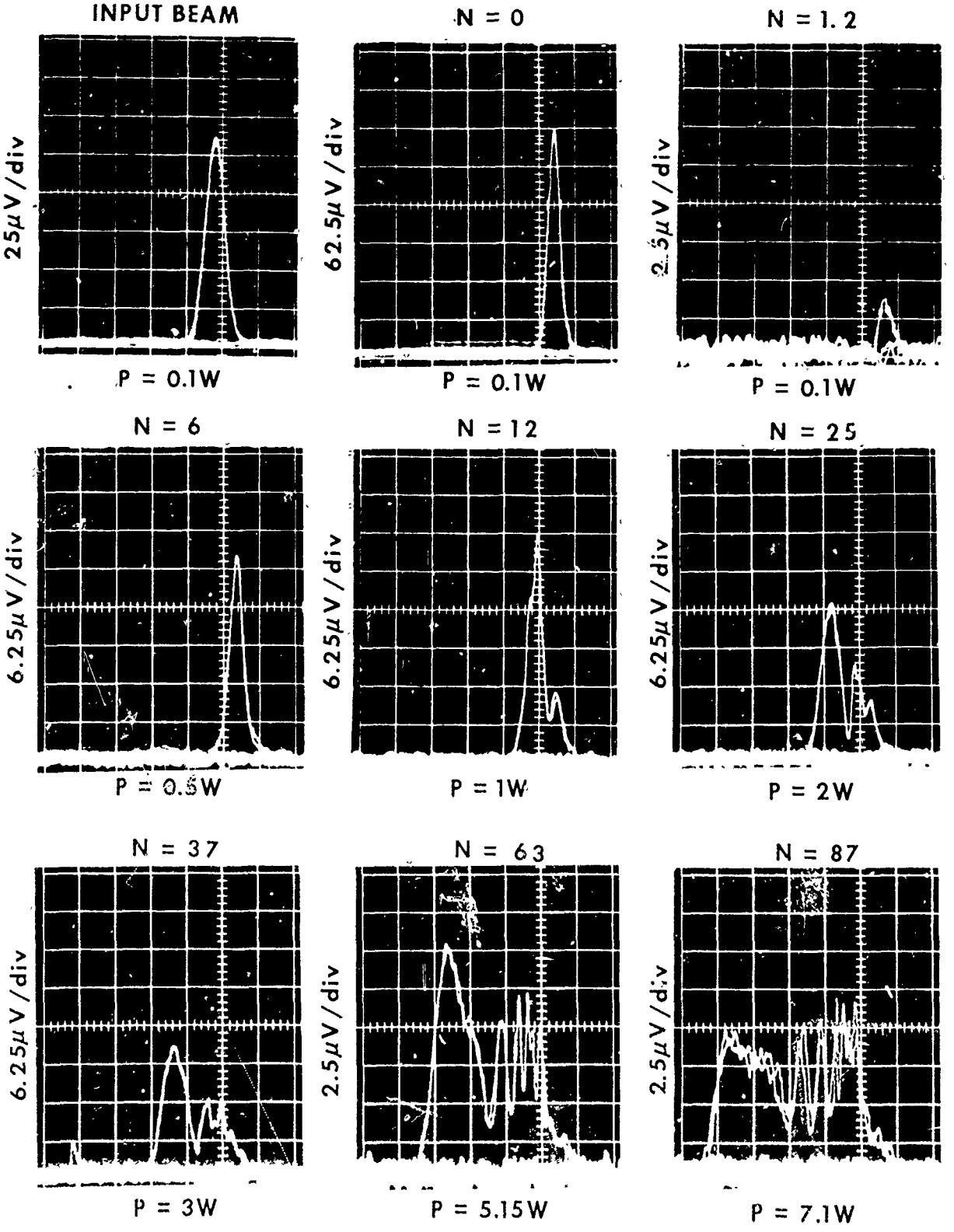

FIG. C- 4

MEASURED INTENSITY PROFILES: ABERRATED BEAM

HORIZONTAL SCALE = 1.9mm/div

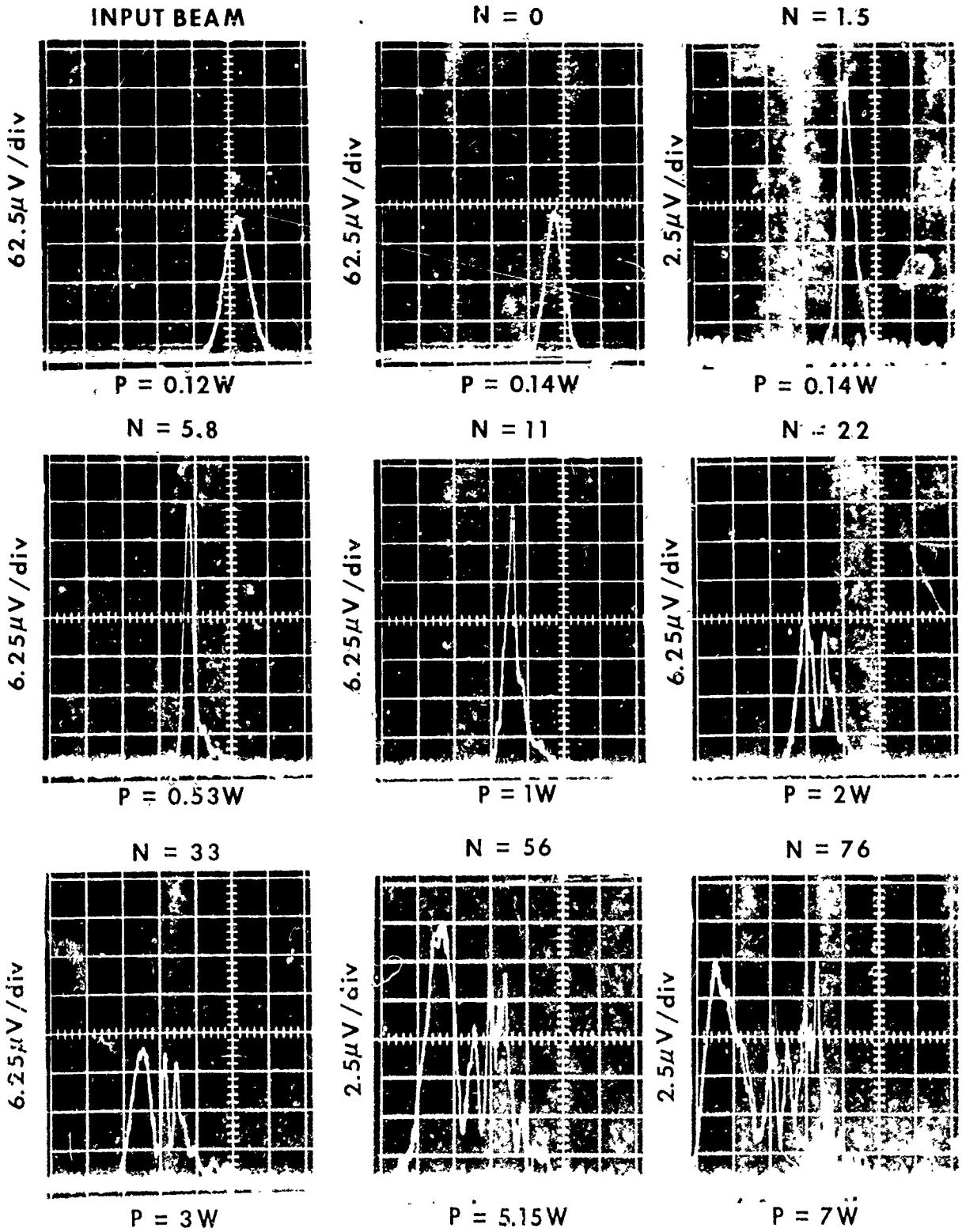

PEAK INTENSITY VERSUS LASER BEAM POWER

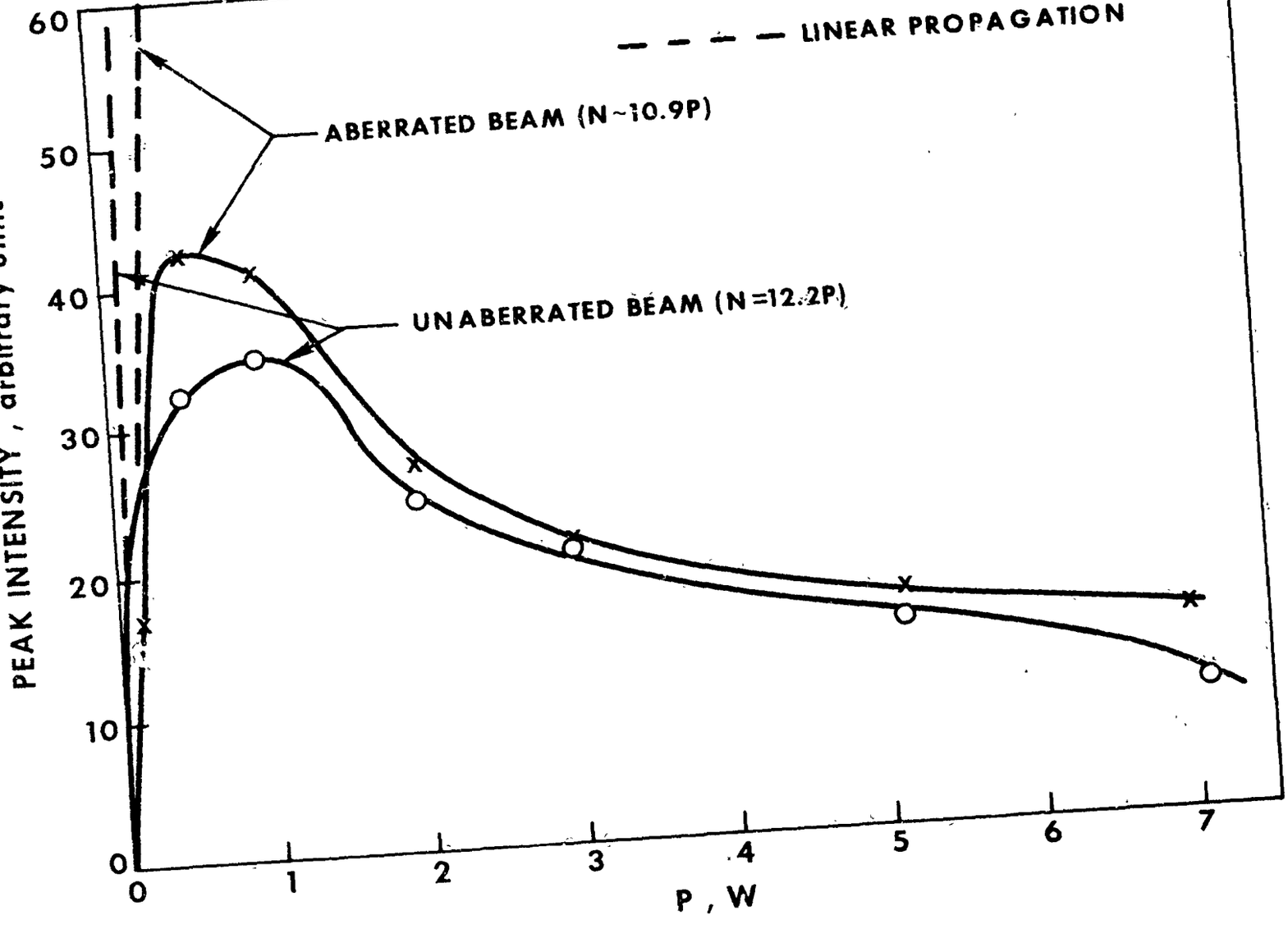

L921004-8

FIG. C-5

United Aircraft Research Laboratories

FIG. C-6

DEPENDENCE OF RELATIVE PEAK INTENSITY ON N

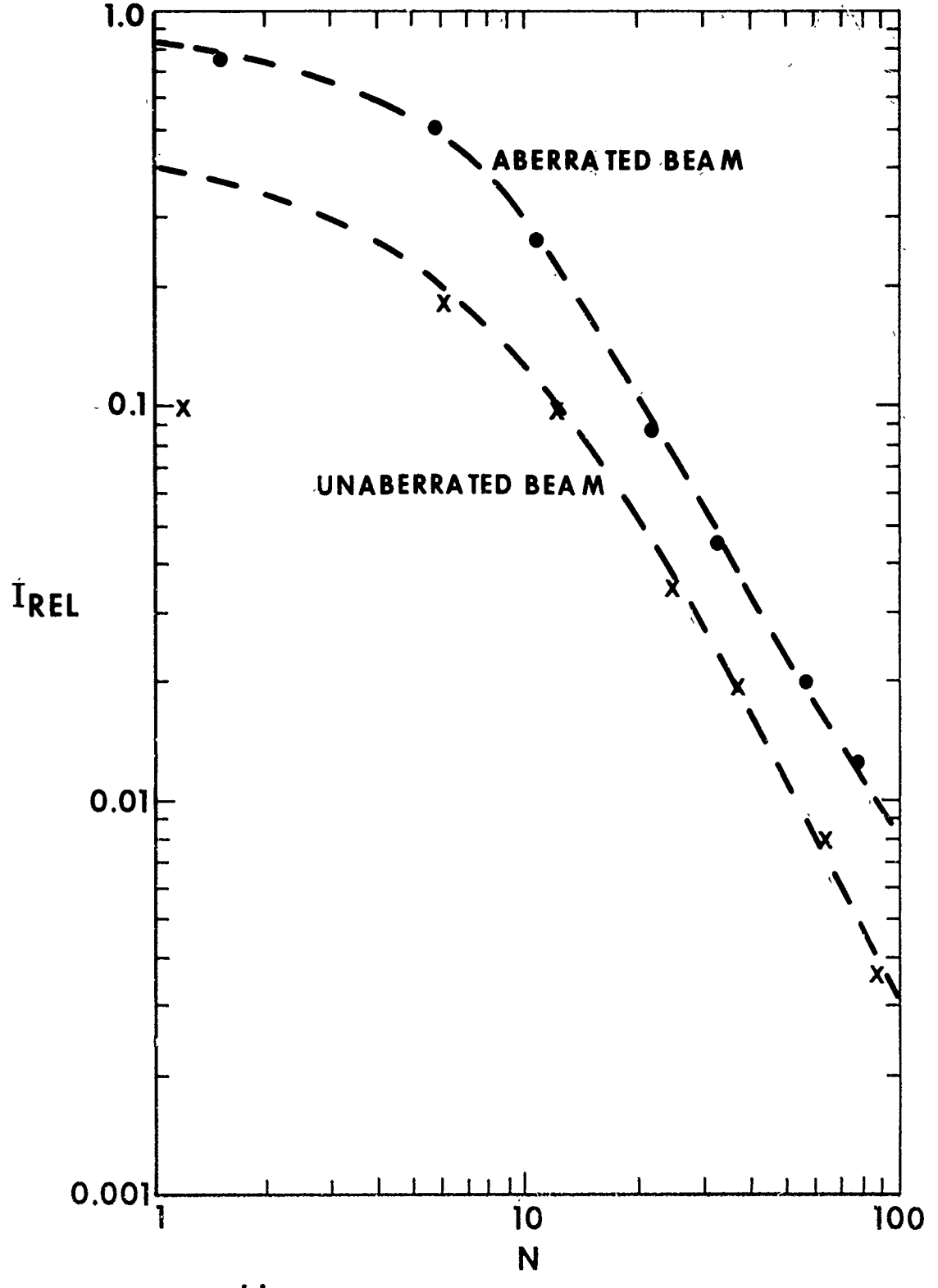

L921004-8

FIG. C-7

DEPENDENCE OF NORMALIZED BEAM DEFLECTION ON N

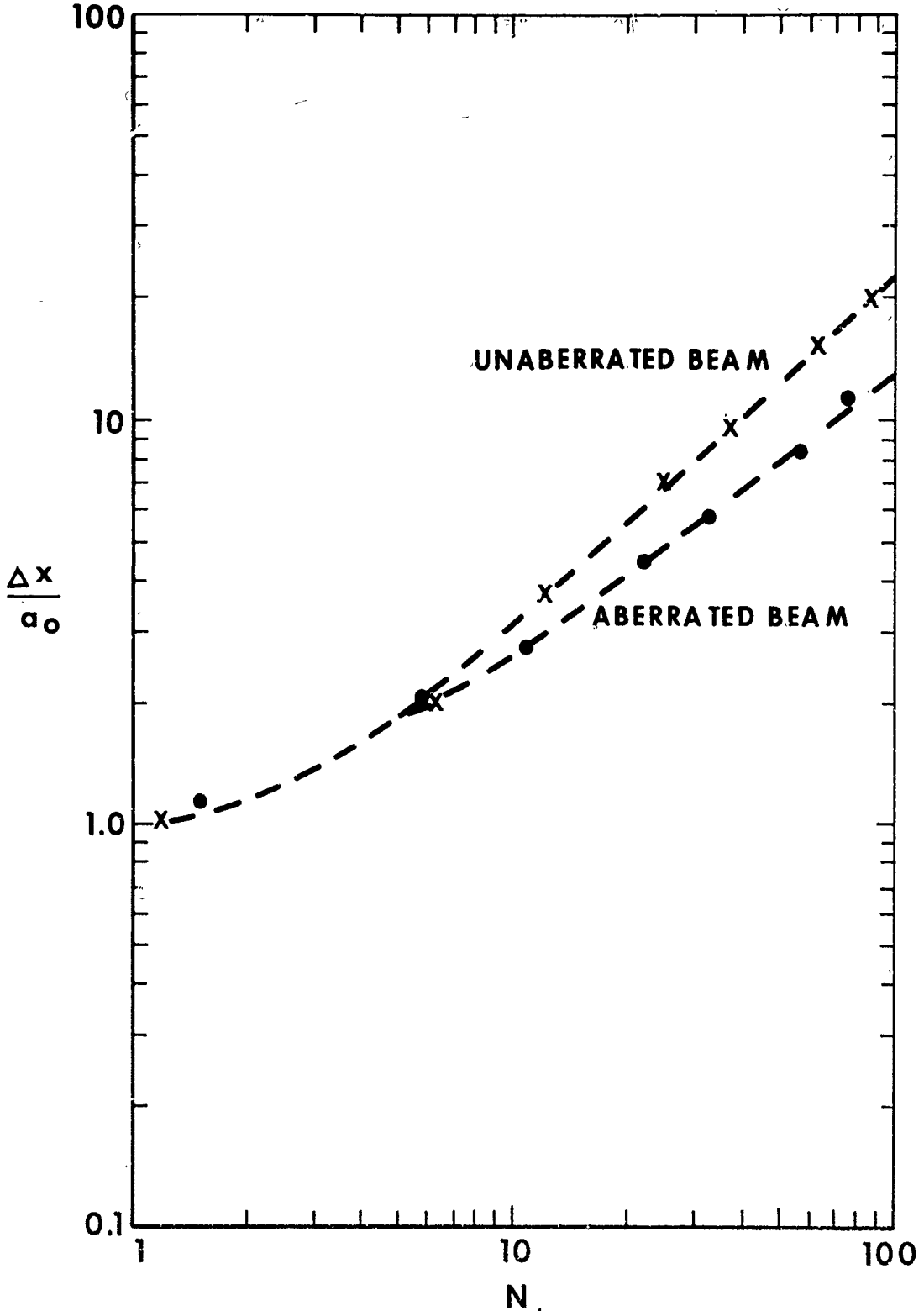

APPENDIX D

Kinetic Cooling of a Gas By Absorption of CO_2 Laser Radiation

by

Frederick G. Gebhardt and David C. Smith
United Aircraft Research Laboratories
East Hartford, Connecticut 06108

October 11, 1971

L921004-8

Kinetic Cooling of a Gas by Absorption of CO_2 Laser Radiation

Frederick G. Gebhardt and David C. Smith
United Aircraft Research Laboratories, East Hartford, Connecticut 06108
(Received 11 October 1971)

The effect of kinetic cooling due to the absorption of 10.6-μ CO_2 laser radiation in the atmosphere has recently been predicted. In this letter, experimental evidence for this effect is presented. Transient-density increases due to the kinetic cooling have been observed in CO_2-N_2 mixtures following the propagation of an ~1-μsec 0.5-J CO_2 laser pulse through the gas. The experiments were performed with varying concentrations of CO_2 and the observed cooling and subsequent heating effects are explained using the usual three-level approximation for vibrational energy transfer in CO_2-N_2, together with known relaxation rates.

The propagation of high-power CO_2 laser radiation in the atmosphere can lead to various self-induced thermal lens effects which distort or otherwise alter the beam itself.[1-5] These effects are caused by the changes in temperature, and hence, refractive index that result from the absorption of 10.6-μ radiation, by CO_2, and water vapor. The absorption process involves vibrational transitions and the increase in vibrational energy is transferred by collisional relaxation processes to translation causing the gas to eventually be heated. In the case of H_2O, as with many other absorbers, the relaxation processes are so rapid that for all practical purposes the absorbed energy is transferred instantaneously into heat. For CO_2, on the other hand, the relaxation processes are much slower and the possibility of a nonequilibrium cooling of the gas by absorption has been reported.[3,4] With cooling, the gas density and refractive index increase, which tends to focus the laser beam in contrast with the usual defocusing or "blooming" effects due to heating. Although the cooling is distinctly a transient effect and is thus important for pulsed propagation,[4] Wallace and Camac[5] have shown its importance also for cw propagation with a wind or beam slewing.

In this letter, experimental evidence for the kinetic cooling of a gas by the absorption of CO_2 laser radiation is presented. Transient-density increases have been observed in CO_2-N_2 mixtures following the propagation of an ~1-μsec 0.5-J CO_2 laser pulse through the gas. The observed cooling interval and delay in gas heating increase with decreasing CO_2 concentration in accordance with known relaxation rates.

A detailed theoretical treatment of the energy-exchange processes involved with 10.6-μ absorption in air has been presented by Wood, Camac, and Gerry.[4] For the present experiment where gas mixtures of varying concentrations of CO_2 with N_2 have been used rather than natural air, the kinetic model must be changed somewhat from that in Ref. 4, particularly with regard to the rates involved. Also, the use of a pulse width shorter than the important relaxation times alters the effects in the experiment somewhat from the predictions of Ref. 4. In order to discuss the absorption of 10.6-μ radiation and subsequent relaxation processes in a CO_2-N_2 mixture, the familiar three-level approximation for the CO_2 laser[6] in Fig. 1 is convenient. Group (0) is the ground level with no vibrational energy; level (1) includes the bending (v_2) and symmetric stretch (v_1) modes of CO_2 with the lower level (100) of the 10.6-μ transition; and the level (2) includes the first vibrational level of N_2 together with the upper level (001) of the absorbing transition, which is the asymmetric stretch mode (v_3) of CO_2. Within the limits of the three-level approximation the vibrational levels within the individual groups are assumed to be closely coupled by rapid relaxation processes; and, the only important relaxation times are τ_{21} and τ_{10}, which govern the energy transfer between the levels (2)-(1) and (1)-(0), respectively. The absorption of a 10.6-μ CO_2 laser photon [the absorption coefficient for $T = 300\,^{\circ}K$ and 1-atm pressure is $\alpha \approx X_{CO_2}\,(2\times10^{-3})\ cm^{-1}$, where X_{CO_2} is the mole fraction of CO_2 (Ref. 7)] produces a 001 vibrationally excited molecule and eliminates one molecule in the 100 state. The nearly resonant energy transfer between the CO_2 (001) and N_2 ($v = 1$) levels rapidly establishes vibrational equilibrium and the combined energy levels (2) relax through collisions to (1) at the rate τ_{21}^{-1}. Level (1), which has been depleted by the absorption process, is restored to thermodynamic equilibrium either through the ground state (0) at the rate τ_{10}^{-1}, or the

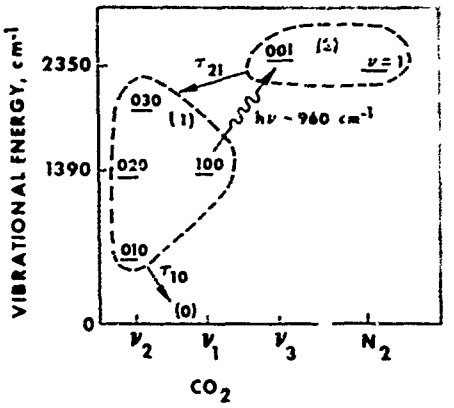

FIG. 1. Simplified vibrational-energy-level diagram showing the three-level approximation for CO_2-N_2 gas mixtures.

deactivation of level (2) at the rate τ_{21}^{-1}, depending on which is faster. With the former process (i.e., $\tau_{10} < \tau_{21}$) vibrational equilibrium is established at the expense of translational energy, and the gas is cooled until level (2) can relax. In the latter case (i.e., $\tau_{21} < \tau_{10}$) no cooling occurs and the gas is heated following the collisional deactivation of levels (2) and (1). In both cases, gas heating due to the absorbed energy occurs on a time scale of $\sim \tau_{21} + \tau_{10}$. The relaxation times τ_{21} and τ_{10} have been calculated using the expressions and rates given in Ref. 6. The results are shown in Fig. 2 as functions of X_{CO_2}, the mole fraction of CO_2, for a pressure of 1 atm. The characteristic heating time $\tau_{21} + \tau_{10}$ is included in Fig. 2 as the broken curve. Decreasing X_{CO_2} or equivalently increasing the N_2 concentration X_{N_2} significantly increases the upper level (2) lifetime τ_{21} while slightly decreasing the lower level (1) lifetime τ_{10}. According to Fig. 2, the kinetic cooling effect should occur for $X_{CO_2} < 0.6$, since under these conditions $\tau_{21} > \tau_{10}$. As X_{CO_2} decreases, the cooling effect becomes more pronounced since τ_{21} increases. The magnitude of the cooling and subsequent heating, however, depends on the absorption coefficient which is proportional to X_{CO_2}. It should be pointed out that the kinetic model used for air in Ref. 4 differs somewhat from the three-level CO_2-N_2 model because of the low (~0.03%) CO_2 concentration and the presence of H_2O and O_2 in air. Although this modifies the various relaxation rates involved, essentially the same vibrational-energy-transfer processes in CO_2 and N_2 are responsible for the cooling effect in both cases. The main difficulty in observing experimentally the cooling effect in normal air is, of course, due to the small absorption coefficient. In addition, while H_2O alters the relaxation rates involved in the cooling process, it also absorbs laser radiation and causes beam-heating effects that compete with the cooling.

The experimental arrangement is shown in Fig. 3. A 1-μsec 0.5-J pulse from an electrically excited CO_2 laser[6] is passed through a gas cell, 12 cm long by 3.8 cm in diameter, containing a mixture of CO_2 and N_2. The gas cell is equipped with NaCl windows and is placed in one arm of a Mach-Zehnder interferometer. A He-Ne laser beam at 6328 Å is expanded by a telescope and used to illuminate the interferometer. A germanium lens L with 25-cm focal length is used to focus the 10.6-μ radiation into the gas cell through an antireflection-coated germanium window W that also serves as a mirror for the visible beam in the interferometer. The density changes in the gas cell that result from the absorption of CO_2 laser radiation are measured with a photodiode placed in the fringe field at the interferometer output. With the interferometer adjusted to produce an infinite fringe, a change in gas density modifies the interferometer intensity and a signal is obtained from the photodiode that is amplified (Tektronix 1121, 5-Hz 17-MHz bandwidth) and displayed on an oscilloscope. The combined photodiode-amplifier rise time is $\lesssim 2$ μsec as measured with a spark gap. Rotation of the optical flat F is used to bias the interferometer for maximum sensitivity and for calibration by establishing the magnitude and direction of the phase change. The CO_2 laser beam was measured from burn patterns on thermofax paper to be ~2 × 5 mm at the cell entrance and exit windows, and the focused spot size midway through the cell was estimated to be ~0.2 mm. The photodiode aperture was 4 mm in diameter.

The experiment consisted essentially of monitoring the density changes in the CO_2-N_2 mixture following the absorption of a portion of the CO_2 laser pulse energy. The experiments were performed with X_{CO_2} varied from 0.05 to 1.0 at a total pressure of 1 atm, and the results

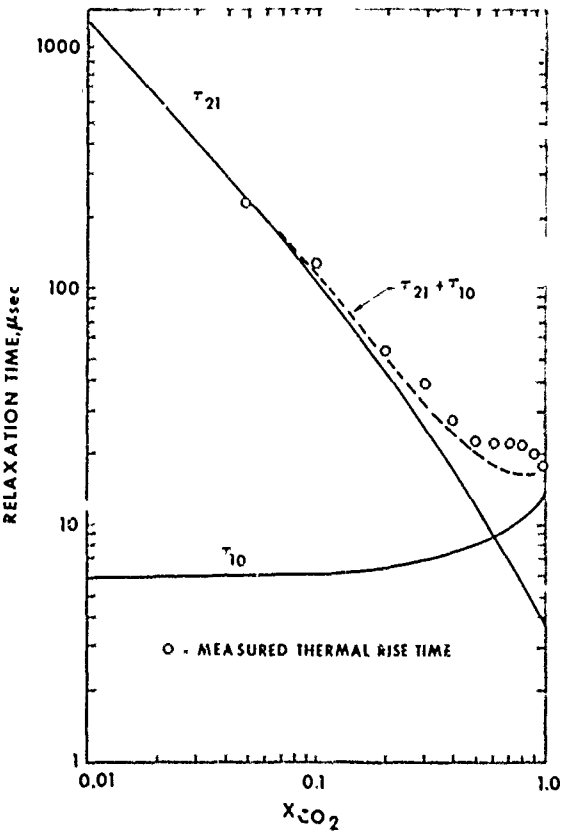

FIG. 2. Relaxation times calculated using data from Ref. 6 for the three-level approximation in CO_2-N_2 mixtures are shown together with experimentally determined thermal rise times.

Appl. Phys. Lett., Vol. 20, No. 3, 1 February 1972

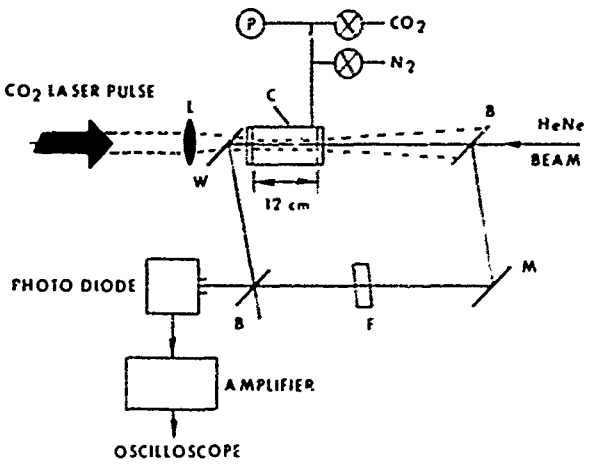

FIG. 3. Experimental arrangement for the interferometric observation of kinetic cooling. L: Ge lens, 25-cm focal length; W: Ge-window Ar coated for 10.6 μ; B: beamsplitter; M: mirror; F: optical flat; C: gas cell, 3.8 cm in diam; P: vacuum gauge.

for $X_{CO_2}=0.1$, 0.2, 0.3, 0.4, 0.6, and 1.0 are shown in Fig. 4. The photodiode signals in Fig. 4 show the normalized density changes with time (horizontal scale = 50 μsec/div), and a density increase corresponding to the cooling effect is observed for the cases where $X_{CO_2}<0.6$ as predicted. For $X_{CO_2}\geq 0.6$, only a density decrease due to heating is observed with essentially no change in the signal as X_{CO_2} is increased. The density change can be expressed in terms of the photodiode-signal voltage since it is small compared with that required to change the optical path length by $\frac{1}{2}\lambda$, as determined by rotating the optical flat F. Thus, the photodiode signal is assumed to be nearly proportional to the interferometer path difference and, hence, the gas density. Since the laser pulses are short compared with the relaxation times shown in Fig. 2, the gas-temperature changes following the laser pulse occur on the same time scale as these vibrational decay processes. The gas-density change, and hence the interferometer signal, on the other hand, are delayed by the acoustic transit time $\tau_a=D/v_s$, where D is the beam diameter and v_s the sound velocity. Following this time the gas-density change with temperature for a constant pressure is observed. Thus, considering the case of pure CO_2 (i.e., $X_{CO_2}=1.0$), the gas heating should occur after $\tau_{21}+\tau_{10}\approx 17$ μsec (see Fig 2), and the acoustic time preceding the gas density change is $\tau_a\approx 13$ μsec, where we have assumed $D=3.5$ mm and $v_s=2.8\times 10^4$ cm/sec for CO_2 at 21 °C. The ~10–15-μsec rise time of the interferometer signal for $X_{CO_2}=1.0$ in Fig. 4 is consistent with this estimate for τ_a. That the rise time is associated with the acoustic time has been established by reducing the pressure to ~0.5 atm and observing only a small change in the signal rise time in spite of the doubling of the relaxation times at the lower pressure. As the CO_2 concentration decreases below 60%, τ_{10} becomes shorter than τ_{21}, and the gas cools after the time $\tau_{10}\sim 6$ μsec. The rise time of the interferometer signal showing the density increase is, of course, delayed by the acoustic transit time. Since the heating time $(\tau_{21}+\tau_{10})$ increases with decreasing X_{CO_2}, becoming much greater than the acoustic transit time, this time eventually dominates the time for the gas density to decrease to the minimum value after the cooling interval. The thermal rise time, which is defined as the time for

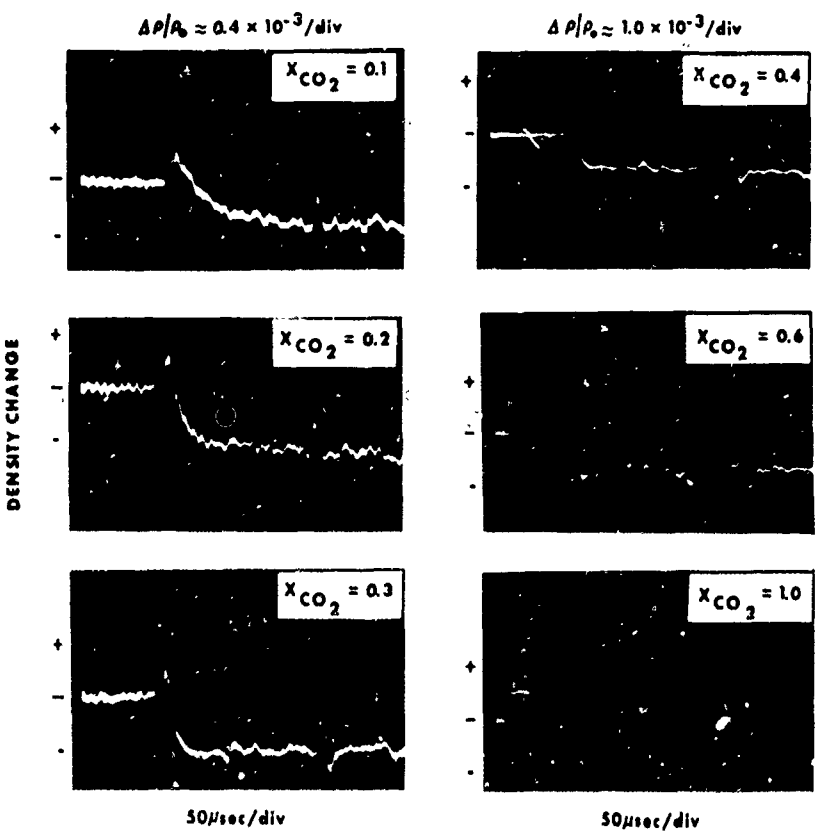

FIG. 4. Photodiode signals showing interferometrically determined density changes in CO_2-N_2 gas mixtures following the propagation of an ~1-μsec 0.5-J CO_2 laser pulse.

the density to reach 90% of the total change from maximum to minimum density, has been measured from the oscilloscope traces and the results are shown in Fig. 2. The beginning of the time interval is taken as the break in the oscilloscope trace which is caused by an electrical noise transient associated with the spark gap used to trigger the CO_2 laser. The measured thermal rise or heating time is seen to be in close agreement with the calculated heating time ($\tau_{21}+\tau_{10}$). It should be pointed out, however, that this agreement is somewhat fortuitous and probably due to the effect of the finite acoustic transit time. For the case where the acoustic time τ_a and τ_{10} become negligible compared with τ_{21}, the so-called thermal rise time should in theory approach $\sim 2\tau_{21}$. Also, in this limit, the density *increase* for very short times ($t \ll \tau_{21}$) should be 1.44 times the density *decrease* for $t \gg \tau_{21}$, which is the ratio of the 100 vibrational energy to the photon energy $h\nu_{10.6}$.

For very long times the decrease in gas density must eventually decay to zero, due to thermal conduction. The thermal-conduction time τ_c of ~50 msec has been measured for pure CO_2, and since $\tau_c = D^2/16\chi$, where $\chi = 0.11$ cm^2/sec is the thermal diffusivity for CO_2, we obtain $D \approx 3$ mm for the effective beam diameter within the gas cell.

It is interesting to note that the density change with $X_{CO_2} = 0.1$ is roughly about one-half that obtained with pure CO_2 rather than one-tenth as expected. This indicates that the CO_2 laser pulse energy density exceeds the saturation value for pure CO_2, and when X_{CO_2} is reduced by adding N_2 the saturation energy density increases to compensate somewhat for the reduction in the absorption coefficient. For a laser pulse shorter than the upper-level relaxation processes, as in the present case, the absorbed energy density under strongly saturated conditions is $\alpha_0 E_s = n_1 h\nu_{10.6}/2$, where n_1 is the number density of CO_2 molecules in the lower absorbing (100) level and α_0 is the unsaturated absorption coefficient. That is to say, E_s is the energy per unit area required for one-half of the (100) CO_2 molecules to be excited by absorption to the (001) level and thus approximately saturate the transition. For pure CO_2 at $T = 300$ °K and 1-atm pressure with $\alpha_0 = 2\times10^{-3}$ cm^{-1} and $n_1 = 7.25\times10^{16}$ cm^{-3}, we obtain for E_s the value 0.34 J/cm^2. The laser pulse energy of 0.5 J together with the beam radius of 1.5 mm (based on the measured thermal-conduction signal decay) gives ~7 J/cm^2, which clearly exceeds the estimated saturation energy density.

The observed density decrease in Fig. 4 for pure CO_2 corresponds to a temperature rise of $\Delta T \sim 0.5$ °C. Assuming saturated conditions and using the energy equation, we find that $E_s \approx 0.38$ J/cm^2 for pure CO_2, which is in good agreement with the calculated value.

It should also be noted that the small pulses appearing in the interferometer signals in Fig. 4 are associated with repeated reflections of the acoustic wave from the walls of the gas cell. Their occurrence in pure CO_2 at intervals of ~125 μsec after the initial density change corresponds well with the 3.8-cm tube diameter. For the case of $X_{CO_2} = 0.1$, the pulse interval is reduced to about 100 μsec, which can be explained by the increase in sound velocity to $v_s \approx 3.4\times10^4$ cm/sec due to the addition of N_2.

In summary, these results have shown the first experimental evidence of kinetic cooling by absorption of laser radiation. The cooling and subsequent heating occur on the time scale of known vibrational relaxation rates, and the simple three-level model for the CO_2-N_2 system appears to be adequate for modeling the effect. In the case of atmospheric propagation, the times associated with the cooling will be increased to milliseconds or greater because of the longer lifetime, τ_{21} associated with the lower CO_2 concentration. The kinetic cooling can be a beneficial effect for propagating pulsed beams which have a pulse width comparable to τ_{21}, or for cw beams propagating with a cross wind such that the transit time across the beam is comparable to τ_{21}.

The authors gratefully acknowledge helpful discussions with Dr. J.J. Hinchen and Dr. M.A. Kovacs and the technical assistance of A. Guardiani. This research was supported in part by the United States Army Electronics Command, Institute for Exploratory Research, Fort Monmouth, N. J. 07703.

[1]D.C. Smith, IEEE J. Quantum Electron. QE-5, 600 (1969).
[2]F.G. Gebhardt and D.C. Smith, IEEE J. Quantum Electron. QE-7, 63 (1971).
[3]A.J. Glass, Opto-Electron. 1, 174 (1969).
[4]A.D. Wood, M. Camac, and E.T. Gerry, Appl. Opt. 10, 1877 (1971).
[5]J. Wallace and M. Camac, J. Opt. Soc. Am. 60, 1587 (1970).
[6]C. Bradley Moore, R.E. Wood, B.L. Hu, and J.T. Yardley, J. Chem. Phys. 46, 4222 (1967).
[7]T.K. McCubbin and T.R. Mooney, J. Quant. Spectrosy. Radiative Transfer 8, 1255 (1968).
[8]D.C. Smith and A.J. DeMaria, J. Appl. Phys. 41, 5212 (1970).

APPENDIX E

Comparison of Numerical and Experimental Thermal Distortion Results

In this appendix a measured thermally distorted laser beam pattern is compared with results obtained numerically. In Fig. E-1, the distorted CO_2 beam pattern obtained with Kalvar film in a liquid CS_2 experiment simulating a wind is shown on the right-hand side. The value of N as computed using Eq. (1) and the appropriate experimental conditions (Ref. 1, Figs. 36 and 37, P=2 W case) is 20 for the measured pattern. On the left-hand side of Fig. E-1, numerical results obtained by Bradley and Herrmann (Ref. 2) with the Lincoln Laboratories nonlinear propagation code are shown for a case with N = 16, which is roughly comparable to the distortion parameter for the liquid experiment. In each case the beams were focused and a close similarity between the numerical and experimental results can be seen, particularly with regard to the overall shape of the patterns and the presence of the small central lobes. In particular, both the values of I_R and $\Delta x/a_f$, which are, respectively, the peak intensity normalized by the undistorted intensity and the normalized beam shift into the wind, are in agreement as shown in Fig. E-1. The calculated constant intensity contours are labeled to indicate the values of intensity normalized by the peak. The constant intensity contour represented by the edge of the measured pattern corresponds to 14 percent of the peak which is indicated by the x. This was determined by comparing the measured intensity profile (Ref. 1, Fig. 37, P = 2 W case) with the Kalvar image of the beam pattern. The dashed circles represent the undistorted 1/e intensity contours of the focused spots for each case.

The thermal distortion results are shown in Fig. E-1 in terms of normalized dimensions and intensity levels; and the physical parameters for each case are also given in normalized fashion in terms of the distortion parameter N, the fractional absorption, αz, and the ratio of initial to focused spot sizes, a_i/a_f of the beams in the absence of distortion. Of these parameters, the values for αz differ the most between the numerical and experimental cases. In view of the results showing the αz dependence of the distortion in Sec. 2.4, the larger αz in the liquid experiment may be responsible for the good agreement between the numerical and experimental results in spite of the fact that the values of N differ between the numerical (N = 16) and experimental (N = 20) cases.

Perhaps the most important point to be made by the comparison in Fig. E-1 of the numerical results with those obtained experimentally concerns the vastly different conditions between (a) the laboratory simulation of wind with a small ($\sim$ 5 in. long) cell of liquid CS_2 moving across the beam, and (b) the numerical calculations which were performed using conditions typical for high-power propagation in the atmosphere. The actual conditions associated with the liquid CS_2 experiment and also for which the numerical result in Fig. E-1 was obtained are given in Table E-I. Thus, from the rather good agreement indicated by the results in Fig. E-1, there should be no question about the validity of the liquid simulation of atmospheric propagation in a wind. In addition, Fig. E-1 provides convincing evidence for the usefulness of the parameter, N, for the scaling or comparison of the convective thermal lens effects under widely differing conditions, e.g., as in Table E-I.

TABLE E-I

COMPARISON OF CONDITIONS FOR FIG. E-1

$\lambda = 10.6\ \mu$

	Numerical Results (Lincoln Labs.)	Liquid CS_2* Experiments
Power, P	100 kW	2 W
Source radius, a_i	10 cm	1 mm
Focused radius, a_f	3.6 cm	0.22 mm
Range, z	2 km	15.5 cm
Wind Velocity, V	2 m/s	1 cm/s
N	16	20
αz	0.134	2.2
$kn_o a_i^2/z$	3	5.7
a_i/a_f	2.8	4.5

* Liquid CS_2 results have been taken from Ref. 1, Figs. 36 and 37. To avoid confusion the distinctions between the cell length, t and z, and the effective propagation constant, k_e and kn_o, are omitted here.

FIG. E-1

FOCUSED BEAM THERMAL DISTORTION

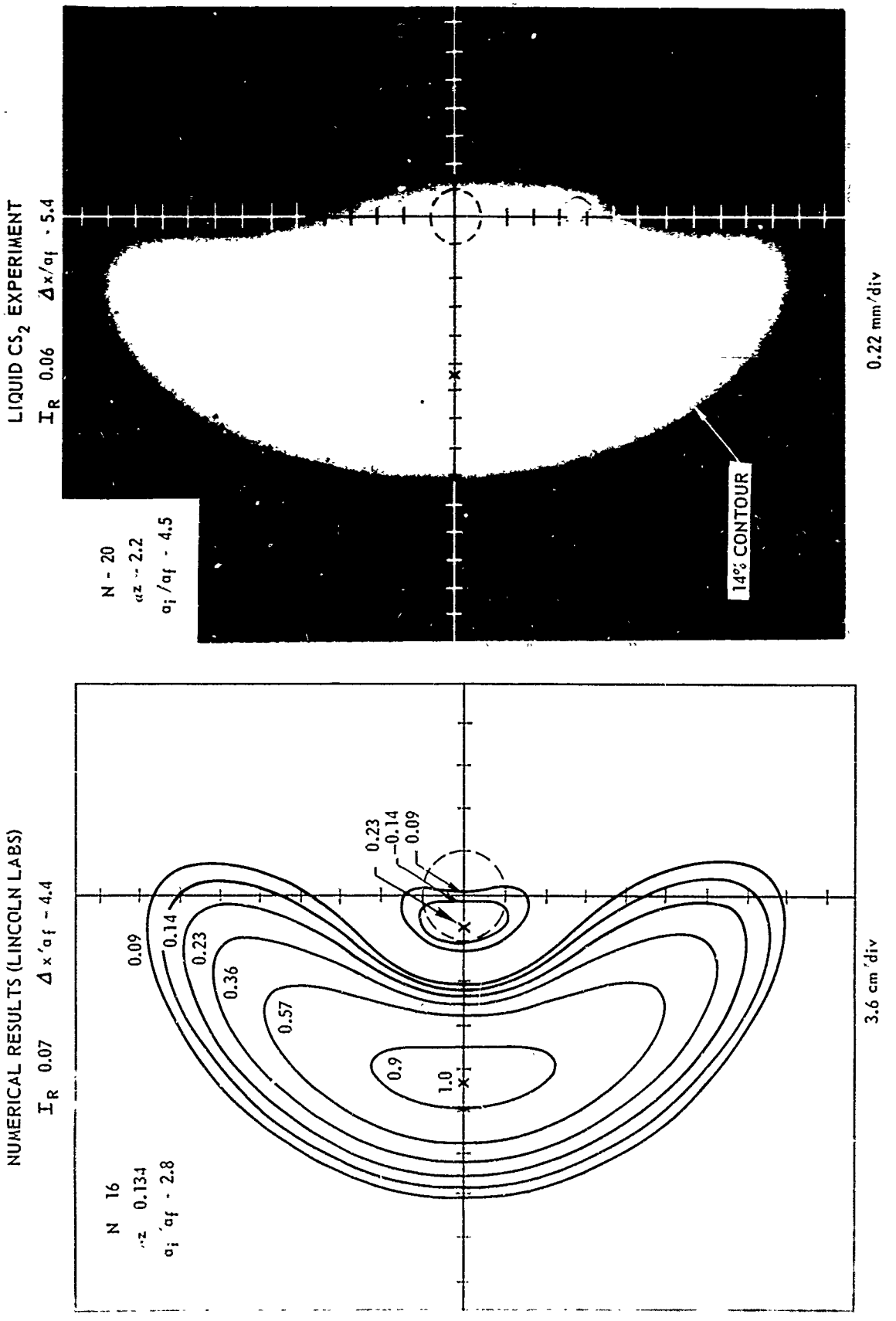

Acknowledgments

The authors are pleased to acknowledge helpful technical discussions and the continued encouragement and support of Dr. Rudolph G. Buser and Dr. Robert S. Rohde of the Electronics Technology and Device Laboratory, U. S. Army Electronics Command, Fort Monmouth, New Jersey. We also wish to express our appreciation to Dr. L. Bradley and Dr. J. Herrmann of MIT Lincoln Laboratories for supplying the numerical results in Fig. E-1.